Single-Cell, Real-Time Detection of Antimicrobial Peptide's Attack in Live *E. coli* Cells

By

Zhilin Yang

A dissertation submitted in partial fulfillment of

the requirements of the degree of

Doctor of Philosophy

(Chemistry)

At the

University of Wisconsin-Madison

2018

Date of Final oral Examination: 6/12/2018

The dissertation is approved by the following members of the Final Oral Committee:

James C. Weisshaar, Professor, Chemistry

Lloyd M Smith, Professor, Chemistry

Samuel H. Gellman, Professor, Chemistry

Alessandro Senes, Associate Professor, Biochemistry

TABLE OF CONTENTS

Acknowledgement

It has been 22 years in school starting from kindergarten. Finally, I am leaving school. I cannot believe that this long journey is going to end soon. Were I not here today, I could not have imagined that I were able to pave all the way here, almost getting a doctoral degree from University of Wisconsin at Madison. In this final assignment at school, I would like to thank everyone who contribute to my PhD degree.

First and foremost, I want to thank my parents. Due to personal health or family financial issues, unfortunately neither of them could make it to university though they were all top students in their classes. So, they tried their best to avoid similar tragedies on me. They spared no efforts to educate, love, care, support and encourage me. They also set good examples in life to me what kind of traits that I should have. I cannot appreciate more for what they have contributed, sacrificed and endured.

I also want to thank all the other family members and relatives who helped me. I especially want to thank my aunt Eva Yang and her husband John Pan. Aunt Eva has always been treating me as her child since I was born. She supported me both mentally and financially. As the first person in my family who studied and worked abroad, she influenced me in many ways. I also want to thank uncle John who helped me a lot with my GRE writing.

Next, I would like to thank all the teachers that I have encountered. I feel very grateful and lucky to have so many amazing and responsible teachers. I especially want to thank my English teachers, chemistry teachers and physics teachers in the middle school and high school. They helped me to shape my interests in these three subjects, which are most related to what I

am doing now. I also want to say big thank you to all my headteachers who helped me a lot not only in study but also in life. I want to thank my undergraduate course advisor Professor Fengpei Du for giving me a lot of help and advices. I want to thank Professor Xuefeng Li for the help and support. I want to thank Professor Zhengying Pan from Peking University Shenzhen Graduate School for giving me an opportunity to have my first real research experience in his lab. I also want to thank my undergraduate research advisor Professor Hongchao Guo for his training, which lead to my first first-author paper in his lab.

Before graduate school, my family was in somewhat tough situation. Therefore, I really want to thank to all those scholarship, fellowship and personal support that helped me to go through university. I also want to thank my classmates and good friends who accompanied me all the way.

Graduate school is a new chapter and graduate school in Wisconsin is cold. Fortunately, I met many warm-hearted people here and they helped me to enjoy those five years.

I would like to thank former and current Weisshaar group members. I thank Dr. Heejun Choi, Dr. Ken Barns and Dr. Nambirajan Rangarajan for their help with initiating my projects in Weisshaar lab. I particularly want to thank Dr. Choi, who was my mentor, collaborator and good friend. He helped me a lot both in science and life. I also want to thank my peer members Sonisilpa Mohapatra and Nikolai Radzinski for their help and accompanying. I want to thank my juniors Mainak Mustafi, Anurag Agrawal and Yanyu Zhu for some fun conversations both inside and outside science. I also what to thank two undergraduates that I have dealt with, Meghan Turner and Sam Rider for bringing different experiences to me. In addition, I would like to thank past group member Dr. Somenath Bakshi and Dr. Wenting Li for all kinds of help and tips.

Outside the lab, I would like to thank all the staff members in the chemistry department for all kinds of help and support. For example, I want to thank Sue Martin Zernicke and Kristi Hemmings for coordination and free food, Chad Skemp for purchasing, Arrietta Clauss for career information sessions, Kendall Schneider for machine shop help, Rob McClain for electronics help, Comhelp for computer stuffs, Tracy Drier for glassblowing instructions, and GSFLC for organizing various activities. I want to thank Professor Lingjun Li, who was the first professor that I interacted with since landing in Madison, for leaving me a very good impression of the chemistry department. I also want to thank other badgers for the help with research. For example, I want to thank Thiago Santos and John Crooks from Weibel lab for help with getting KEIO collection strains and microfluidics fabrication. I want to thank Patricia Sanchez from Gourse lab for providing P1 phage. I want to thank Lesie Rank from Gellman lab for help with peptide synthesis.

Graduate school is packed with research and long. However, life needs a balance. Therefore, I want to thank people who made my graduate school relaxing and enjoyable. I want to thank my otto Dr. Yusuke Okuno and his parents for the care and support. Yusuke accompanied me through the last three years of my PhD. I really want to thank him for his great patience and kindness. My life has more flavors because of his appearance. In addition, I really want to thank all my badminton friends. Without them, I would not be able to enjoy exercises continuously in the last five years. I also want to thank all other friends I made in Madison, especially Zhengwei Chen, Yajin Chen, Chunhua Yao, and Yaoxin Liang. They are all very nice people and we shared a lot of good memories. I also want to thank Dr. Runhui Liu and Dr. Chenxuan Wang for sharing their scientific experiences. I want to thank Le Zhang from University of Missouri for keeping encouraging me since applying for graduate school.

Besides exercises, music my other way to relax. For that, I want to thank composer Yanni. His music always makes me feel peaceful and focus quickly. I also want to thank the beautiful views in Madison. Biking in the summer morning from home to the department enlightens my day.

PhD is long and easy to get lost. Therefore, I feel honored to have Professor Lloyd Smith and Professor Samuel Gellman serving in my committee for the last four years. They are all great scientists and provided me many suggestions in terms of science. They also supported me very well when I was applying for HHMI international student fellowship and postdoc. Moreover, I am very happy to have Professor Alessandro Senes joining my thesis committee. I am looking forward to the tips he is going to give to me.

Last but not least, I want to say thank you so much to my advisor Professor James Weisshaar. Jim has always been very supportive. He is always there whenever I need advice and help. He gives feedbacks very promptly. He gives encouragement so that I was able to try and learn new things. In addition, he is very considerate to students. Under his training, I really enjoyed my graduate school. I wish all the best to his remaining time at office and new life after retirement.

Rome was not built in a day, but they were laying bricks every hour. The page is too short, so the acknowledgment is to be continued……

Abstract

Antimicrobial peptides (AMPs) are important bacterial population regulators used by nearly all living organisms. Understanding bacteria-AMPs interaction will help to understand bacterial imbalance causing human chronic inflammatory diseases. In addition, unlike small molecule antibiotics, AMPs are multifunctional and less susceptible to development of bacterial resistance, serving as a platform to design a new class of peptide-based antibiotics. To obtain the complete picture of AMP action, my thesis work utilized single-cell, time-lapse quantitative fluorescence microscopy with various fluorescent indicators and the *E. coli* model system to directly observe bacterial cellular responses upon AMP attack. The technique reveals cell response heterogeneity and enables correlation of different phenomena in space and time, rendering clues of interactions between different AMP mechanisms. I identified and dissected complex membrane events during the attack of Melittin on *E. coli.* I have developed a new single-cell, time-lapse fluorescence microscopy assay that reports on the permeabilization of the *E. coli* outer membrane to small molecules, with the use of HaloTag technique. In addition, my co-worker and I found that some antimicrobial peptides inhibit *E. coli* growth more efficiently in aerobic than in anaerobic conditions, likely due to oxidative stress. In the detailed study of human antimicrobial peptide LL-37, we found that LL-37 induces reactive oxygen species formation after entry into the periplasm, but before permeabilization of the cytoplasmic membrane. We also found that LL-37 targets specifically cytochrome oxidase *bd* of the electron transport chain, resulting in elevated level of reactive oxygen species.

ABBREVIATIONS

E. coli: *Escherichia coli*

OM: Outer Membrane

CM: Cytoplasmic Membrane

LPS: lipopolysaccharide

OmpF: Outer membrane porin F

NADH: quinone reductases, or NuoA-N

ROS: Reactive Oxygen Species

SOD: Superoxide Dismutase

AMP: Antimicrobial Peptide

GFP: Green Fluorescent Protein

Chapter 1

Introduction

This introductory chapter comprises two parts. Part I describes the general structure of *Escherichia coli (E. coli)* cell envelope and brief description of oxidative stress in *E. coli*. *E. coli* is the model organism used throughout my thesis work. The introduction of oxidative stress would assist the reading of chapter 4. Part II introduces antimicrobial peptides (AMPs) in terms of discovery, significance and mechanisms, techniques developed in our lab and a brief summary of my thesis work.

PART I: CELL ENVELOP OF *E. COLI* and OXIDATIVE STRESS IN *E. COLI*

Cell envelop of *E. coli*

E. coli is a well and widely studied Gram-negative bacteria, with a complete collection of single-gene deletion mutants available. Meanwhile, *E. coli* is one of the leading Gram-negative bacteria that cause many diseases, such as recurrent urinary tract infections, neonatal meningitis, and colon cancer[1].

In order to increase its survival rate, *E. coli* has developed a multilayered envelop, which is composed of outer membrane (OM), periplasm and cytoplasmic membrane (CM) (**Figure 1.1**)[2]. OM and CM are lipid bilayers both containing transmembrane proteins and lipoproteins, but with different structures[3]. OM has phospholipids confined to its inner surface and lipopolysaccharide (LPS) attached to its outer surface. OM acts as a barrier against foreign molecules from outside with LPS layer reinforcing the barrier function. Anionic phospholipids and LPS yields net negative charge on OM. Most of the transmembrane proteins on OM are channels enabling passive diffusion of small molecules (~600 Da). However, recently outer membrane porin F (OmpF) was suggested to allow the passage of large molecules such as colicins (~3.5 kDa)[4].

The periplasmic space between OM and CM is thin, occupying only ~10% of the cell volume[5]. It houses the peptidoglycan layer, which is important for the cell growth and cell shape[6-8], and some important proteins especially enzymes for the formation of disulphide bonds[9].

Further inward lies the CM. The CM phospholipid bilayer consists of phosphatidylethanolamine (neutral, 70-80%), phosphatidylglycerol (-1 charge, 15-20%), and a small amount of cardiolipin (-2 charge, <5%)[10]. The CM is responsible for respiration and membrane potential generation.

Oxidative stress in *E. coli*

E. coli grows under both aerobic condition and anaerobic condition, mainly due to its flexible electron transport chain in the CM. The electron transport chain is composed of dehydrogenases, a quinone pool, and reductases (**Figure 1.1**)[11]. Dehydrogenases transfer electrons from specific donors to a quinone pool. Then electrons from reduced quinones are transferred to different electron acceptors through terminal reductases. At the aerobic condition, *E. coli* runs active electron transport chain using NADH as the major electron donor, NADH dehydrogenase (NDH) complexes as the major dehydrogenases, ubiquinone as the major quinone, and two primary oxidoreductases, cytochrome *bo*$_3$ and cytochrome oxidase *bd*, with O_2 as the major terminal electron acceptor[12]. When O_2 concentration is high, cytochrome *bo*$_3$ predominates. At low O_2 concentration, cytochrome *bd* expression increases. Both cytochrome *bo*$_3$ and cytochrome *bd* contribute to proton motive force generation, but the H^+/e^- ratio is 2 for cytochrome *bo*$_3$ and 1 for cytochrome *bd*[13].

In reality, O_2 is not completely reduced by the aerobic electron transport chain. Some partially reduced O_2 species might leak out from the electron transport chain or form after accidental interaction with the exposed redox moieties of electron-transfer enzymes especially

the abundant flavoenzymes[14-16]. These partially reduced O_2 species are called reactive oxygen species (ROS) which include superoxide (O_2^-), hydrogen peroxide (H_2O_2) and hydroxyl radical (•OH) (**Figure 1.1**). The charged O_2^- is not permeable to the membrane at neutral pH, but uncharged H_2O_2 penetrates membranes[17]. Therefore, ROS level within the cytoploasm increases whenever exogenous H_2O_2 is present. ROS, especially •OH, cause strong oxidative stress to *E. coli* cells. They can damage many intracellular components, including heme-containing proteins and DNA[15].

To combat oxidative stress, *E. coli* produces a variety of scavengers such as superoxidases (SOD), peroxidases and catalases. *E. coli* contains three SODs, two in the cytoplasm (Mn-SOD and Fe-SOD) and one in the periplasm (CuZn-SOD)[17-18]. In general, the cytoplasmic SODs are abundant enough to convert O_2^- to H_2O_2 and keep steady state O_2^- at subnanomolar concentration. H_2O_2 is primarily scavenged by peroxidases. When H_2O_2 doses saturates peroxidases, the expression of catalases will be strongly induced and catalases will take over the H_2O_2 scavenging job. However, if ROS accumulated inside cells saturate all ROS scavengers, cells will suffer growth defect and possible death. Recent studies show that some bactericidal antibiotics impose oxidative stress in *E. coli*, likely contributing to their killing activity[19-20].

PART II: Antimicrobial peptides

The discovery of antimicrobial peptides

Antimicrobial peptides are relatively short peptides (~12-50 aa) that exist in nearly all organisms, protecting the hosts from invading pathogens. They are typically cationic and amphipathic, but vary in conformation, structure, hydrophobicity, and amphipathicity[21-22]. AMPs

display a broad spectrum of activities against a range of bacteria, fungi, viruses, parasites and cancer cells[23-25].

The discovery of AMPs dates back to the late 19th century when researchers observed bacterial cell death after phagocytosis[26] and bread yeast death by some lethal substance in the wheat flour[27]. Researchers suspected that some natural antimicrobial compounds might exist. In 1939, soil microbiologist René Dubos extracted the first AMP from a soil *Bacillus* strain[28]. This AMP showed strong antibacterial activity, even protecting mice from *Pneumococcus* infection[29]. In the following year, René Dubos collaborated with biochemist Rollin Hotchkiss and they characterized and identified the antimicrobial extract to be gramicidin[30]. Later, gramicidin became the first clinically tested and commercially manufactured antibiotic agent[31]. It was used as a topical antibiotic to treat wounds and ulcers during World War II. Following gramicidin, more and more AMPs were discovered and characterized from nature, such as purothionin from plant[32], defensins from rabbit[33] and human[34], bombinin[35] and magainins[36] from frog, and cecropins from moth[37]. As of January 2018, more than 2950 natural AMPs have been reported[38].

AMPs: promising platform for novel antibiotics

Before the introduction of antibiotics, patients could barely survive from bacterial infections. The promotion of penicillin and streptomycin in 1943 saved millions of lives and brought the ‘Golden Age of antibiotics’. Unfortunately, the ‘Golden Age of antibiotics’ was just a flash in the pan, resulting in an upgraded war between human and bacteria.

At the very beginning, it was not expected that the development and application of antibiotics would be coupled with bacterial antibiotic resistance evolution. Bacteria develop resistance quickly, as traditional antibiotics only target specific cellular activities, and thus many traditional antibiotics have short shelf time. During the ‘Golden Age of antibiotics’, the

investigation of natural antimicrobial compounds slowed down, and research focused on the modification of existing compounds. This enabled some bacteria to outpace the development of new antibiotics. In the early 1960s, multidrug-resistant bacteria emerged. Worse still, no new antibiotics have been approved since 1960s, except daptomycin which was discovered in 1968 but not approved until 2003[39]. The abuse of antibiotics in clinics and livestock aggravated the situation. Now the challenges from bacteria are more and more severe and it is more and more pressing to search for novel alternative antibiotics.

Under this circumstance, the ancient soldier AMP attracts attention again and is considered a promising candidate for future antibiotics. AMPs are much less likely to induce resistance in bacteria, in part due to their broad spectrum of activities and multiple modes of action. They can be used as either a single antimicrobial agent or combination with traditional antibiotics, delaying antibiotic resistance formation and fighting against multi-drug resistant bacteria[40-41]. Some AMP-based antibiotics are already in the clinical trial phase II or III[42-43], such as Omiganan (Microbiologix Biotech) for bacteria and fungi/bloodstream infections, Surotomycin (Merck) for *Clostridium difficile*-associated diarrhea, and Brilacidin (PolyMedix) for *Staphylococcus aureus* skin infections. Still, some bottlenecks halted the development of AMPs from the bench to the clinic[44], and one of them is the lack of structure-function relationship.

AMPs: modulators for the immune system

For a long time, AMPs were thought to fight against bacteria directly. Gradually, studies show that many AMPs also act as immune signaling molecules[45]. For some AMPs, immunomodulation is their primary role inside the hosts[46]. Therefore, AMPs are also called host defense peptides.

Tight regulation of immunological responses by AMPs is vital for the proper maintenance of commensal microorganisms in the hosts' complex environment of all living organisms[46-47]. Dysregulation of commensal flora was found to associate with many human chronic inflammatory diseases, such as asthma, cancer, and stroke[48-50]. Understanding the circumstances of such balanced and sometimes imbalanced interactions between bacteria and host AMPs is necessary to explore the causes and therapeutic implications for human chronic inflammatory diseases.

Direct antimicrobial mechanisms of AMPs

Originally, AMPs were characterized as pore formers, causing loss of membrane integrity. However, recent studies have shown that AMPs also cause damages to intracellular targets.

Membrane permeabilization by AMPs has been extensively studied with synthetic lipid bilayers, by exploiting techniques such as X-ray crystallography, Nuclear Magnetic Resonance spectroscopy, Fourier transform infrared, and fluorescence optical spectroscopy[21, 51]. The attraction, attachment, insertion and orientation of AMPs, as well as the orientation of the lipids and the thickness and integrity of the lipid bilayer were measured. Numerous models were proposed to explain the lipid bilayer disruption by AMPs. There are four models that are most popular: 1) barrel-stave model in which peptides insert perpendicular to the membrane and form barrel-like pores; 2) toroidal model in which peptides insert perpendicular to the membrane but twist local membrane curvature resulting in toroidal pores; 3) carpet model in which peptides act as detergents and dissolve the membranes into micelle-like structures; and 4) aggregate model in which peptides aggregate on the membrane surface and interact with the hydrophobic fatty acid 'tails' forming disorganized and transient pores (**Figure 1.2**). Although the artificial membrane

studies provide insights to the membrane permeabilization activity of AMPs at the molecular level, they may not accurately reflect what happens to the real biological membrane. Currently there are still some gaps between these two systems[52].

In the recent years, researchers have been trying to better understand the direct antimicrobial mechanisms of AMPs on cells and found that AMPs do more than membrane permeabilization. The speculation initially came from the observation that *E. coli* growth reduces significantly while membrane remains intact under the attack of Bac7 fragments[53]. The finding that buforin II enters the cytoplasm without permeabilizing the cytoplasmic membrane drove the exploration of possible intracellular targets[54-55]. Indeed, AMPs can affect many essential biological processes[56]. For example, buforin II and tachyplesin can bind to DNA. Pleurocidin and indolicidin can inhibit the synthesis of DNA, RNA and protein. Histains and apidaecin can inhibit enzymatic activity. Gramicidin can inhibit cytochrome oxidase *bd* complex[57]. Some AMPs target both membrane and intracellular activities, and some AMPs target multiple intracellular activities. It is evident that AMPs display complex mechanisms in their attack on microbes. Furthermore, AMPs activities may be modulated by the environment, based on the result that the bacterial killing ability of some AMPs is stronger at lower salt concentration[56] or in a reducing environment[58].

Despite these observations, there is still no clear understanding of the mechanisms by which AMPs attenuate growth and ultimately kill cells. Obtaining a complete picture of existing and underlying AMPs mechanisms and their roles in the lethality of AMPs is essential to identify novel antibacterial targets, to assist the rational design of effective peptide-based antibiotics, and to better understand human chronic inflammatory diseases caused by bacteria imbalance.

Single-cell, time-lapse fluorescence microscope study of AMPs

Live-cell imaging techniques are powerful tools to uncover the dynamic, multifaceted actions of AMPs on the bacterial cells[59]. They are exempted from sample fixation and processing, which are typically required for techniques such as immunolocalization[60], electron microscopy[61], and atomic force microscopy[62]. However, historically most live-cell studies of AMP mechanisms have been restricted to either imaging individual cells at a specific time point, or imaging the entire cell population at different time points after AMP treatment. The former fails to track the dynamic responses of cells to AMPs, and the latter only reflects the average AMP effect on the entire population. Neither shows the heterogeneity of cell responses owing to AMPs multifaceted mechanisms. To circumvent this issue, our lab has developed several single-cell, time-lapse fluorescence microscope assays by utilizing various fluorescent indicators and phase contrast[63-66]. These assays allow the imaging and quantitative measurements on the same cells to monitor their complex and dynamic changes in response to AMPs on the time scale of a few seconds to tens of minutes. In addition, different biochemical events can be observed in the same cells in space and time, enabling the dissection and correlation of the complex antimicrobial modes of AMPs in live cells. Our lab has applied these techniques to well-understood Gram-negative bacterium *E. coli* and Gram-positive bacterium *Bacillus subtilis*.

Our first application of the single-cell, time-lapse fluorescence microscopy technique was reported in 2010, on the actions of human AMP LL-37 in single live *E. coli* cells[66]. Prior to that work, the understanding of antimicrobial mechanism of LL-37 was restrained to model membrane studies and bulk assays. LL-37 was only known to disrupt membranes. By using rhodamine labeled LL-37, our lab found that there LL-37 attacks *E. coli* cells in three distinct phases. First LL-37 binds to the outer surface of OM. Then in the phase 2, LL-37 gains access to the periplasm at the curved region of OM, either at the septum region for septating cells or

endcap for nonseptating cells, inducing cell shrinkage and OM permeabilization to Green Fluorescent Protein (GFP, 26 kDa) size molecules. Interestingly, cell length decreases gradually while LL-37 slowly spreads across the entire cell. The phase 2 lasts about 5-10 min. Finally, CM also becomes permeabilized. In 2015, we reported new assays to detect reactive oxygen species (ROS) formation in the single *E. coli* cells at real time[67]. In that work, we studied the activities of synthetic AMP CM15. We found that CM15 enhances ROS level inside *E. coli* cells dramatically in the aerobic condition, likely to explain why CM15 activity is stronger in the aerobic condition than in the anaerobic condition.

My thesis work applied the existing assays and designed new assays to reveal the actions of AMPs more clearly in live *E. coli* cells. In Chapter 2, I observed and dissected a series of events induced in *E. coli* membranes by Melittin. Strikingly, six separate events happened within ~20 s. Moreover, for the first time we observed membrane resealing behavior soon after membrane permeabilization under the attack of AMPs. In Chapter 3, by applying HaloTag technique, I developed a new single-cell, time-lapse fluorescence microscopy assay that reports on the permeabilization of the *E. coli* OM to small molecules, with time resolution of 3 s or better. The new assay suggests a common mechanism of *E. coli* membrane permeabilization induced by cationic peptides. We hypothesize that cationic peptides may all cause OM permeabilization to small molecules first and possibly including themselves. After a time lag, the OM is transiently and abruptly permeabilized to large molecules such as GFP, followed by abrupt CM permeabilization. In Chapter 4, we found that similar to CM15, some AMPs also inhibit *E. coli* growth more efficiently in aerobic than in anaerobic conditions, likely due to oxidative stress. In a detailed study of LL-37, we found that LL-37 induces ROS after entry into the periplasm, but before permeabilization of the cytoplasmic membrane. We also found that LL-

37 targets specifically cytochrome oxidase *bd* on the electron transport chain, resulting in elevated ROS level. Chapter 5 describes possible future extensions of this work. Chapter 6 is an extended chapter for communicating Ph.D. research to the public, with the support from Wisconsin Initiative for Science Literacy (WISL).

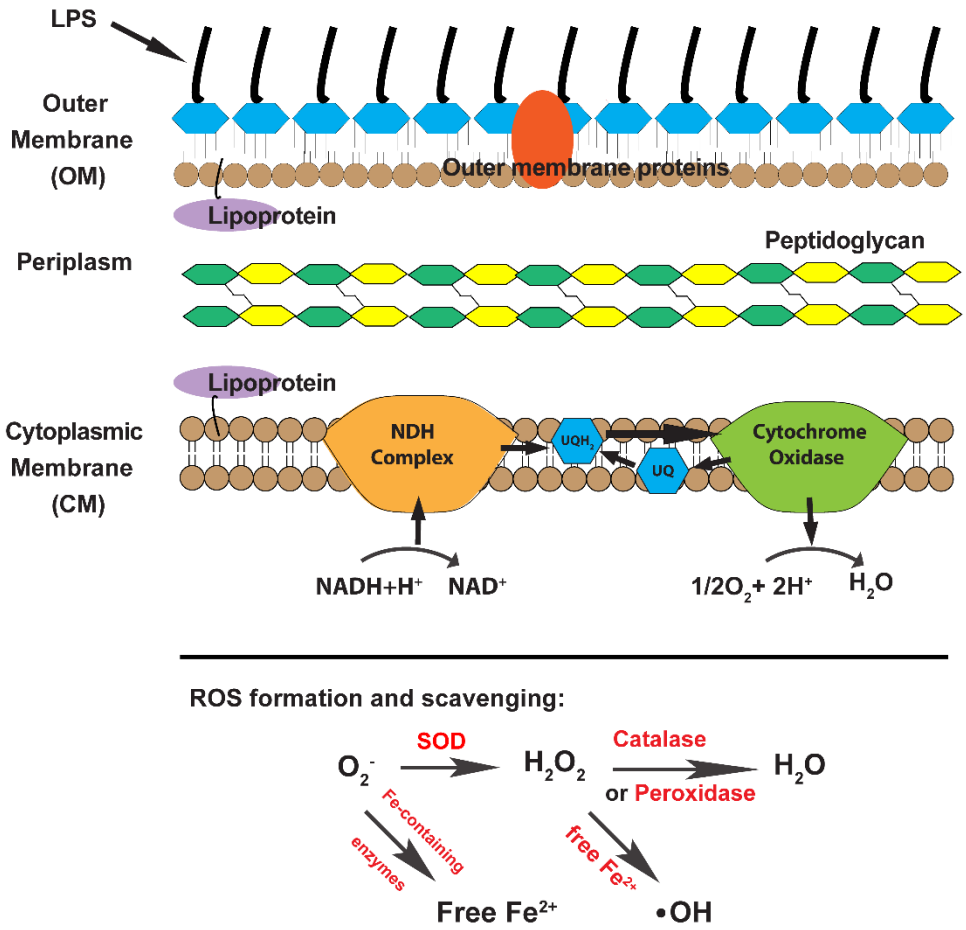

Figure 1.1 The scheme of *E. coli* envelope, and ROS formation and scavenging. The OM is a lipid bilayer with phospholipids in its inner leaflet, lipopolysaccharide (LPS) in its outer leaflet, and proteins across or anchored. The periplasm lies between the OM and the CM, housing the peptidoglycan cell wall. The CM is a lipid bilayer composed of phospholipids (PL), also containing integral membrane proteins and lipoproteins. The electron transport chain resides in the CM. Several enzymes are expressed to scavenge ROS.

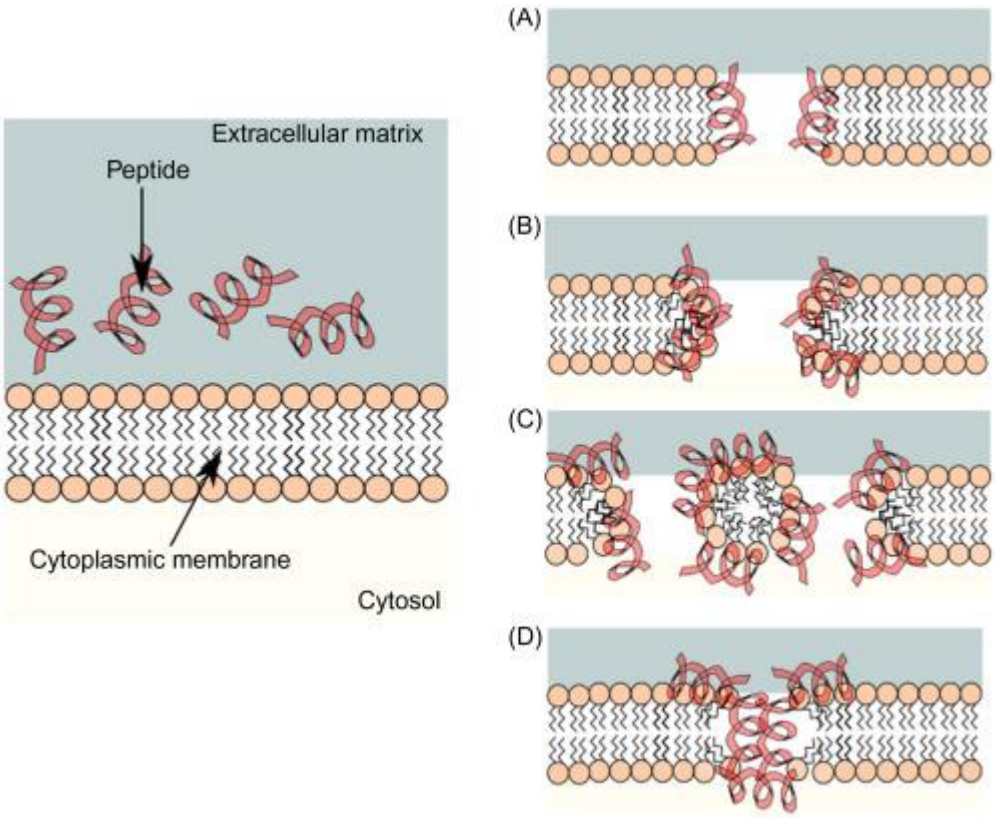

Figure 1.2 Four popular models for the interaction of AMPs and lipids. (A) Barrel-stave model. (B) Toroidal pore model. (C) Carpet model. (D) Aggregate model. This figure is adopted from reference 43 with permissions.

References

1. Raisch, J.; Rolhion, N.; Dubois, A.; Darfeuille-Michaud, A.; Bringer, M. A., Intracellular colon cancer-associated Escherichia coli promote protumoral activities of human macrophages by inducing sustained COX-2 expression. *Lab Invest* **2015,** *95* (3), 296-307.

2. Silhavy, T. J.; Kahne, D.; Walker, S., The bacterial cell envelope. *Cold Spring Harb Perspect Biol* **2010,** *2* (5), a000414.

3. Ruiz, N.; Kahne, D.; Silhavy, T. J., Advances in understanding bacterial outer-membrane biogenesis. *Nat Rev Microbiol* **2006,** *4* (1), 57-66.

4. Zakharov, S. D.; Sharma, O.; Zhalnina, M.; Yamashita, E.; Cramer, W. A., Pathways of colicin import: utilization of BtuB, OmpF porin and the TolC drug-export protein. *Biochemical Society transactions* **2012,** *40* (6), 1463-8.

5. Van Wielink, J. E.; Duine, J. A., How big is the periplasmic space? *Trends in Biochemical Sciences* **1990,** *15* (4), 136-137.

6. Uehara, T.; Park, J. T., Growth of *Escherichia coli*: significance of peptidoglycan degradation during elongation and septation. *J Bacteriol* **2008,** *190* (11), 3914-22.

7. Reshes, G.; Vanounou, S.; Fishov, I.; Feingold, M., Cell shape dynamics in *Escherichia coli*. *Biophys J* **2008,** *94* (1), 251-64.

8. Huang, K. C.; Mukhopadhyay, R.; Wen, B.; Gitai, Z.; Wingreen, N. S., Cell shape and cell-wall organization in Gram-negative bacteria. *Proc Natl Acad Sci U S A* **2008,** *105* (49), 19282-7.

9. Berkmen, M., Production of disulfide-bonded proteins in *Escherichia coli*. *Protein Expr Purif* **2012,** *82* (1), 240-51.

10. Oliver, P. M.; Crooks, J. A.; Leidl, M.; Yoon, E. J.; Saghatelian, A.; Weibel, D. B., Localization of Anionic Phospholipids in *Escherichia coli* Cells. *Journal of Bacteriology* **2014,** *196* (19), 3386-3398.

11. Friedrich, T.; Pohl, T., NADH as Donor. *EcoSal Plus* **2007,** *2* (2).

12. Borisov, V. B.; Verkhovsky, M. I., Oxygen as Acceptor. *EcoSal Plus* **2009,** *3* (2).

13. Unden, G.; Steinmetz, P. A.; Degreif-Dunnwald, P., The aerobic and anaerobic respiratory chain of *Escherichia coli* and *Salmonella enterica*: enzymes and energetics. *EcoSal Plus* **2014,** *6* (1).

14. Imlay, J. A., Pathways of oxidative damage. *Annu Rev Microbiol* **2003,** *57*, 395-418.

15. Imlay, J. A., The molecular mechanisms and physiological consequences of oxidative stress: lessons from a model bacterium. *Nat Rev Microbiol* **2013,** *11* (7), 443-54.

16. Imlay, J. A., Oxidative Stress. *EcoSal Plus* **2009,** *3* (2).

17. Mishra, S.; Imlay, J., Why do bacteria use so many enzymes to scavenge hydrogen peroxide? *Arch Biochem Biophys* **2012,** *525* (2), 145-60.

18. Imlay, J. A., Cellular defenses against superoxide and hydrogen peroxide. *Annu Rev Biochem* **2008,** *77*, 755-76.

19. Kohanski, M. A.; Dwyer, D. J.; Hayete, B.; Lawrence, C. A.; Collins, J. J., A common mechanism of cellular death induced by bactericidal antibiotics. *Cell* **2007,** *130* (5), 797-810.

20. Dwyer, D. J.; Belenky, P. A.; Yang, J. H.; MacDonald, I. C.; Martell, J. D.; Takahashi, N.; Chan, C. T. Y.; Lobritz, M. A.; Braff, D.; Schwarz, E. G.; Ye, J. D.; Pati, M.; Vercruysse, M.; Ralifo, P. S.; Allison, K. R.; Khalil, A. S.; Ting, A. Y.; Walker, G. C.; Collins, J. J., Antibiotics induce redox-related physiological alterations as part of their lethality. *Proceedings of the National Academy of Sciences* **2014,** *111* (20), E2100-E2109.

21. Brogden, K. A., Antimicrobial peptides: pore formers or metabolic inhibitors in bacteria? *Nat Rev Microbiol* **2005,** *3* (3), 238-50.

22. Zasloff, M., Antimicrobial peptides of multicellular organisms. *Nature* **2002,** *415*, 389.

23. Lakshmaiah Narayana, J.; Chen, J. Y., Antimicrobial peptides: Possible anti-infective agents. *Peptides* **2015,** *72*, 88-94.

24. Bahar, A. A.; Ren, D., Antimicrobial peptides. *Pharmaceuticals (Basel)* **2013,** *6* (12), 1543-75.

25. O'Brien-Simpson, N. M.; Hoffmann, R.; Chia, C. S. B.; Wade, J. D., Editorial: Antimicrobial and Anticancer Peptides. *Front Chem* **2018,** *6*, 13.

26. Greenlee-Wacker, M. C., Clearance of apoptotic neutrophils and resolution of inflammation. *Immunol Rev* **2016,** *273* (1), 357-70.

27. Okada, T.; Yoshizumi, H.; Terashima, Y., A Lethal Toxic Substance for Brewing Yeast in Wheat and Barley. *Agricultural and Biological Chemistry* **1970,** *34* (7), 1084-1094.

28. Dubos, R. J., Studies on a bactercidal agent extracted from a soil *Bacillus*. *The Journal of Experimental Medicine* **1939,** *70* (1), 1-10.

29. Dubos, R. J., Studies on a bactericidal agent extracted from a soil Bacillus: II. Protective effect of the bactericidal agent against experimental *Pneumococcus* infections in mice. *The Journal of Experimental Medicine* **1939,** *70* (1), 11-17.

30. Hotchkiss, R. D. D., R.J., Fractionation of the bactericidal agent from cultures of a soil *Bacillus*. *J. Biol. Chem* **1940,** *132*, 791-792.

31. Van Epps, H. L., René Dubos: unearthing antibiotics. *The Journal of Experimental Medicine* **2006,** *203* (2), 259-259.

32. Hernandez-Lucas, C.; Carbonero, P.; Garcia-Olmedo, F., Identification and purification of a purothionin homolog from *rye (Secale cereale L.). Journal of Agricultural and Food Chemistry* **1978,** *26* (4), 794-796.

33. Hirsch, J. G., Phagocytin: A bactericidal substance from polymorphonuclear leucocytes *The Journal of Experimental Medicine* **1956,** *103* (5), 589.

34. Schneider, J. J.; Unholzer, A.; Schaller, M.; Schafer-Korting, M.; Korting, H. C., Human defensins. *J Mol Med (Berl)* **2005,** *83* (8), 587-95.

35. Kiss, G. M., H. , Uber das giftsekret der gelbbauchunke, *Bombina variegata* L. *Toxicon* **1962,** (1), 33-34.

36. Zasloff, M., Magainins, a class of antimicrobial peptides from Xenopus skin: isolation, characterization of two active forms, and partial cDNA sequence of a precursor. *Proceedings of the National Academy of Sciences* **1987,** *84* (15), 5449.

37. Steiner, H.; Hultmark, D.; Engström, Å.; Bennich, H.; Boman, H. G., Sequence and specificity of two antibacterial proteins involved in insect immunity. *Nature* **1981,** *292*, 246.

38. UNMC, The Antimicrobial Peptide Database. **2018**.

39. Lewis, K., Platforms for antibiotic discovery. *Nat Rev Drug Discov* **2013,** *12* (5), 371-87.

40. Lazar, V.; Martins, A.; Spohn, R.; Daruka, L.; Grezal, G.; Fekete, G.; Szamel, M.; Jangir, P. K.; Kintses, B.; Csorgo, B.; Nyerges, A.; Gyorkei, A.; Kincses, A.; Der, A.; Walter, F. R.; Deli, M. A.; Urban, E.; Hegedus, Z.; Olajos, G.; Mehi, O.; Balint, B.; Nagy, I.; Martinek, T. A.; Papp, B.; Pal, C., Antibiotic-resistant bacteria show widespread collateral sensitivity to antimicrobial peptides. *Nat Microbiol* **2018,** *3* (6), 718-731.

41. Xu, X.; Xu, L.; Yuan, G.; Wang, Y.; Qu, Y.; Zhou, M., Synergistic combination of two antimicrobial agents closing each other's mutant selection windows to prevent antimicrobial resistance. *Sci Rep* **2018,** *8* (1), 7237.

42. Kang, H. K.; Kim, C.; Seo, C. H.; Park, Y., The therapeutic applications of antimicrobial peptides (AMPs): a patent review. *J Microbiol* **2017,** *55* (1), 1-12.

43. Sun, E.; Belanger, C. R.; Haney, E. F.; Hancock, R. E. W., Host defense (antimicrobial) peptides. **2018**, 253-285.

44. Wimley, W. C.; Hristova, K., Antimicrobial peptides: successes, challenges and unanswered questions. *J Membr Biol* **2011,** *239* (1-2), 27-34.

45. Hancock, R. E.; Haney, E. F.; Gill, E. E., The immunology of host defence peptides: beyond antimicrobial activity. *Nat Rev Immunol* **2016,** *16* (5), 321-34.

46. Hilchie, A. L.; Wuerth, K.; Hancock, R. E., Immune modulation by multifaceted cationic host defense (antimicrobial) peptides. *Nat Chem Biol* **2013,** *9* (12), 761-8.

47. Alalwani, S. M.; Sierigk, J.; Herr, C.; Pinkenburg, O.; Gallo, R.; Vogelmeier, C.; Bals, R., The antimicrobial peptide LL-37 modulates the inflammatory and host defense response of human neutrophils. *Eur J Immunol* **2010,** *40* (4), 1118-26.

48. Muniz, L. R.; Knosp, C.; Yeretssian, G., Intestinal antimicrobial peptides during homeostasis, infection, and disease. *Front Immunol* **2012,** *3*, 310.

49. Ostaff, M. J.; Stange, E. F.; Wehkamp, J., Antimicrobial peptides and gut microbiota in homeostasis and pathology. *EMBO Mol Med* **2013,** *5* (10), 1465-83.

50. Guani-Guerra, E.; Santos-Mendoza, T.; Lugo-Reyes, S. O.; Teran, L. M., Antimicrobial peptides: general overview and clinical implications in human health and disease. *Clin Immunol* **2010,** *135* (1), 1-11.

51. Marquette, A.; Bechinger, B., Biophysical Investigations Elucidating the Mechanisms of Action of Antimicrobial Peptides and Their Synergism. *Biomolecules* **2018,** *8* (2).

52. Savini, F.; Bobone, S.; Roversi, D.; Mangoni, M. L.; Stella, L., From liposomes to cells: Filling the gap between physicochemical and microbiological studies of the activity and selectivity of host-defense peptides. *Peptide Science* **2018**, e24041.

53. Gennaro, R.; Zanetti, M., Structural features and biological activities of the cathelicidin-derived antimicrobial peptides. *Biopolymers* **2000,** *55* (1), 31-49.

54. Park, C. B.; Kim, H. S.; Kim, S. C., Mechanism of Action of the Antimicrobial Peptide Buforin II: Buforin II Kills Microorganisms by Penetrating the Cell Membrane and Inhibiting Cellular Functions. *Biochemical and Biophysical Research Communications* **1998,** *244* (1), 253-257.

55. Park, C. B.; Yi, K. S.; Matsuzaki, K.; Kim, M. S.; Kim, S. C., Structure-activity analysis of buforin II, a histone H2A-derived antimicrobial peptide: the proline hinge is responsible for the cell-penetrating ability of buforin II. *Proc Natl Acad Sci U S A* **2000,** *97* (15), 8245-50.

56. Nizet, V., Antimicrobial peptide resistance mechanisms of human bacterial pathogens. *Current issues in molecular biology* **2006,** *8* (1), 11.

57. Mogi, T.; Ui, H.; Shiomi, K.; Omura, S.; Kita, K., Gramicidin S identified as a potent inhibitor for cytochrome bd-type quinol oxidase. *FEBS Lett* **2008,** *582* (15), 2299-302.

58. Schroeder, B. O.; Wu, Z.; Nuding, S.; Groscurth, S.; Marcinowski, M.; Beisner, J.; Buchner, J.; Schaller, M.; Stange, E. F.; Wehkamp, J., Reduction of disulphide bonds unmasks potent antimicrobial activity of human beta-defensin 1. *Nature* **2011,** *469* (7330), 419-23.

59. Munoz, A.; Read, N. D., Live-cell imaging and analysis shed light on the complexity and dynamics of antimicrobial Peptide action. *Front Immunol* **2012,** *3*, 248.

60. Theis, T.; Marx, F.; Salvenmoser, W.; Stahl, U.; Meyer, V., New insights into the target site and mode of action of the antifungal protein of Aspergillus giganteus. *Res Microbiol* **2005,** *156* (1), 47-56.

61. Friedrich, C. L.; Moyles, D.; Beveridge, T. J.; Hancock, R. E. W., Antibacterial action of structurally diverse cationic peptides on Gram-Positive bacteria. *Antimicrobial Agents and Chemotherapy* **2000,** *44* (8), 2086-2092.

62. Alves, C. S.; Melo, M. N.; Franquelim, H. G.; Ferre, R.; Planas, M.; Feliu, L.; Bardaji, E.; Kowalczyk, W.; Andreu, D.; Santos, N. C.; Fernandes, M. X.; Castanho, M. A., *Escherichia coli* cell surface perturbation and disruption induced by antimicrobial peptides BP100 and pepR. *J Biol Chem* **2010,** *285* (36), 27536-44.

63. Choi, H.; Rangarajan, N.; Weisshaar, J. C., Lights, Camera, Action! Antimicrobial Peptide Mechanisms Imaged in Space and Time. *Trends Microbiol* **2016,** *24* (2), 111-22.

64. Rangarajan, N.; Bakshi, S.; Weisshaar, J. C., Localized permeabilization of E. coli membranes by the antimicrobial peptide Cecropin A. *Biochemistry* **2013,** *52* (38), 6584-94.

65. Barns, K. J.; Weisshaar, J. C., Real-time attack of LL-37 on single *Bacillus subtilis* cells. *Biochim Biophys Acta* **2013,** *1828* (6), 1511-20.

66. Sochacki, K. A.; Barns, K. J.; Bucki, R.; Weisshaar, J. C., Real-time attack on single *Escherichia coli* cells by the human antimicrobial peptide LL-37. *Proc Natl Acad Sci U S A* **2011,** *108* (16), E77-81.

67. Choi, H.; Yang, Z.; Weisshaar, J. C., Single-cell, real-time detection of oxidative stress induced in *Escherichia coli* by the antimicrobial peptide CM15. *Proc Natl Acad Sci U S A* **2015,** *112* (3), E303-10.

Chapter 2

Melittin-induced Permeabilization, Re-sealing, and Re-permeabilization of *E. coli* Membranes

Adapted from publication listed below:

Yang, Z., Choi, H., and Weisshaar, J. C. (**2018**) Melittin-induced permeabilization, re-sealing, and re-permeabilization of *E. coli* Membranes, *Biophys J 114*, 368-379.

* ZY, HC, and JCW all contributed to design of the project. ZY performed the majority of the experiments. HC performed the experiments of CM15 with *E. coli* cells expressing periplasmic GFP. ZY and JCW analyzed the data and wrote the manuscript. HC helped edit the manuscript. Supplemental movies are available online.

ABSTRACT

The permeabilization of model lipid bilayers by cationic peptides has been studied extensively over decades, with the bee-sting toxin melittin perhaps serving as the canonical example. However, the relevance of these studies to the permeabilization of real bacterial membranes by antimicrobial peptides remains uncertain. Here we employ single-cell fluorescence microscopy in a detailed study of the interactions of melittin with the outer membrane (OM) and the cytoplasmic membrane (CM) of live *E. coli*. Using periplasmic GFP as probe, we find that melittin at twice the minimum inhibitory concentration (MIC) first induces abrupt cell shrinkage and permeabilization of the OM to GFP. Within ~4 s of OM permeabilization, the CM invaginates to form inward facing "periplasmic bubbles". Seconds later the bubbles begin to leak periplasmic GFP into the cytoplasm. Permeabilization is localized, consistent with possible formation of toroidal pores. Within ~20 s, first the OM and then the CM re-seals to GFP. Some 2–20 min later, both CM and OM are re-permeabilized to GFP. We invoke a mechanism based on curvature stress concepts derived from model bilayer studies. The permeabilization and re-sealing events involve sequential, time-dependent build-up of melittin density within the outer and inner leaflets of each bilayer. We also propose a mechanical explanation for the early cell shrinkage event induced by melittin and a variety of other cationic peptides. As peptides gain access to the periplasm, they bind to the anionic peptido-crosslinks of the lipopolysaccharide layer, increasing its longitudinal elastic modulus. The cell wall shrinks because it can withstand the same turgor pressure with smaller overall extension. Shrinkage in turn induces invagination of the CM, preserving its surface area. We conclude by comparing the behavior of different peptides.

INTRODUCTION

Melittin, a toxic component of bee venom, is a 26-residue cationic peptide of +6 charge that can lyse eukaryotic cells and kill bacterial cells [1]. In the crystal structure of melittin, the peptide adopts a bent, amphipathic helical structure. Residues 1–10 and 13–26 form helices whose axes lie 120° apart due to the presence of Pro-14 [2]. Melittin has served as an important model for understanding the mechanisms by which cationic antimicrobial peptides (AMPs) permeabilize lipid vesicles. Previous work includes studies of small, large, and giant unilamellar vesicles (SUVs, LUVs, and GUVs), both zwitterionic and anionic [3-7]. At peptide-to-lipid (P/L) ratios of ~1/100 or lower, melittin induces permeabilization sites (usually interpreted as pores) that pass small ions and organic dye molecules [5-6, 8]. Even after a long observation time, not all of the dye is released [9], consistent with formation of transient pores with lifetimes on the order of 10 ms [3]. At P/L ratios of ~1/50 or higher, melittin evidently induces permanent, equilibrium permeabilization sites in GUVs [7]. Oriented circular dichroism of melittin interacting with hydrated multilayers shows that at these higher concentrations, most melittin molecules change orientation from parallel to perpendicular to the bilayer plane [7]. This is consistent with formation of toroidal pores, although other permeabilization models are possible. Accordingly, neutron diffraction experiments on multilayers at high P/L have detected D_2O-filled pores of 4.4 nm inside diameter [10]. Most recently, stable permeabilization sites have been induced in cytoplasmic membrane spheroplasts derived from *E. coli* [11].

The relevance of studies of AMP interactions with model lipid bilayers to the mechanisms by which the same peptides kill real bacterial cells remains uncertain [12]. In an effort to provide more information, we and others have used single-cell, time-resolved fluorescence microscopy to directly observe membrane permeabilization events in live bacterial cells [13-20]. Here we present a

detailed study of melittin interactions with the membranes of live *E. coli*. Surprisingly, using GFP as the probe species, we observe sequential permeabilization, re-sealing, and re-permeabilization of both the outer membrane (OM) and the cytoplasmic membrane (CM). Seconds after the initiation of OM permeabilization, we detect short-lived, inward facing invaginations in the CM. For septating cells, these "periplasmic bubbles" evidently provide the conduit through which GFP, the dye Sytox Orange, and presumably melittin itself, gain access to the cytoplasm. We suggest that when melittin crosses the OM and enters the periplasm, it binds to anionic crosslinks of the peptidoglycan (PG) layer [21]. This causes the cell wall to stiffen and contract. Cell wall shrinkage in turn forces the CM to shrink in length by invagination. Our proposed mechanism for the permeabilization and re-sealing events invokes the same curvature stress arguments originally used to explain AMP permeabilization and re-sealing of lipid vesicles [5, 7, 22].

METHODS

We have developed a variety of real-time, single-cell imaging protocols that reveal the sequence of events in the attack of AMPs on live *E. coli* at an unusual level of detail. The protocols differ in imaging modality, labeling methods, and camera frame rate. In all experiments reported here, cells are plated in a microfluidics chamber and are growing in a continuous flow of aerated, 30°C EZ rich defined medium (EZRDM). The flow of 10 μM melittin (twice the aerobic MIC) in EZRDM begins at $t = 0$ and continues throughout the duration of the imaging experiment. This maintains a constant peptide concentration in the cell surround.

Bacterial strains, materials, and growth conditions

The background ("WT") strain is MG1655 (K12) in all cases. Experiments on periplasmic GFP used strain JCW10, in which TorA-GFP is expressed from plasmid pJW1 as previously

described [23]. TorA-GFP is transported to the periplasm by the twin-arginine transport system and the TorA signal peptide is cleaved, leaving free GFP in the periplasm. Under our induction conditions, at least 90% of the green fluorescence comes from GFP that has been transported to the periplasm. This was shown in studies of LL-37 [20] and Cecropin A [18], both of which induced loss of at least 90% of total green fluorescence after permeabilization of the OM and before permeabilization of the CM to Sytox dye. Efficient export of GFP to the periplasm is corroborated in the present work by inspection of transverse intensity linescans, which exhibit two distinct peaks; see below. In the strain JCW1, cytoplasmic GFPmut2 was expressed using the *lac* promoter on the plasmid pMGS053, as previously described [24].

Melittin was purchased from Sigma-Aldrich (M2272). LL-37 was purchased from Anaspec (61302). The hybrid synthetic peptide CM15 with C-terminal amidation was received from Jimmy Feix (Medical College of Wisconsin, Milwaukee). The DNA stains Sytox Green (S7020) and Sytox Orange (S11368), and the membrane dye FM4-64 (T13320) were purchased from Thermo-Fisher Scientific. The Sytox dyes are essentially non-fluorescent in solution phase, but exhibit strong fluorescence on binding to chromosomal DNA.

Bulk cultures were grown in EZ rich, defined medium (EZRDM) [25], which is a MOPS-buffered solution at pH = 7.4 supplemented with metal ions (M2130; Teknova), glucose (2 mg/mL), amino acids and vitamins (M2104; Teknova), nitrogenous bases (M2103; Teknova), 1.32 mM K_2HPO_4, and 76 mM NaCl. Cultures were grown from glycerol frozen stock to stationary phase overnight at 30°C. Subcultures were grown to exponential phase (OD = 0.2–0.6 at 600 nm) at 30°C before sampling for the microscopy experiments.

Minimum Inhibitory Concentration (MIC) Assay

The aerobic MIC values for the various AMPs (**Table 2.1**) were determined using the broth microdilution method as previously described [20]. Two-fold serial dilutions of melittin in EZRDM were performed in separate rows of a polystyrene 96-well plate, with each plate containing an inoculum of *E. coli* MG1655. The inoculum was a 1:20 dilution from a bulk culture at midlog phase (OD_{600} = 0.5) grown at 30°C. The plate was incubated at 30°C and shaken at 200 rpm in a Lab-Line Orbital Environ Shaker (model 3527) for 6 hr. The MIC value was taken as the lowest concentration for which no growth was discernible (<0.05 OD_{600})
after 6 hr.

Microscopy

As previously described [17], imaging of individual cells was carried out at 30°C in a microfluidics chamber consisting of a single rectilinear channel of uniform height of 50 μm and width of 6 mm, with a channel length of 11 mm. The total chamber volume is ~10 μL. After bonding of the PDMS chamber to the glass coverslip, 0.01% poly-L-lysine (molecular weight >150,000 Da) was injected through the chamber for 30 min and rinsed thoroughly with Millipore water. *E. coli* cells are immobilized on the coverslip but grow normally. During imaging experiments, the chamber was maintained at 30°C with an automatic temperature controller.

Single-cell imaging was performed on two different microscopes: a Nikon TE300 inverted microscope with a 100×, 1.3 N.A. phase contrast objective and a Nikon Eclipse Ti inverted microscope with a 100×, 1.45 N.A. phase contrast objective. For the TE300, images were further magnified 1.45× in a home-built magnification box. GFP, Sytox Green, and FM4-64 were imaged using 488 nm excitation (Coherent Sapphire laser), expanded to illuminate the field of view uniformly. Sytox Orange was imaged using 561 nm excitation (Coherent Sapphire laser). Laser intensities at the sample were typically ~5 W/cm^2 at 488 nm and ~2.5 W/cm^2 at 561 nm.

Fluorescence images were obtained with an EMCCD camera, either Andor iXon 897 or Andor iXon 887. In both cases, the pixel size corresponds to 110 ± 10 nm at the sample.

The slower, one-color time-lapse movies were obtained with 50-ms exposure time in each channel, with fluorescence and phase contrast images interleaved at 6-s intervals (12 s per complete cycle). The emission filter was HQ525/50 (Chroma Technology), for GFP, and Sytox Green and D675/50 (Chroma Technology) for FM4-64. For fast one-color movies, fluorescence images only were acquired at 0.5 sec/cycle with 50-ms exposure time. For fast two-color experiments, μManager was used to obtain the data and switch filters between frames using a LB10-NW filter wheel (Sutter). The time-lapse movies were obtained with 50-ms exposure time each, with green fluorescence (488 nm excitation) and red fluorescence (561 nm excitation) (2 sec/cycle). To minimize spectral bleed-through in the two-color experiments, we utilized the narrow filters HQ510/20 for the green channel and HQ600/50M for the red channel.

For the FM4-64 membrane staining assay, MG1655 cells were incubated with 1μg/ml FM4-64 for 10 min before plating on microfluidics chamber. Fresh, pre-warmed, aerated EZRDM was used to wash away unbound cells. After the wash, 10 μM melittin plus 1 μg/ml FM4-64 was injected when taking the movies. To maintain good aeration and steady bulk concentrations, the medium with melittin and FM4-64 was flowed continuously at 0.3 mL/min for a minute first, and then at 0.3 ml/hr for the rest of the experiment.

RESULTS

Timing overview

The series of membrane-related events we are able detect is complex. Details will follow. For the sake of clarity, in **Figure 2.1** we present a composite average timeline showing seven membrane-related events observed after the onset of flow of 10 μM melittin at $t = 0$. We label the times at which specific membrane permeabilization or re-sealing events occur by the sequence t_1, t_2, …, t_7 with the index corresponding to the typical order of events in time. The events include the onset of OM permeabilization to periplasmic GFP (t_1), the onset of "periplasmic bubble" formation (t_2), the onset of CM permeabilization to Sytox Orange (t_3), the onset of CM permeabilization to periplasmic GFP (t_4), the re-sealing of the OM to GFP (t_5), the re-sealing of the CM to GFP (t_6), and the re-permeabilization of both CM and OM to GFP (t_7). **Figure 2.1** is an amalgamation of results from the different experiments described below—no single experiment detects all seven events. The times in **Figure 2.1** are averages across cells measured relative to t_1, the widely variable time of the onset of OM permeabilization and cell shrinkage. Quantitative details of the timing of specific events relative to each other are provided as histograms in **Appendix 2A**. Means and standard deviations are provided in **Table 2.2**.

Transient disruption of the *E. coli* membrane barrier by melittin

The first experiments use the *E. coli* strain JCW10, which expresses GFP that is transported to the periplasm by the Tat system [23]. On excitation at 488 nm, cells exhibit a halo of green fluorescence (**Figure 2.2A, B**), indicating a predominantly periplasmic spatial distribution of GFP. Typically ~90% or more of total GFP has been transferred to the periplasm before the melittin experiment begins [18, 20], as confirmed by the double-peaked transverse intensity linescan (**Figure 2.2B**). Fluorescence images are interleaved with phase contrast images that monitor cell

length vs time to a precision of ±50 nm. One full imaging cycle is completed every 12 s. At least 90% of the 25 cells in a typical field of view exhibit a similar sequence of membrane–related events, but each cell has its own timing.

A representative example is shown in **Figure 2.2** and Movie S1. At t_1 = 36 s, the OM is permeabilized to GFP and the cell shrinks in length (**Figure 2.2C**). This cell loses 37% of its GFP intensity and 20% of its length in less than two camera frames (<24 s). Each cell is different. The fractional GFP loss at t_1 ranges from 36% to 64%, with a mean across cells of ~50%. The spatial distribution of the remaining GFP quickly changes from the periplasmic (halo) distribution to that of a filled cytoplasm (**Figure 2.2B**), indicating CM permeabilization and influx of periplasmic GFP into the larger cytoplasmic volume. Beginning at time t_5 = 60 s, the rate of GFP loss decreases abruptly. (The intervening timing events t_2, t_3, and t_4 will be determined from other experiments.) After a transition period, ~10 times slower leakage of GFP out of the cell envelope continues, as inferred from the subtle decrease in total GFP intensity from t = 5–21 min. Evidently the breach in the cell envelope has largely re-sealed to GFP. At t_7 = 21 min, fast leakage resumes, and by t = 23 min all GFP has been lost to the cell surround. It is not clear from these experiments which membrane(s) (OM or CM or both) have re-sealed over the 21 min interval ($t_5 - t_1$) to contain most of the remaining GFP. Nor is it clear which membrane(s) have "re-permeabilized" to enable complete loss of GFP beginning at t_7 = 21 min.

The distribution of times t_1 between the onset of melittin flow at t = 0 and the onset of GFP loss and cell shrinkage is shown in **Appendix 2A**. Across 40 cells, the mean is $\langle t_1 \rangle = 3.7 \pm 6.4$ min (± one standard deviation). From 12 s/cycle imaging, we can only infer that the time interval ($t_5 - t_1$) during which the OM leaks periplasmic GFP rapidly to the surround is shorter than ~24 s. Sampling at 12 s/cycle is too slow to capture this difference accurately.

Transient formation of invaginations in the CM and pooling of periplasmic GFP

During the same 12 s/cycle movies of periplasmic GFP, in ~30% of cells we observe formation of bright, transient puncta of GFP at essentially the same time as cell shrinkage and loss of ~50% of the GFP intensity. When observed, the puncta typically last only one or two frames, or ~12 s. The bright puncta are evidently caused by pooling of GFP within the periplasm; as soon as a punctum appears, the periplasmic halo of the remaining GFP becomes much dimmer. To test whether such short-lived puncta occur in all cells, we repeated the experiment with periplasmic GFP imaging at the much faster camera rate of 0.5 s/cycle. These faster movies reveal that all cells exhibit transient puncta of GFP fluorescence. Three examples are shown in **Figure 2.3** and Movie S2. In 12 of 18 septating cells, the puncta form in pairs on opposite sides of the septal region (**Figure 2.3B**), suggesting that GFP may sometimes be pooling in a circumferential "donut" structure surrounding the septal region. In non-septating cells, single puncta may form anywhere along the cell periphery. The puncta are typically larger than the diffraction limit in size. Intensity linescans across the puncta have cross sections of ~400–700 nm FWHM. The puncta evidently have sufficient volume to cause pooling of much of the remaining periplasmic GFP within several seconds.

The bright puncta are apparently invaginations in the CM (inward facing periplasmic volumes) rather than blebs in the OM (outward facing periplasmic volumes). The intensity peak of a punctum always moves inward (towards the long cell axis) as the bubble expands. In addition, we use evidence from the higher signal-to-noise images of the membrane stain FM4-64 during addition of melittin (**Appendix 2B**). In those images, the excess membrane always faces inward rather than outward. Furthermore, we see no evidence of outward facing blebs in the phase contrast images. Finally, for cells expressing cytoplasmic rather than periplasmic GFP

(**Appendix 2C**), we observe no transient outward facing GFP bubbles. Evidence below will indicate that the GFP puncta are short-lived because the periplasmic bubbles soon leak GFP into the much larger cytoplasmic volume as well as the cell surround.

Timing of localized disruption of the CM to Sytox Orange

In the 12 s/cycle movies of periplasmic GFP, the periplasmic halo image evolves to a filled cytoplasmic image shortly after the initial loss of GFP intensity (**Figure 2.2A, B**). This indicates CM permeabilization to GFP and concomitant loss of periplasmic GFP to the much larger cytoplasmic volume. To gain more insight into the nature and timing of CM disruption, we obtained a set of two-color, 2 s/cycle movies imaging periplasmic GFP and the DNA stain Sytox Orange. Sytox Orange is non-fluorescent in solution but becomes highly fluorescent on binding to the chromosomal DNA after membranes are compromised. The onset of Sytox Orange fluorescence in a nucleoid spatial pattern marks the time of permeabilization of the OM and CM to small molecules. Such two-color experiments enable direct observation within single cells of the relative timing of OM permeabilization to GFP at t_1, formation of the periplasmic GFP bubble(s) at t_2, CM permeabilization to Sytox Orange at t_3, and nearly complete re-sealing of the cell envelope to GFP at t_5. In the representative septating cell of **Figure 2.4** and Movie S3, the onset of OM permeabilization to GFP precedes the onset of formation of the periplasmic GFP bubble by $(t_3 - t_1) = 4$ s. The onset of OM and CM permeabilization to Sytox Orange is simultaneous with bubble formation within one camera frame: $(t_3 - t_2) \leq 2$ s. The permeability to GFP decreases at t_5, but the permeability of the CM to Sytox Orange persists. The cell envelope leaks GFP rapidly over an interval $(t_5 - t_1) = 32$ s.

Averaged across cells (**Table 2.2**), the periplasmic bubble forms at $\langle(t_2 - t_1)\rangle = 4 \pm 2$ s after the onset of OM permeabilization. Sytox Orange fluorescence begins to rise within

$\langle(t_3 - t_2)\rangle$ = 1 ± 1 s of the onset of bubble formation. In all septating cells, the bubble already begins to leak Sytox Orange across the CM while it gathers GFP from the rest of the periplasm. Bubble formation and leakage of Sytox Orange into the cytoplasm occur in parallel with leakage of GFP to the cell surround. The Sytox Orange signal continues to rise for at least 2 min after the cell envelope has re-sealed to GFP.

For septating cells, Sytox Orange always enters the cytoplasm at the septal location. This is seen clearly in the axial linescans of Sytox Orange intensity vs time, which show a staining pattern that evolves outward from punctal to the characteristic lobal pattern of the nucleoids (example in **Figure 2.4C**) [26]. The pattern is consistent with the suggestion that Sytox Orange is leaking across the CM and into the cytoplasm through the periplasmic bubble. Melittin itself likely enters the cytoplasm by the same pathway. In sharp contrast, for non-septating cells Sytox Orange always enters the cytoplasm at one endcap, after which the signal slowly spreads across the entire nucleoid (example in **Appendix 2D**). For non-septating cells, the location of the periplasmic GFP bubble seems unrelated to the position of localized entry of Sytox Orange into the cytoplasm.

Timing of OM and CM permeabilization and re-sealing to GFP

Finally, we return to the 0.5 s/cycle, one-color movies of periplasmic GFP in an effort to understand the timing of permeabilization and re-sealing events of the OM and CM with respect to GFP. Detailed analysis of the same septating cell shown in **Figure 2.3A** and Movie S2 follows. We are attempting to dissect three signals: the loss of total GFP from the cell envelope, the growth and decay of the periplasmic bubble, and the transport of GFP through the bubble into the cytoplasm. Accordingly, we measure intensity vs time within three different regions of interest (ROI), as shown in **Figure 2.5A**. The first ROI measures total fluorescence from the

entire cell, shown by the $T(t)$ trace in **Figure 2.5C**; *T* stands for total. The second ROI is a small box that covers the location where the periplasmic GFP bubble will grow and shrink, shown by the trace $B(t)$ in **Figure 2.5C**; *B* stands for bubble. This ROI includes some cytoplasm, some periplasm, and some extracellular space. The third ROI comprises the sum of intensities within two small boxes that lie within the cell body far from the bubble location, $C(t)$ in **Figure 2.5C**. $C(t)$ stands for cytoplasm; it is intended to report primarily on leakage of GFP into and out of the cytoplasm. However, it includes ~10% periplasmic volume. As shown in transverse linescans of the 2D projected images of periplasmic and cytoplasmic GFP (**Figures. 2.2B and 2.5B**), $C(t)$ inevitably responds to changes in GFP intensity within the periplasm as well. The intensities $B(t)$, $C(t)$, and $T(t)$ are background-corrected, mean intensities over each ROI. They are not normalized to each ROI area. The absolute magnitudes are not to be compared.

For the cell in **Figure 2.5**, total intensity $T(t)$ shows rapid loss of GFP to the surround beginning at t_1 = 42 s after addition of melittin. This rapid loss continues until t_5 = 53 s, when the rate of loss slows down by about a factor of four. The slower loss of intensity after t = 53 s is real. The rate of photobleaching, as judged by the slope of $T(t)$ at t < 40 s, is much slower. The intensity in the bubble ROI $B(t)$ shows a dip in the range t = 40–43 s. This is due to loss of periplasmic GFP to the surround prior to bubble formation, the same loss detected less sensitively by $T(t)$. We assign the onset of bubble formation to t_2 = 43 s, when $B(t)$ reaches a minimum and begins to rise. From t = 43–49 s, the bubble is inflating. Its intensity peaks at t = 49 s and then decreases, first rapidly and then more slowly. The intensity $C(t)$ remains constant until the same t = 43 s, when it begins to decrease. We attribute this to loss of periplasmic intensity as the bubble grows. Recall that $C(t)$ is a mixture of periplasmic and cytoplasmic signals, with the periplasmic component dominant at early times. $C(t)$ reaches a minimum at t_4 =

49 s, when it begins to rise. This time point marks the onset of leakage of GFP from the bubble, across the CM, and into the cytoplasm. Accordingly, the intensity in the central part of the transverse linescan begins to increase (**Figure 2.5B**). Notice that t_4 coincides with the peak in $B(t)$. We interpret the subsequent rapid decrease in $B(t)$ to simultaneous, parallel loss of bubble intensity to both the cytoplasm and the cell surround. When the rate of loss of $B(t)$ slows down at t_5, $C(t)$ is still rising. Evidently it is the OM, not the CM, that has mostly re-sealed against GFP. The distribution of intervals $(t_5 - t_1)$ during which the OM leaks GFP rapidly has mean $\langle(t_5 - t_1)\rangle = 13.3 \pm 3.9$ s (**Appendix 2A**, **Table 2.2**). Loss of intensity of $B(t)$ slows down even further at $t >$ 65 s, when entry of GFP into the cytoplasm has effectively ceased. We designate $t_6 \sim 65$ s as the time at which the CM has re-sealed to GFP. Beyond t_6, $C(t)$ remains constant. At the same t_6, the rate of loss of bubble intensity $B(t)$ decreases, but $B(t)$ continues to lose intensity very slowly. We attribute the very slow loss at $t > 65$ s as a continuing slow leak through the OM. Accordingly, for $t > 65$ s the decay rate of $T(t)$ appears similar to that of $B(t)$.

Notice that the CM remains permeable to GFP for some 13 s $(t_6 - t_5)$ after the OM has mostly re-sealed to GFP. These seem to be independent events. Both CM and OM are simultaneously quite permeable to GFP only for the short time period $(t_5 - t_4) = 4$ s. This short interval explains why experiments imaging cytoplasmic GFP after melittin addition (**Appendix 2C.A**) show little or no loss of GFP on the several minute timescale of the early OM and CM permeabilization events. Finally, at much longer time $t_7 \sim$ 2–20 min (not shown in **Figure 2.5**), both membranes have become permeable to GFP once again, and the cell drains completely.

Our measurements provide no information about the molecular-level nature of the permeabilization sites. However, the timescale of GFP leakage during different events provides some indication of the degree of permeability of the OM or CM to GFP at each stage of the

attack. These timescales vary significantly. The initial loss of GFP through the OM is rapid, occurring on average in $<(t_5 - t_1)>$ ~13 s. Transfer of GFP from the bubble through the CM and into the cytoplasm is comparably rapid, $<(t_6 - t_4)>$ ~ 13 s. In contrast, when melittin attacks cells expressing cytoplasmic GFP (**Appendix 2C.A**), the final leakage from cytoplasm to the cell surround beginning at t_7 is very slow, typically occurring over ~4 min. This loss is apparently limited by the combined CM and OM permeability, not by GFP diffusion in the cytoplasm [27-28]. For comparison, in the attack of LL-37 on cells expressing cytoplasmic GFP, the cytoplasm typically drains entirely in ~20 s or less after membrane permeabilization (example in **Appendix 2C.B**). The underlying cause of the bottleneck to the final stage of melittin-induced GFP leakage is not clear.

DISCUSSION

Melittin interactions with model lipid bilayers

There is an extensive literature describing interactions of AMPs with model lipid bilayers in the form of small or large unilamellar vesicles (SUVs or LUVs), giant unilamellar vesicles (GUVs), cushioned planar bilayers, and, most recently, *E. coli* cytoplasmic membranes in the form of spheroplasts [3-7, 11]. Melittin is probably the peptide most often studied by these methods. A persistent question is the relevance of such studies of model membranes to the mechanisms by which AMPs interact with real bacterial membranes. Because the present work provides the most detailed account thus far of melittin interactions with bacterial membranes, an attempt to find connections seems worthwhile.

In experiments on model lipid bilayers, melittin apparently exhibits different behaviors at low vs high peptide-to-lipid (P/L) ratios, and also for zwitterionic vesicles (typically POPC) vs vesicles containing 30–100% anionic lipids (typically POPG). In 1998, Schwarz and co-workers

observed graded (partial) release of dye from zwitterionic vesicles induced by melittin at low P/L ratios on the order of 1/1000 [3]. Graded release indicates that vesicles were transiently permeabilized to the dye, but re-sealed on the timescale of complete release of dye content. They attributed the partial release to formation of transient pores. Quantitative modeling yielded a very short estimated pore lifetime, below ~10 ms. Transient permeabilization by melittin at low P/L ratio was corroborated more recently in studies of both zwitterionic and mixed zwitterionic/anionic vesicles by Wimley and Hristova [5-6]. Melittin interactions with bilayers may also depend on the degree of hydration of the sample. Stable, equilibrium pores were observed in low-hydration multilayers [7], while similar P/L ratios caused transient permeabilization at high hydration [5-6].

An appealing mechanism for transient pore formation at low P/L invokes the build-up of curvature stress (the "wedge effect") as melittin binds initially to the outer leaflet of the vesicle [5, 7]. Eventually the stress induces vesicle rupture (attributed to pore formation) and dye release. The same rupture enables translocation of melittin to the vesicle inner leaflet. Equilibration of melittin density across the two leaflets alleviates the asymmetric curvature stress and the pore re-seals. For melittin at low P/L, at equilibrium the bilayer is once again impermeable to dye. There are no persistent pores.

There is also evidence that melittin can induce membrane disruptions (perhaps toroidal pores) large enough to pass a small globular protein such as the 27 kDa GFP. In 1982, DeGrado and co-workers showed that melittin transiently permeabilized erythrocytes to hemoglobin [29]. They attributed the re-sealing process to translocation of melittin across the membrane, similar to the mechanism invoked here. In a 2001 study of purely anionic vesicles (100% POPG), Ladokhin and White [4] found that melittin at high P/L ratios >1/35 induced membrane disruptions

that leaked both small and larger fluorescently labeled dextrans (4 kDa and 50 kDa) with comparable efficiency. While the disruptions were ascribed to a "detergent-like" mechanism, they could equally well have been pores of diameter ~3 nm. In 2001, such large, melittin-induced pores were detected quite directly by Huang and co-workers in fully hydrated, oriented multilayers using in-plane neutron scattering [10]. For melittin at P/L > 1/30 on POPC multilayers, D_2O-filled pores of inside diameter 4.4 nm were inferred. At the same high P/L ratios, oriented circular dichroism showed that most of the melittin helices were inserted into the bilayer (perpendicular orientation). The inferred structure was that of a toroidal pore lined by a mixture of melittin and lipid molecules. A recent study showed that melittin at P/L of 1:50 enabled passage of 10 kDa dextran across lipid vesicle bilayers. A synthetic melittin variant "MelP5" showed permeabilization of vesicles to both 10 kDa dextran and 24 kDa chymotrypsin at P/L ratios as low as 1:500 [30].

In 2013 the Huang lab studied melittin interactions with anionic GUVs made of 7:3 POPC:POPG [7]. Stable permeabilization to small dye molecules occurred only at high P/L ratios in excess of 1/45. The permeabilization persisted on a timescale of hours, strongly suggesting an equilibrium state. Recently the same lab has studied the interaction of melittin with large spheroplasts made of *E. coli* cytoplasmic membrane [11, 31]. Comparably stable permeabilization was observed in the spheroplasts [11]. The proposed mechanism invokes initial formation of transient pores due to the same outer leaflet curvature stress invoked before to explain graded dye release from vesicles. Such transient pores would enable melittin translocation, which leads to build-up of positive curvature stress in both leaflets. At sufficiently high P/L, the equilibrium state has equal melittin concentration in both GUV leaflets and includes stable permeabilization sites, possibly due to toroidal pores, that incorporate excess

melittin in an orientation perpendicular to the plane of the membrane. The stable pores would thus relieve membrane tension caused by apposition of two leaflets, both with positive curvature stress, in a planar geometry.

Proposed mechanism of membrane permeabilization and re-sealing steps

The present work provides strong evidence of melittin-induced transient permeabilization of both the OM and CM of live *E. coli* to GFP. Membranes permeable to GFP will enable melittin translocation and will leak other small proteins as well as a host of small ions and neutral molecules. The GFP permeabilization sites tend to occur at curved membrane surfaces (both septa and endcaps), where the anionic phospholipids cardiolipin (CL) and phosphatidylglycerol (PG) are known to concentrate. The sites are localized, but we cannot determine whether the membrane disruptions are pore-like or less organized. The transient OM and CM disruptions live ~10 s, after which they re-seal to GFP. Some 2–20 min later, both membranes have re-permeabilized to GFP.

In contrast to most vesicle experiments, our flow experiments hold the external melittin concentration constant at 10 μM, providing an unlimited supply of the AMP to the plated bacterial cells. As time progresses, the total concentration of melittin within a cell builds up from the outside in. The mean total concentration of a cationic AMP in an *E. coli* cell, averaged over all internal components, can become very high [32-33]. For the synthetic peptide ARVA, Wimley showed binding of ~10^7–10^8 peptides per cell, corresponding to a mean concentration in the low-mM range [32]. In effect, our experiments likely sweep the membrane-bound melittin concentration over a very wide range of P/L ratios during the 30 min observation time.

The real *E. coli* cell envelope is structurally and compositionally much more complex than a unilamellar membrane comprising pure lipids. Comparisons with model lipid bilayers are necessarily speculative. Nevertheless, we can paint an appealing mechanistic picture that

incorporates ideas first generated to explain the vesicle experiments. We imagine an initial buildup of melittin in the anionic LPS layer; melittin gradually penetrates to the outer leaflet of the OM, generating curvature stress. This leads to membrane disruption and the initial leakage of periplasmic GFP to the cell surround (t_1). The disruption enables rapid translocation of melittin into the periplasm, where it binds to the PG layer, inducing cell shrinkage. The envelope shrinkage forces shrinkage of the CM, which invaginates to form inward-facing periplasmic bubbles (t_2). (See the proposed explanation below.) As melittin concentration builds up within the periplasm, it binds to the inner leaflet of the OM, relieving the curvature stress and causing nearly complete re-sealing of the OM to GFP (t_5).

Meanwhile the same process of differential curvature stress repeats itself on the inside leaflet of the periplasmic bubble (the outer leaflet of the CM), which soon bursts and begins to leak Sytox Orange (t_3), GFP (t_4), and presumably melittin into the cytoplasmic space. Melittin density on the outside bubble leaflet (the inner leaflet of the CM) then builds up to re-seal the bubble to GFP (t_6). Evidently the CM remains permeable to Sytox Orange and, by inference, to melittin, throughout OM and CM permeabilization and re-sealing to GFP. We suggest that melittin continues to translocate across both OM and CM, causing a gradual buildup of curvature stress in both leaflets of both membranes. That buildup occurs slowly, over ~8 min, in part because binding of melittin to both membranes is competing with binding to a variety of anionic bacterial components. These include the LPS layer of the OM; within the periplasmic space, the PG layer and anionic glycopolymers, proteins, and lipids; and within the cytoplasmic space, the chromosomal DNA, ribosomes, lipids, and a host of soluble anionic proteins and RNAs. These anionic components evidently act as highly absorbent sinks for cationic AMPs [32-33]. Eventually, both OM and CM re-permeabilize to GFP and all residual GFP is lost to the surround (t_7).

The timescale of re-sealing of the OM and CM to GFP is ~10 s, much longer than the lifetime of ~10 ms for the pores that leak dye from vesicles in the low P/L ~ 1/1000 regime. It seems unlikely that the pores in these two different types of experiment are closely related. Our speculative mechanism requires GFP-sized pores that open at much higher P/L ratios and then subsequently close. Such large, transient pores have not been observed in vesicle experiments, which have focused on dye efflux.

Proposed mechanism of cell shrinkage and periplasmic bubble formation

How does melittin cause the initial cell shrinkage event and concomitant formation of the inward-facing periplasmic bubbles? Here we propose a novel mechanical concept that couples binding of melittin to the peptidoglycan (PG) layer with cell shrinkage and bubble formation. The PG layer is a single gigantic molecule comprising a meshwork of circumferential glycan strands crosslinked to each other by short, flexible peptide chains oriented longitudinally [21]. The peptide linkers contain two anionic amino acids each. The PG layer is longitudinally elastic but circumferentially stiff. It is covalently bound to lipoproteins whose hydrocarbon tails are embedded in the inner leaflet of the outer membrane. The high concentration of neutral and ionic solute molecules in the cytoplasm causes influx of excess water, resulting in a large turgor pressure that drops across the PG/OM layer [34]. Mechanical equilibrium is attained when the turgor pressure is balanced by the restoring force of the stretched PG layer, which expands beyond its equilibrium size. This is analogous to blowing up a balloon.

We propose that binding of cationic AMPs to the anionic peptide crosslinks changes the physical properties of the PG layer, in effect increasing its longitudinal stiffness (elastic modulus). If the turgor pressure remains essentially constant while the elastic modulus of the PG layer increases, the PG layer will contract. Mechanical equilibrium will be re-established at a

shorter overall length of the cell envelope. This is a plausible explanation for the shrinkage of cell length as cationic AMPs enter the periplasm. If it is correct, we would expect the rate of shrinkage of cell length to mimic the rate of build-up of the cationic AMP concentration in the periplasmic space. Our original study of LL-37 [20] used a rhodamine fluorescent label on the AMP itself, fortuitously enabling direct observation of the build-up of Rh-LL-37 in the periplasm as a wave of dequenched red fluorescence that slowly expanded from septum to cell tips. Independent experiments demonstrated that Rh-LL-37 indeed binds to purified peptidoglycan. In the example of Fig. 2 of Ref. 20, the shrinkage of cell length and the build-up of periplasmic Rh-LL-37 intensity both occur gradually on the same timescale, over ~8 min. This behavior is consistent with our suggestion that AMP binding leads to compression of the PG layer and longitudinal cell shrinkage.

What happens to the OM and the CM as the PG layer contracts in length? Both membranes suddenly have excess surface area. The OM is covalently bound to the PG layer by proteolipids. It could form ruffles or blebs [35], it could mechanically de-couple from the PG layer by releasing lipoprotein copies, or it could bud off LPS vesicles to the surround. Our present methods do not discern blebs and would be insensitive to ruffles or small vesicles. In contrast, the CM is only weakly mechanically coupled to the PG layer, if at all, and the shrinking PG layer encloses the CM. As the PG layer contracts axially, the CM must somehow shrink its effective length. It could ruffle, it could bud off internal vesicles, or it could invaginate. Our observation of the inward-facing septal periplasmic bubbles induced by melittin indicates that the CM in fact invaginates. The surface area of a bubble can account for the cylindrical surface area lost in a 15% shrinkage event. The surface area of a periplasmic bubble of radius $r_{\mathrm{bubble}} \sim 300$ nm is S_{bubble}

$= 4\pi r_{bubble}^2 \sim 1.1\ \mu m^2$. This is indeed 15% of the cylindrical surface area of a cell of radius $R_{cell} \sim$ 400 nm and cylindrical length $L \sim 3\ \mu m$: $S_{cylinder} = 2\pi R_{cell} L \sim 7.5\ \mu m^2$.

This is the only mechanism we can imagine that explains large invaginations in the CM, *i.e.*, inward facing bubbles. As melittin accumulates in the periplasm, it first binds differentially to the outer leaflet of the CM, part of which forms the "inside leaflet" of the bubble. This creates positive curvature stress on the CM. In unconstrained space, this type of stress would induce outward facing blebs, not inward facing bubbles. Our model instead supposes that the mechanical constraint imposed by the shrinking PG layer forces the bubble to grow inward, taking up extra surface area and relieving the axial stress due to PG layer shrinkage. As melittin continues to accumulate preferentially in the inside leaflet of the bubble bilayer (the outer leaflet of the CM), the resulting curvature stress causes the bubble to rupture in a few seconds. This connects the bubble volume to the cytoplasmic volume and enables Sytox Orange and periplasmic GFP to enter the cytoplasm. The re-sealing of the bubble to GFP may occur as sufficient melittin translocates to the cytoplasm where it gains access to the outside leaflet of the bubble (inner CM leaflet), thus relieving the curvature stress.

Septal periplasmic GFP bubble formation evidently occurs for both melittin and CM15. For melittin, the septal bubbles remain connected to the periplasmic space and soon become leaky to the cytoplasm as well. For CM15, the bubbles evidently isolate GFP from both the periplasmic space and the cytoplasm, as if a stable, internal giant unilamellar vesicle (GUV) has formed (**Appendix 2F** and Movie S4). While appealing for melittin, proposed mechanism does not explain the observation that CM15 induces stable "internal GUVs".

Comparisons across antimicrobial peptides

By now we have used single-cell imaging methods to directly observe the attack of a variety of antimicrobial peptides on live *E. coli*, including LL-37 [20], cecropin A [18], melittin, and CM15 (a synthetic cecropin A/melittin hybrid) [17]. All are positively charged, but they vary in sequence, length, and charge density (**Table 2.1**). The observed membrane phenomena and the sequence of events vary significantly across these peptides.

For the longer peptides LL-37 and cecropin A, the initially observed events were abrupt shrinkage of cell length by 15–20% and essentially complete loss of periplasmic GFP to the cell surround. No periplasmic GFP bubbles were observed, perhaps because the rapid loss of GFP to the cell surround precluded their observation. No membrane re-sealing events were observed, perhaps for the same reason. The two shorter peptides CM15 and melittin behave similarly to each other. In both cases, part of the periplasmic GFP intensity is lost almost simultaneously with cell shrinkage. The OM evidently re-seals and much of the remaining periplasmic GFP then moves inward into the cytoplasm. For septating cells, both peptides induce periplasmic bubbles of GFP intensity at the septal region. See **Appendix 2F** and Movie S4 for the CM15 data. Only much later do both CM and OM re-permeabilize, enabling complete loss of GFP to the cell surround. For melittin, the periplasmic GFP bubbles quickly drain. For CM15, the GFP bubbles persist, even after complete loss of GFP from both cytoplasm and periplasm.

For all four AMPs, septating cells are attacked earlier than non-septating cells and curved membrane surfaces are preferentially permeabilized (septal region and endcaps; see **Appendix 2F**). We speculate that the sensitivity of curved membranes to permeabilization by cationic AMPs may be due in part to the higher concentration of the anionic lipids cardiolipin and phosphatidyl glycerol at those locations. Localized permeabilization (consistent with pore

formation) seems quite general across AMPs. There are subtle differences in the patterns of OM and CM attack. For example, for septating cells cecropin A permeabilizes the OM at the septal region but the CM at one endcap. LL-37 and melittin permeabilize both OM and CM in the septal region (**Appendix 2E**).

Finally, we contrast the effects on *E. coli* of **MM_{63}:CHx_{37}**, a highly cationic random copolymer of β-peptide subunits with mean length of ~35 subunits and mean charge of ~+22. Like melittin and CM15, the random copolymer induced inward movement of periplasmic GFP, indicating translocation across the OM without complete permeabilization to GFP [16]. However, the first observation was cell shrinkage (by only ~9%) and formation of what we called "endcap periplasmic GFP bubbles". The copolymer-induced bubbles localized at both endcaps; they are highly reminiscent of the plasmolysis spaces induced by abrupt external osmotic upshift. We believe that the osmotic effects due to translocation of **MM_{63}:CHx_{37}** and a host of accompanying anions into the periplasm cause the endcap bubbles. As a result, the osmolality of the periplasm increases, much as it does after an abrupt external osmotic upshift. The result is loss of cytoplasmic water and eruption of endcap plasmolysis spaces. In contrast, the osmotic effects are much smaller when a more moderately charged +6 CM15 or melittin molecule enters the periplasm and binds to the PG layer. For these reasons, we believe the endcap periplasmic bubbles induced by **MM_{63}:CHx_{37}** are plasmolysis spaces caused by an effective osmotic upshift in the periplasm, while the septal periplasmic bubbles induced by melittin and CM15 are not.

CONCLUSION

It is increasingly clear that introduction of a high concentration of polycationic peptide into an *E. coli* cell, most of whose biopolymer content is polyanionic, wreaks havoc in a variety of ways. However, it all begins with permeabilization of the OM and CM to the peptide itself. Here

we have characterized the spatiotemporal effects of melittin on the *E. coli* membranes in great detail. For both the OM and the CM, we have observed membrane permeabilization, nearly complete re-sealing, and subsequent re-permeabilization to the globular protein GFP. We speculate that a mechanism invoking transient permeabilization and permanent re-permeabilization, both due to the build-up of membrane curvature stress, might prove to be common to both bacterial membranes and model lipid bilayers. However, the variety and specificity of the effects of different AMPs on *E. coli* membranes remains surprising. The spatiotemporal complexity observed here goes well beyond the effects observed thus far in model lipid bilayers.

Author Contributions

ZY, HC, and JCW all contributed to design of the project. ZY and HC performed the experiments. ZY and JCW analyzed the data and wrote the manuscript. HC helped edit the manuscript.

ACKNOWLEDGMENTS

This research was supported by the National Institute of General Medical Sciences of the National Institutes of Health under awards R01GM094510 (to JCW as PI) and R01GM093265 (to JCW and Samuel Gellman as co-PIs). The content is solely the responsibility of the authors and does not necessarily represent the official views of the National Institutes of Health.

Table 2.1 Antimicrobial agents compared in this work.

Antimicrobial Agent	Sequence	Net Charge	MIC (μM) [1]
LL-37	***LLGDFFRKSKEKIGKEFKRI-VQRIKDFLRNLVPRTES***	+6	4
Cecropin A	**KWKLFKKIEKVGQNIRDGII-KAGPAVAVVGQATQIAK-NH_2**	+7	0.9
Melittin	***GIGAVLKVLTTGLPALISWI-KRKRQQ*-NH_2**	+6	5
CM15	**KWKLFKKIGAVLKVL-NH_2**	+6	5
β-peptide copolymer MM_{63}:CHx_{37}	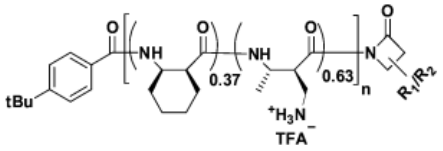	63% cationic sidechains	25 μg/mL

[1] Minimum inhibitory concentration (in μM) over 6-hr period in aerated EZRDM medium at 30°C, determined by OD for successive two-fold dilutions in 96 well plates. Copolymer **MM_{63}:CHx_{37}** lacks a defined molar mass, so MIC is in μg/mL.

Table 2.2 Summary of timing measurements.[1]

Experiment	Measurement	*N*	Mean ± SD (s)	Range (s)
ppGFP + phase contrast 12 s/cycle	t_1	40	3.7 ± 6.4 (min)	0.2 – 25.2 (min)
	$t_7 - t_1$	26	7.5 ± 5.4 (min)	1.8 – 20.4 (min)
ppGFP + Sytox Orange 2 s/cycle	$t_2 - t_1$	25	4 ± 2	2 - 8
	$t_3 - t_2$	25	1 ± 1	0 - 6
ppGFP only 0.5 s/cycle	$t_4 - t_2$	33	4.3 ± 2.3	1.5 – 12.5
	$t_5 - t_4$	24	3.8 ± 1.4	1 – 6.5
	$t_5 - t_1$	36	13.3 ± 3.9	6.5 – 23
	$t_6 - t_4$	23	13.1 ± 8.3	2.5 – 30.5

[1] Notation for events as follows. $\boldsymbol{t_1}$: onset of OM permeabilization to GFP. $\boldsymbol{t_2}$: onset of periplasmic GFP bubble formation. $\boldsymbol{t_3}$: onset of CM permeabilization to Sytox Orange. $\boldsymbol{t_4}$: Onset of CM permeabilization to GFP. $\boldsymbol{t_5}$: Re-sealing of OM to GFP. $\boldsymbol{t_6}$: Re-sealing of CM to GFP. $\boldsymbol{t_7}$: Re-permeabilization of both CM and OM to GFP. See Figure 2.1 for average timeline of events. See Appendix 2A for histograms of the various timing distributions. *N* is the number of individual cells in each sample. The ± values are one standard deviation of single measurements. Values in seconds except as noted.

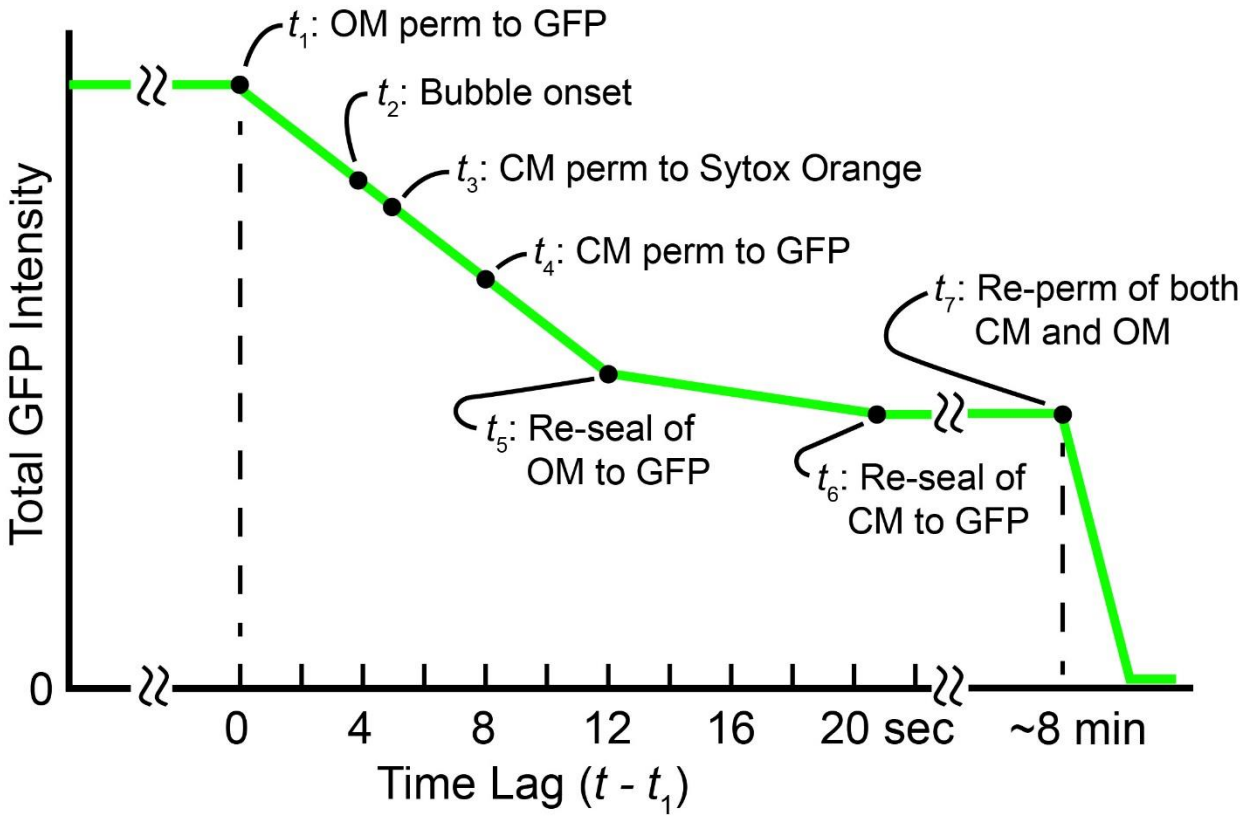

Figure 2.1 Time line summarizing the seven membrane-related events observed following initiation at $t = 0$ of flow of 10 μM melittin (2X MIC) over plated *E. coli* cells expressing periplasmic GFP. Time lags are measured relative to the initial cell shrinkage and OM permeabilization event at t_1. See Table 2.2 and Appendix 2A for mean values and histograms of each quantity across cells.

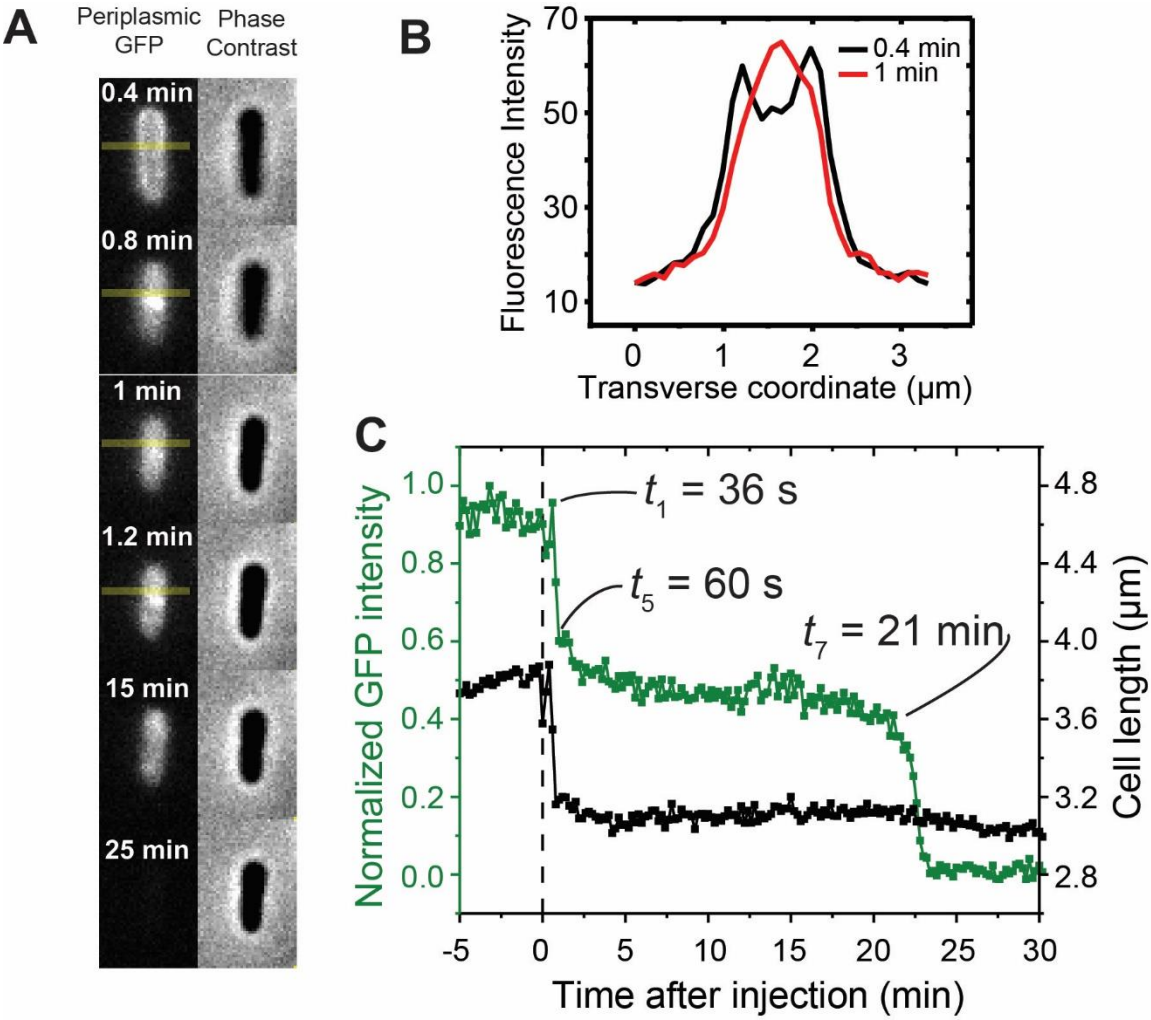

Figure 2.2 Example of effects of 10 μM melittin (2X MIC) on a single, representative *E. coli* cell expressing periplasmic GFP in aerobic growth conditions at 30°C. The frame rate is 12 sec/cycle, and flow of melittin begins at $t = 0$. **(A)** Phase contrast and fluorescence snapshots. **(B)** Transverse intensity profiles along the yellow line shown in panel **A**. The profile is periplasmic before adding melittin and cytoplasmic shortly after adding melittin. **(C)** Time dependence of cell length (from phase contrast images) and total GFP fluorescence intensity. The abrupt 37% decrease in GFP fluorescence intensity coincides with cell shrinkage. Most remaining GFP is trapped inside the cell envelope until $t = 22$ min. *Scale:* The width of an *E. coli* cell under our growth conditions is 900 nm.

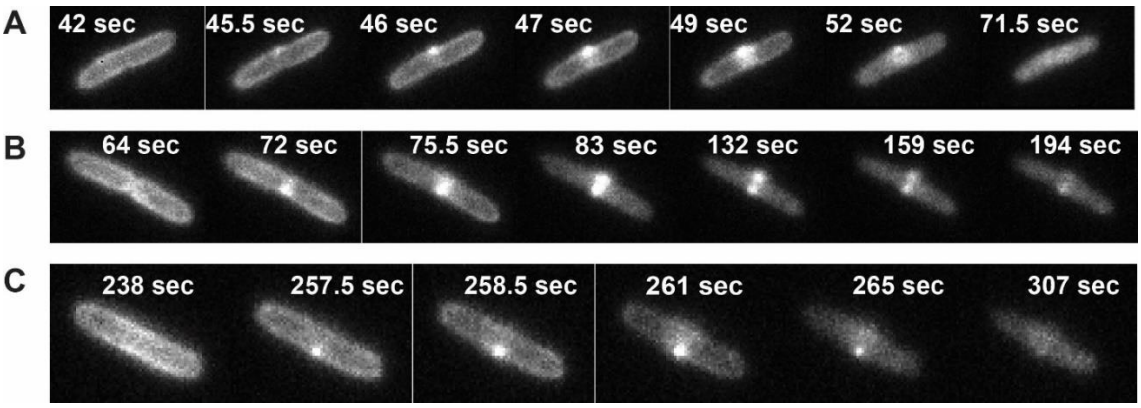

Figure 2.3 Fluorescence snapshots of single *E. coli* cells expressing periplasmic GFP in aerobic growth conditions following addition of 10 μM melittin at $t = 0$. Images acquired at 0.5 sec/cycle. **(A)** A septating cell that forms one periplasmic GFP bubble at the septal region. **(B)** A septating cell that forms a pair of periplasmic GFP bubbles at the septal region, possibly indicating an annular (donut-like) invagination. **(C)** An apparently non-septating cell that forms one periplasmic GFP bubble. *Scale:* The width of an *E. coli* cell under our growth conditions is 900 nm.

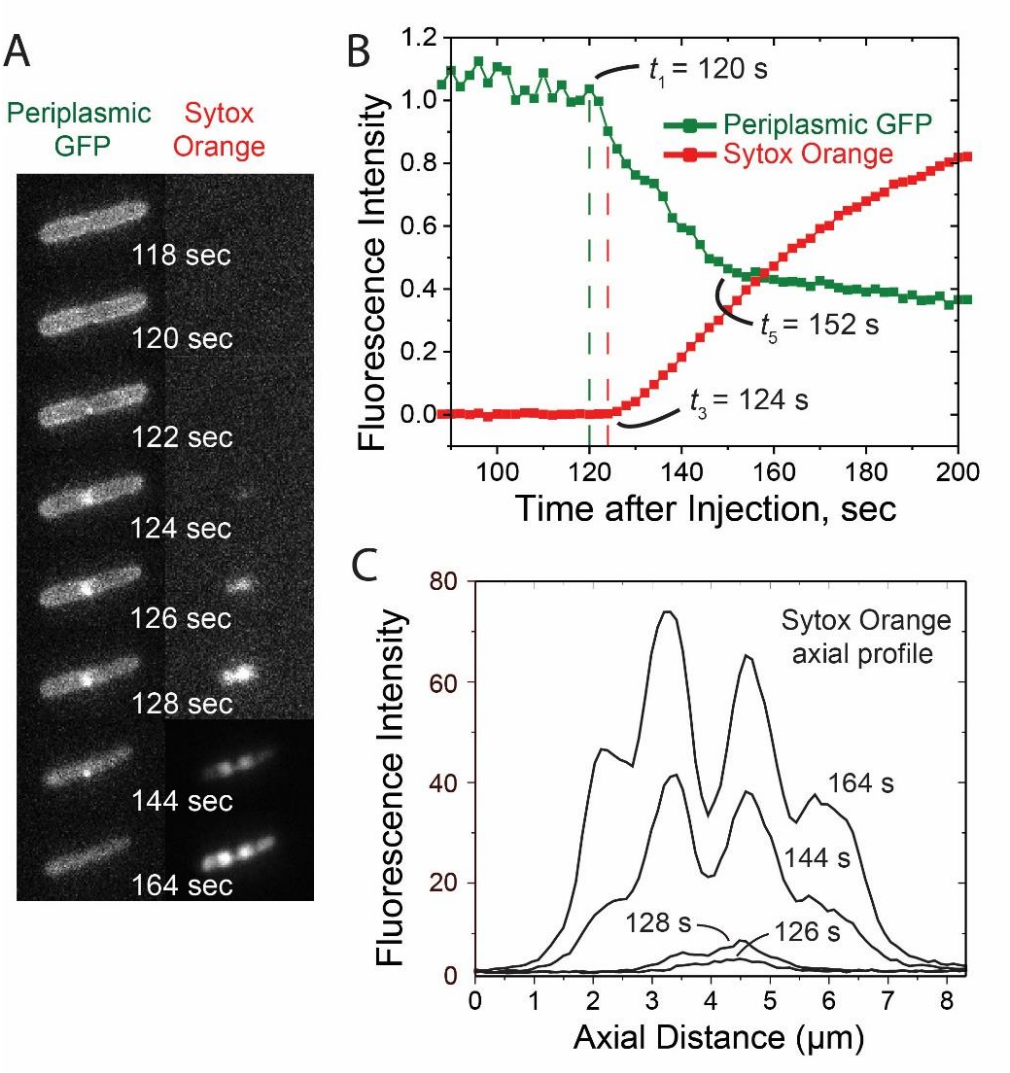

See next page for the figure legend

Figure 2.4 Timing of total fluorescence intensity of GFP and Sytox Orange from two-color imaging of the same cell. The camera alternates acquisition of green and orange fluorescence images at 2 sec/cycle. **(A)** Fluorescence snapshots of a single *E. coli* cell expressing periplasmic GFP in aerobic growth conditions, following addition of 10 μM melittin and 5 nM Sytox Orange beginning at $t = 0$. *Left:* GFP. *Right:* Sytox Orange. Image brightness for snapshots prior to 144 s was enhanced 14X to enable visualization of weak signals. **(B)** Time dependence of total fluorescence intensity in each channel for the cell shown in **A. (C)** Axial intensity distribution of Sytox Orange fluorescence at different time points as shown. Sytox Orange first appears near the septal region, then spreads gradually to the entire cell. The four-peaked distribution at long times is characteristic of the axial distribution of the nucleoids (chromosomal DNA). *Scale:* The width of an *E. coli* cell under our growth conditions is 900 nm.

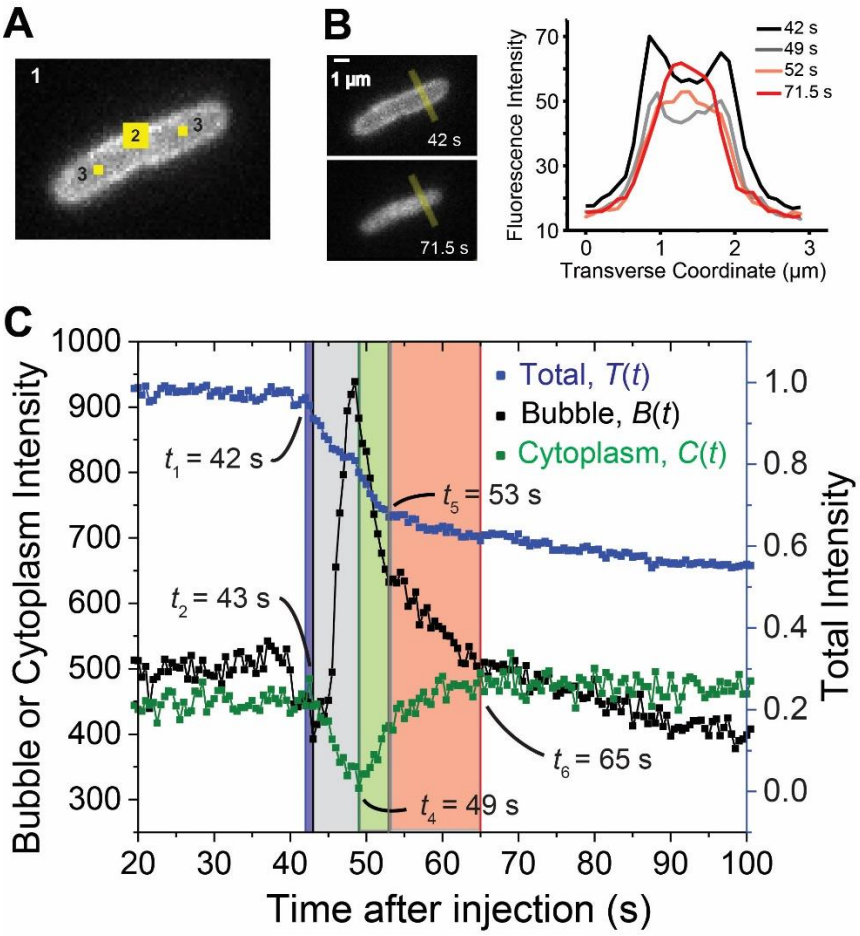

See next page for the figure legend

Figure 2.5 Time evolution of total GFP fluorescence intensity $T(t)$, GFP intensity in the region where the periplasmic bubble forms $B(t)$, and GFP intensity in a region sampling primarily cytoplasmic GFP $C(t)$. The cell under study is the same one shown in Figure 2.3A. Image acquisition occurs at 0.5 sec/cycle. **(A)** Regions of interest 1, 2, and 3 are used for total GFP intensity, GFP bubble intensity, and cytoplasmic GFP intensity. **(B)** *Left:* Fluorescence snapshots of the representative cell before and after melittin injection. *Right:* Transverse intensity profiles along the yellow lines of panel **B**. **(C)** Time dependence of total GFP intensity in the three regions of interest. Permeabilization and re-sealing events marked as t_1, t_2, t_4, t_5, and t_6 denote the onset of OM permeabilization to GFP, the onset of periplasmic GFP bubble formation, the onset of CM permeabilization to GFP, the time of re-sealing of the OM to GFP, and time of re-sealing of the CM to GFP, respectively. See text and Figure 2.5. *Scale:* The width of an *E. coli* cell under our growth conditions is 900 nm.

Appendix

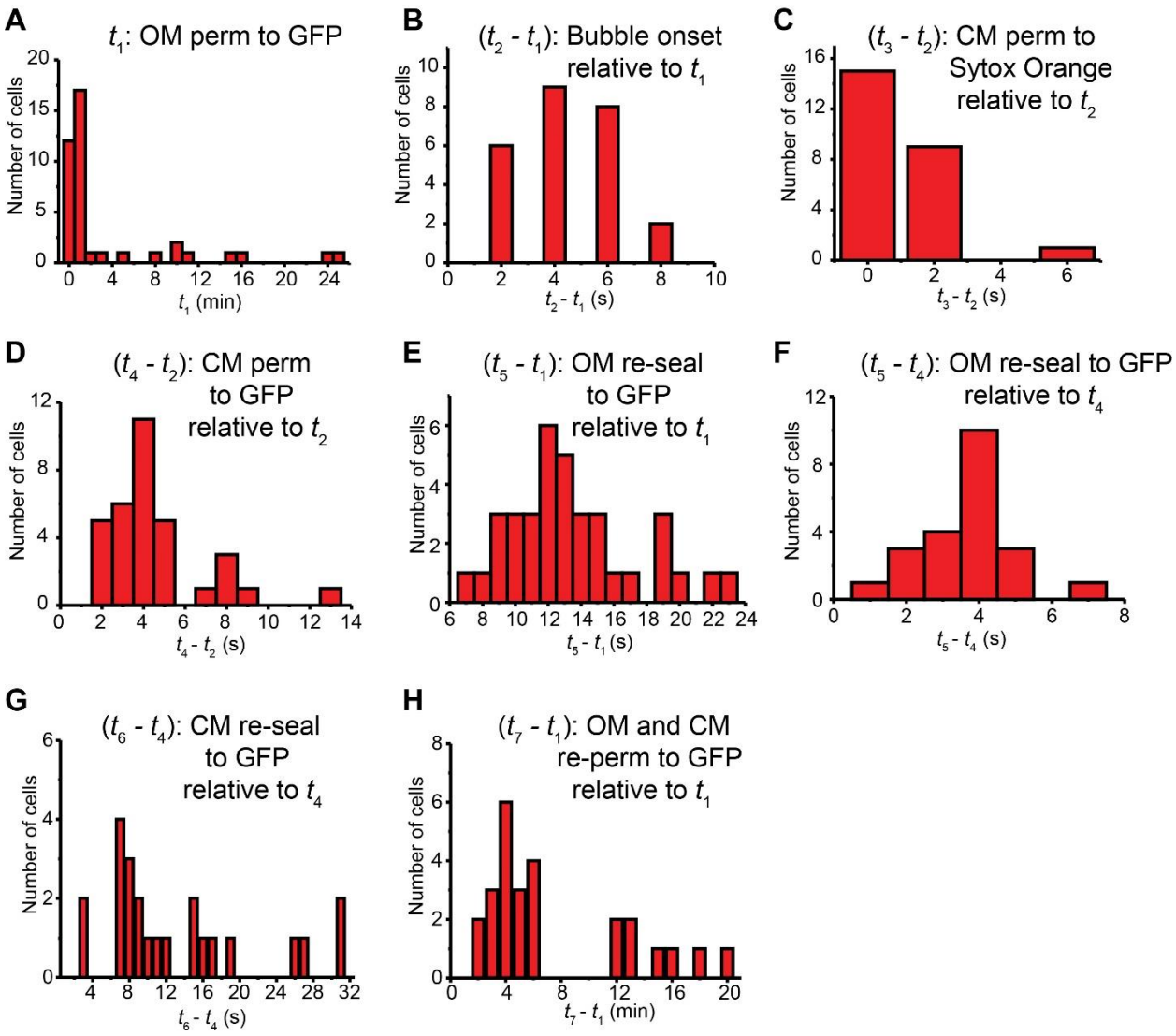

See next page for the figure legend

Appendix 2A. Histograms of lag times of the seven membrane events across different cells after the onset of flow of 10 μM melittin at $t = 0$ across cells expressing periplasmic GFP. See Figure 2.1 for composite timeline and Table 2.2 for means and standard deviations. **A** and **H** are from one-color, 12 sec/cycle experiments. **B** and **C** are from two-color, 2 sec/cycle experiments. **D**, **E**, **F**, and **G** are from one-color, 0.5 sec/cycle experiments. **A:** Onset of cell shrinkage and outer membrane permeabilization (OMP) to GFP. **B:** Lag time between OMP to GFP and onset of GFP bubble formation. **C:** Lag time between GFP bubble onset and cytoplasmic membrane permeabilization (CMP) to Sytox Orange. **D:** Lag time between GFP bubble onset and CMP to GFP. **E:** Lag time between OMP and re-sealing of OM to GFP. **F:** Lag time between CMP to GFP and re-sealing of OM to GFP. **G:** Lag time between CMP and CM re-sealing to GFP. **H:** Lag time between initial OMP event and re-permeabilization of both OM and CM to GFP, allowing complete escape of GFP to cell surround.

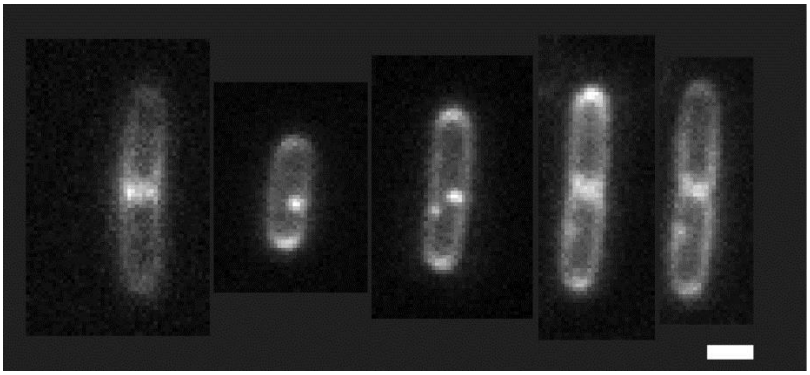

Appendix 2B. Snapshots of representative cells exposed to melittin and the membrane staining dye FM4-64. Bright punctal features always face inward, indicating invagination of the cytoplasmic membrane rather than outward facing blebs in the outer membrane. Scale bar is 1 μm.

A. Melittin attack on *E. coli* expressing cytoplasmic GFP

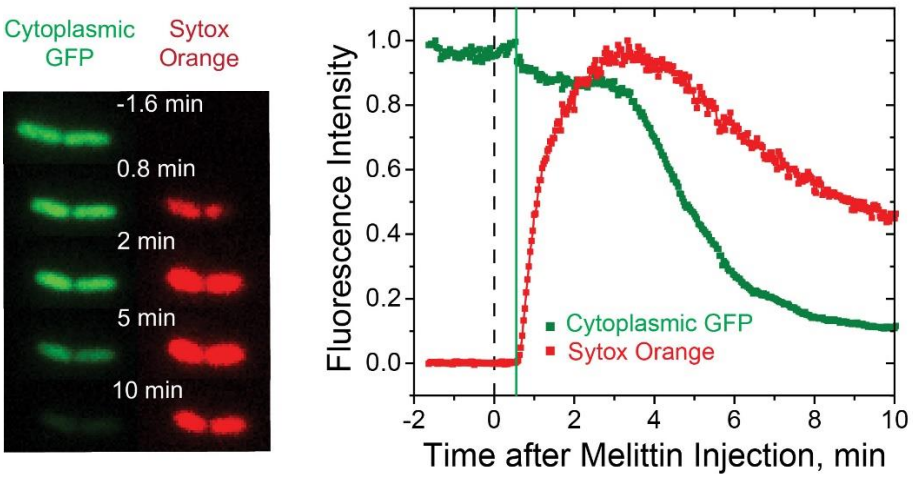

B. LL-37 attack on *E. coli* expressing cytoplasmic GFP

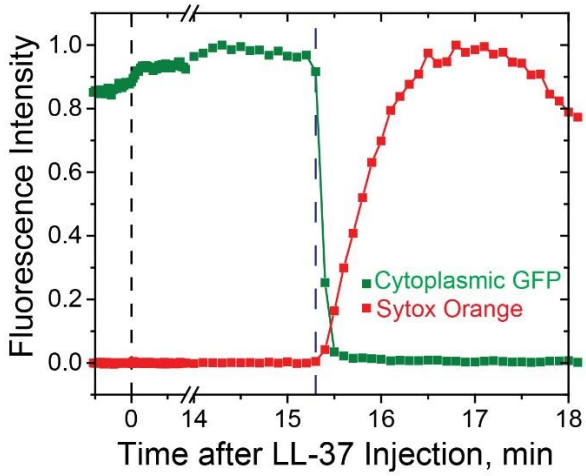

See next page for the figure legend

Appendix 2C. Comparison of rate of loss of cytoplasmic GFP to the cell surround and influx of Sytox Orange into the cytoplasm for attack by melittin vs LL-37. *E. coli* strain is JCW1, which is MG1655 modified to include a plasmid expressing GFPmut2 in the cytoplasm (not exported to the periplasm). **(A)** *Left:* Fluorescence snapshots of a single cell following addition of 10 μM melittin (2X MIC) and 5 nM Sytox Orange. Movie at 2 sec/cycle. *Right:* Time dependence of total fluorescence intensity from GFP and Sytox Orange**.** GFP intensity only decreases slightly when CM is permeabilized to Sytox Orange. Sytox Orange intensity keeps increasing when GFP intensity plateaus. When membranes are re-permeabilized, GFP leaks to cell surround over ~4 min. **(B)** Time dependence of single-cell total fluorescence intensity from GFP and Sytox Orange following addition of 4 μM LL-37 (1X MIC) and 5 nM Sytox Orange. Movie at 6 sec/cycle. Cytoplasmic GFP leaks out completely within ~12 sec.

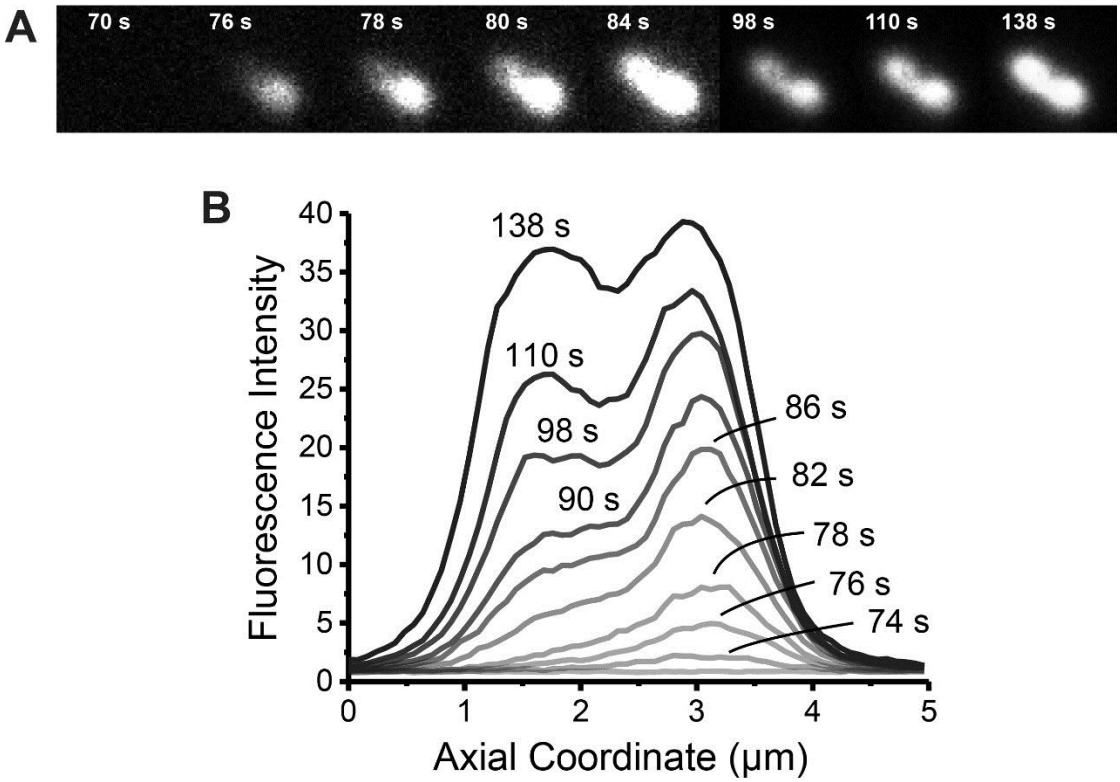

Appendix 2D. For non-septating cells, melittin preferentially attacks endcap of cytoplasmic membrane. **(A)** Sytox Orange fluorescence snapshots of a single *E. coli* cell expressing periplasmic GFP, following addition of 10 μM melittin (2X MIC) and 5 nM Sytox Orange at t = 0 s. Movie at 2 sec/cycle. Brightness enhanced 5-fold for times < 98s for clarity. Sytox Orange lights up initially at one endcap, and then gradually spreads to the entire nucleoid. **(B)** Axial intensity profile of Sytox Orange fluorescence at different times.

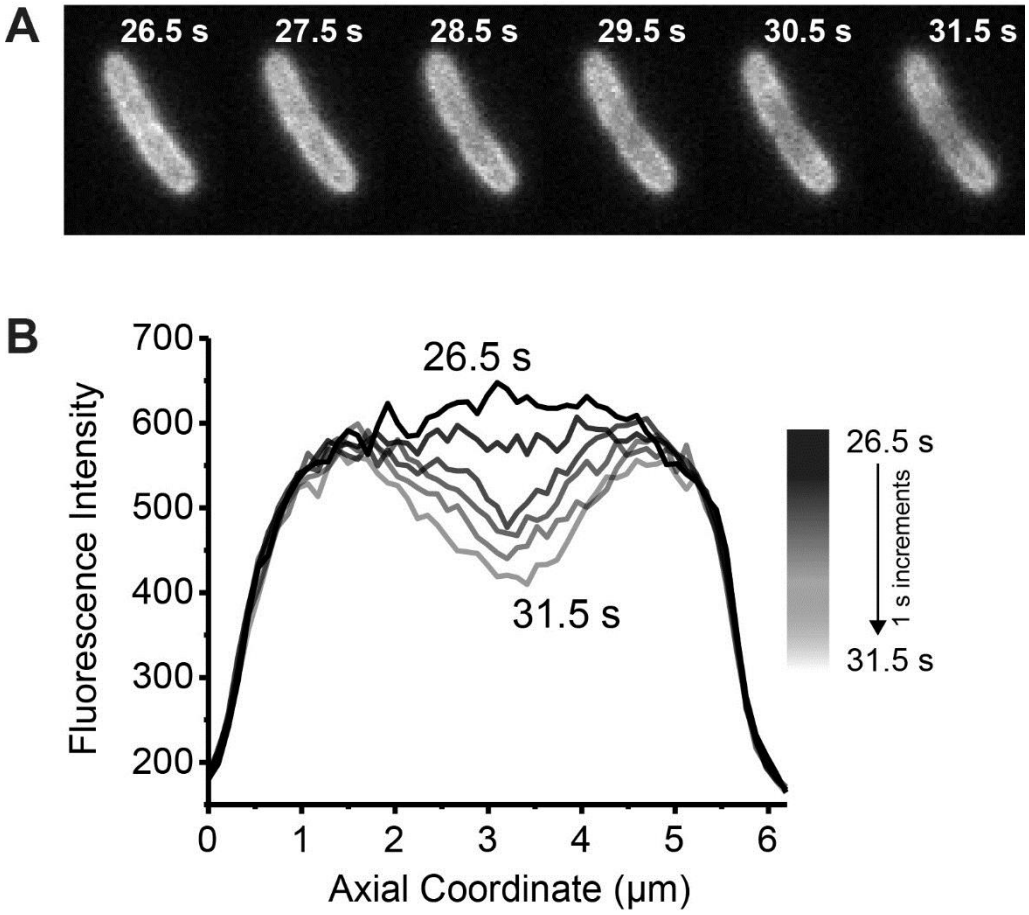

Appendix 2E. Melittin attacks the outer membrane of septating cells at the septal region. **(A)** Green fluorescence snapshots of a single *E. coli* cell expressing periplasmic GFP in aerobic growth conditions, following addition of 10 μM Melittin (2X MIC) and 5 nM Sytox Green at t = 0. Movie acquired at 0.5 sec/cycle. Periplasmic GFP is depleted first from the septal region, before the entry of Sytox Green to the cytoplasm. **(B)** Axial intensity profile of GFP fluorescence at different times, showing the growing hole in the distribution of GFP.

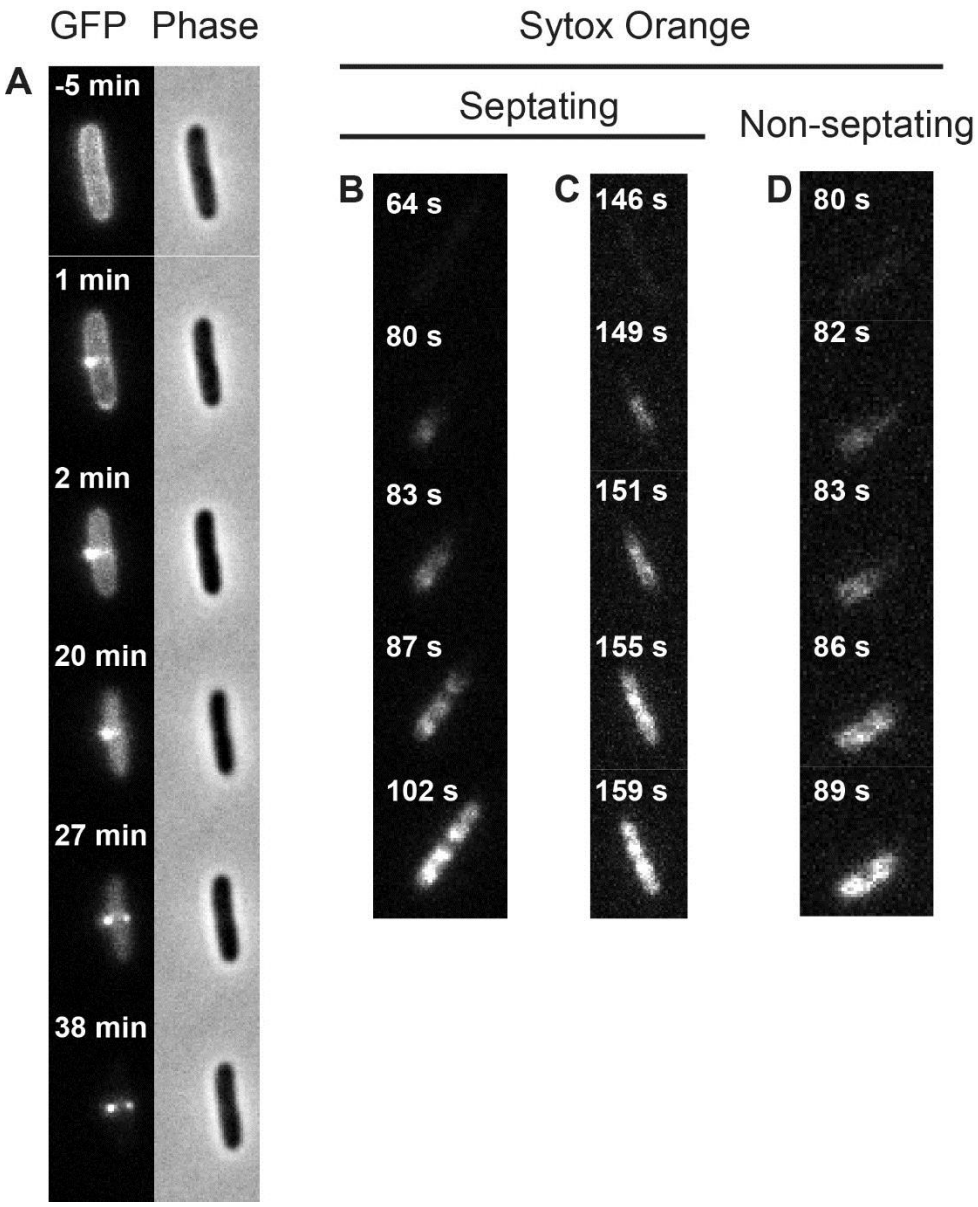

See next page for the figure legend

Appendix 2F. *E. coli* cells attacked by the cecropin A/melittin hybrid peptide CM15. **(A)** Fluorescence and phase contrast snapshots of a single *E. coli* cell expressing periplasmic GFP following addition of 10 μM CM15 (2X MIC). Movie acquisition at 12 sec/cycle. Similar to melittin, CM15 induces a pair of periplasmic GFP bubbles at the septal region. Note the absence of blebs in the phase contrast images. GFP bubbles persist even after outer membrane is permeabilized to GFP. **(B – D)** Sytox Green imaging for three cells showing different modes of attack of CM15 on the cytoplasmic membrane. WT MG1655 *E. coli* cells imaged after addition of 10 μM CM15 (2X MIC) and 5 nM Sytox Green at $t = 0$. Movie acquisition at 0.5 sec/cycle. For septating cells, CM15 sometimes attacks one endcap (**B**), and sometimes attacks the septal region (**C**). For non-septating cells, CM15 always attacks one endcap (**D**).

REFERENCES

1. Dempsey, C. E., The actions of melittin on membranes. *Biochim Biophys Acta* **1990,** *1031* (2), 143-61.

2. Terwilliger, T. C.; Weissman, L.; Eisenberg, D., The structure of melittin in the form I crystals and its implication for melittin's lytic and surface activities. *Biophys J* **1982,** *37* (1), 353-61.

3. Rex, S.; Schwarz, G., Quantitative studies on the melittin-induced leakage mechanism of lipid vesicles. *Biochemistry* **1998,** *37* (8), 2336-45.

4. Ladokhin, A. S.; White, S. H., 'Detergent-like' permeabilization of anionic lipid vesicles by melittin. *Biochim Biophys Acta* **2001,** *1514* (2), 253-60.

5. Wiedman, G.; Herman, K.; Searson, P.; Wimley, W. C.; Hristova, K., The electrical response of bilayers to the bee venom toxin melittin: evidence for transient bilayer permeabilization. *Biochim Biophys Acta* **2013,** *1828* (5), 1357-64.

6. Krauson, A. J.; He, J.; Wimley, W. C., Determining the mechanism of membrane permeabilizing peptides: identification of potent, equilibrium pore-formers. *Biochim Biophys Acta* **2012,** *1818* (7), 1625-32.

7. Lee, M. T.; Sun, T. L.; Hung, W. C.; Huang, H. W., Process of inducing pores in membranes by melittin. *Proc Natl Acad Sci U S A* **2013,** *110* (35), 14243-8.

8. Schwarz, G.; Robert, C. H., Pore formation kinetics in membranes, determined from the release of marker molecules out of liposomes or cells. *Biophys J* **1990,** *58* (3), 577-83.

9. Gregory, S. M.; Pokorny, A.; Almeida, P. F., Magainin 2 revisited: a test of the quantitative model for the all-or-none permeabilization of phospholipid vesicles. *Biophys J* **2009,** *96* (1), 116-31.

10. Yang, L.; Harroun, T. A.; Weiss, T. M.; Ding, L.; Huang, H. W., Barrel-stave model or toroidal model? A case study on melittin pores. *Biophys J* **2001,** *81* (3), 1475-85.

11. Faust, J. E.; Yang, P. Y.; Huang, H. W., Action of Antimicrobial Peptides on Bacterial and Lipid Membranes: A Direct Comparison. *Biophys J* **2017,** *112* (8), 1663-1672.

12. Wimley, W. C.; Hristova, K., Antimicrobial peptides: successes, challenges and unanswered questions. *J Membr Biol* **2011,** *239* (1-2), 27-34.

13. Choi, H.; Yang, Z.; Weisshaar, J. C., Oxidative stress induced in *E. coli* by the human antimicrobial peptide LL-37. *PLoS Pathog* **2017,** *13* (6), e1006481.

14. Barns, K. J.; Weisshaar, J. C., Single-cell, time-resolved study of the effects of the antimicrobial peptide alamethicin on Bacillus subtilis. *Biochim Biophys Acta* **2016,** *1858* (4), 725-32.

15. Choi, H.; Rangarajan, N.; Weisshaar, J. C., Lights, Camera, Action! Antimicrobial Peptide Mechanisms Imaged in Space and Time. *Trends Microbiol* **2016,** *24* (2), 111-22.

16. Choi, H.; Chakraborty, S.; Liu, R.; Gellman, S. H.; Weisshaar, J. C., Single-Cell, Time-Resolved Antimicrobial Effects of a Highly Cationic, Random Nylon-3 Copolymer on Live *Escherichia coli*. *ACS Chem Biol* **2016,** *11* (1), 113-20.

17. Choi, H.; Yang, Z.; Weisshaar, J. C., Single-cell, real-time detection of oxidative stress induced in *Escherichia coli* by the antimicrobial peptide CM15. *Proc Natl Acad Sci U S A* **2015,** *112* (3), E303-10.

18. Rangarajan, N.; Bakshi, S.; Weisshaar, J. C., Localized permeabilization of *E. coli* membranes by the antimicrobial peptide Cecropin A. *Biochemistry* **2013,** *52* (38), 6584-94.

19. Barns, K. J.; Weisshaar, J. C., Real-time attack of LL-37 on single *Bacillus subtilis* cells. *Biochim Biophys Acta* **2013,** *1828* (6), 1511-20.

20. Sochacki, K. A.; Barns, K. J.; Bucki, R.; Weisshaar, J. C., Real-time attack on single *Escherichia coli* cells by the human antimicrobial peptide LL-37. *Proc Natl Acad Sci U S A* **2011,** *108* (16), E77-81.

21. Gumbart, J. C.; Beeby, M.; Jensen, G. J.; Roux, B., *Escherichia coli* peptidoglycan structure and mechanics as predicted by atomic-scale simulations. *PLoS Comput Biol* **2014,** *10* (2), e1003475.

22. Clark, K. S.; Svetlovics, J.; McKeown, A. N.; Huskins, L.; Almeida, P. F., What determines the activity of antimicrobial and cytolytic peptides in model membranes. *Biochemistry* **2011,** *50* (37), 7919-32.

23. Sochacki, K. A.; Shkel, I. A.; Record, M. T.; Weisshaar, J. C., Protein diffusion in the periplasm of *E. coli* under osmotic stress. *Biophys J* **2011,** *100* (1), 22-31.

24. Konopka, M. C.; Sochacki, K. A.; Bratton, B. P.; Shkel, I. A.; Record, M. T.; Weisshaar, J. C., Cytoplasmic protein mobility in osmotically stressed *Escherichia coli*. *J Bacteriol* **2009,** *191* (1), 231-7.

25. Choi, H.; Chakraborty, S.; Liu, R.; Gellman, S. H.; Weisshaar, J. C., Medium effects on minimum inhibitory concentrations of nylon-3 polymers against *E. coli*. *PLoS One* **2014,** *9* (8), e104500.

26. Bakshi, S.; Siryaporn, A.; Goulian, M.; Weisshaar, J. C., Superresolution imaging of ribosomes and RNA polymerase in live *Escherichia coli* cells. *Mol Microbiol* **2012,** *85* (1), 21-38.

27. Konopka, M. C.; Shkel, I. A.; Cayley, S.; Record, M. T.; Weisshaar, J. C., Crowding and confinement effects on protein diffusion in vivo. *J Bacteriol* **2006,** *188* (17), 6115-23.

28. Konopka, M. C.; Sochacki, K. A.; Bratton, B. P.; Shkel, I. A.; Record, M. T.; Weisshaar, J. C., Cytoplasmic Protein Mobility in Osmotically Stressed *Escherichia coli*. *J Bacteriol* **2008**.

29. DeGrado, W. F.; Musso, G. F.; Lieber, M.; Kaiser, E. T.; Kezdy, F. J., Kinetics and mechanism of hemolysis induced by melittin and by a synthetic melittin analogue. *Biophys J* **1982,** *37* (1), 329-38.

30. Wiedman, G.; Fuselier, T.; He, J.; Searson, P. C.; Hristova, K.; Wimley, W. C., Highly efficient macromolecule-sized poration of lipid bilayers by a synthetically evolved peptide. *J Am Chem Soc* **2014,** *136* (12), 4724-31.

31. Sun, Y.; Sun, T. L.; Huang, H. W., Mode of Action of Antimicrobial Peptides on *E. coli* Spheroplasts. *Biophys J* **2016,** *111* (1), 132-9.

32. Starr, C. G.; He, J.; Wimley, W. C., Host Cell Interactions Are a Significant Barrier to the Clinical Utility of Peptide Antibiotics. *ACS Chem Biol* **2016,** *11* (12), 3391-3399.

33. Roversi, D.; Luca, V.; Aureli, S.; Park, Y.; Mangoni, M. L.; Stella, L., How many antimicrobial peptide molecules kill a bacterium? The case of PMAP-23. *ACS Chem Biol* **2014,** *9* (9), 2003-7.

34. Cayley, D. S.; Guttman, H. J.; Record, M. T., Jr., Biophysical characterization of changes in amounts and activity of *Escherichia coli* cell and compartment water and turgor pressure in response to osmotic stress. *Biophys J* **2000,** *78* (4), 1748-64.

35. Chileveru, H. R.; Lim, S. A.; Chairatana, P.; Wommack, A. J.; Chiang, I. L.; Nolan, E. M., Visualizing attack of *Escherichia coli* by the antimicrobial peptide human defensin 5. *Biochemistry* **2015,** *54* (9), 1767-77.

Chapter 3

HaloTag Assay Suggests Common Mechanism of *E. coli* Membrane Permeabilization Induced by Cationic Peptides

Adapted from the publication listed below with permissions:

Yang, Z., and Weisshaar, J. C. (**2018**) HaloTag Assay Suggests Common Mechanism of *E. coli* Membrane Permeabilization Induced by Cationic Peptides, *ACS Chemical Biology*.

* ZY and JCW contributed to design of the project. ZY performed the experiments. ZY and JCW analyzed the data and wrote the manuscript. Supplemental movies are available online.

ABSTRACT

Permeabilization of the Gram negative bacterial outer membrane (OM) by antimicrobial peptides (AMPs) is the initial step enabling access of the AMP to the cytoplasmic membrane. We present a new single-cell, time-resolved fluorescence microscopy assay that reports on the permeabilization of the *E. coli* OM to small molecules, with time resolution of 3 sec or better. When the profluorophore JF_{646} (702 Da) crosses the outer membrane (OM) and gains access to the periplasm, it binds to localized HaloTag protein (34 kDa) and fluoresces in a characteristic hollow spatial pattern. Previous work used the much larger periplasmic GFP (27 kDa) probe, which reports on OM permeabilization to globular proteins. We test the assay on three cationic agents: the Gellman random β–peptide copolymer MM_{63}:CHx_{37}, the human AMP LL-37, and the synthetic hybrid AMP CM15. These results combined with previous work suggest a unifying sequence of OM and cytoplasmic membrane (CM) events that may prove commonplace in the attack of cationic peptides on Gram negative bacteria. The peptide initially induces gradual OM permeabilization to small molecules, likely including the peptide itself. After a lag time, abrupt permeabilization of the OM, abrupt re-sealing of the OM, and abrupt permeabilization of the CM (all to globular proteins) occur in rapid sequence. We propose a mechanism based on membrane curvature stress induced by time-dependent differential binding of peptide to the outer leaflet of the OM and CM. The results provide fresh insight into the critical OM permeabilization step leading to a variety of damaging downstream events.

Introduction

Antimicrobial peptides (AMPs), also called host-defense peptides, play a dual role in the innate immune system of many species, including humans, acting as both antimicrobial agents and signaling molecules.[1-2] In this era of multi-drug resistant bacteria, AMPs may serve as useful lead compounds in the search for novel antibacterial agents. One widespread mechanism of action of natural AMPs is the permeabilization of bacterial membranes of both Gram positive and Gram negative species. Perhaps as a result, bacterial resistance to AMPs develops only slowly.

By now it is clear that the damage mechanisms induced by AMPs go well beyond membrane permeabilization and destruction of the trans-membrane potential that drives ATP production.[3-4] A wide variety of bulk culture and single-cell diagnostic assays have revealed numerous physical and biochemical effects of AMPs on cultured bacteria.[5-6] Our lab has been developing single-cell, time resolved, fluorescence-based assays that monitor a variety of AMP-induced "symptoms".[7-15] We have focused primarily on the Gram negative species *E. coli* under attack by the polycationic AMPs LL-37,[7, 14] Cecropin A,[8] CM15,[11] and Melittin,[15] as well as by the synthetic cationic random β-peptide copolymer MM_{63}:CHx_{37} (**Table 3.1**).[13] Thus far the methods enable direct determination of the timing of events such as outer membrane permeabilization (OMP) to GFP, cytoplasmic membrane permeabilization (CMP) to GFP and a Sytox dye, cell shrinkage, the halting of growth, and the onset of oxidative stress. Each antimicrobial agent exhibits a unique set of events.

Our simplest assay uses a strain of *E. coli* MG1655 that expresses GFP bound to a TorA signal sequence, causing export of GFP from the cytoplasm to the periplasm via the Tat system.[16] Periplasmic GFP creates a hollow, shell-like image in the 2D fluorescence microscope.

This assay alone yields a surprising variety of behaviors for different cationic peptides. After initiation of the flow of LL-37[7, 14] or Cecropin A[8] across plated cells at $t = 0$, we observe a time lag followed by loss of the periplasmic GFP signal to the cell surround. The behavior is illustrated for a representative septating cell during attack by Cecropin A in **Figure 3.1A**. Evidently the AMP has induced OM permeabilization to small, globular proteins in localized fashion at the septal region. In sharp contrast, for the short, synthetic AMP CM15 and for the longer synthetic copolymer MM_{63}:CHx_{37}, the initial periplasmic GFP image abruptly evolves to a filled, cytoplasmic image. This alternative behavior is illustrated for a non-septating cell attacked by the copolymer in **Figure 3.1B**. Evidently the copolymer has first induced CM permeabilization to periplasmic GFP, which moves inward to fill the much larger cytoplasmic volume. Meanwhile, the total GFP fluorescence intensity remains essentially constant. GFP is lost to the surround only much later. Most recently, we found that Melittin induces behavior intermediate between that of **Figure 3.1A** and **3.1B**.[15] After a time lag, roughly half of the periplasmic GFP intensity is lost to the surround, and the remainder of the intensity soon exhibits a cytoplasmic spatial distribution. Complete loss of GFP occurs only much later. Evidently the OM has become transiently permeable to GFP and then re-sealed. Meanwhile the CM has become permeable to GFP. Such re-sealing behavior is reminiscent of the effects of AMPs on purified lipid vesicles and GUVs.[17-24]

GFP is a small, globular protein of mass 27 kDa, much larger than the typical antimicrobial agent of mass ~1–5 kDa. Before periplasmic GFP has moved inward to fill the cytoplasm, the antimicrobial agent must surely have translocated across the OM to gain access to the periplasmic space and to the CM itself. This passage is the key initial step in AMP activity against Gram negative bacteria. An important mechanistic question is: how does the cationic

agent cross the OM? It is possible that linear cationic peptides might thread their way through open porin channels in the OM, as seemingly occurs for colicin.[25] The peptide might also transiently insert in the OM bilayer and subsequently de-insert into the periplasmic space, without having permeabilized the OM to other small molecules, much less to GFP. Finally, the peptide might first induce OM permeabilization to smaller species, including itself; these permeabilization sites may subsequently evolve to enable passage of small globular proteins such as GFP.

In order to dissect these possibilities, it is highly desirable to develop a single-cell assay that detects the onset of OM permeabilization to small molecules with good time resolution. Previously developed bulk assays used small profluorophores to detect permeabilization of the OM, but without spatiotemporal resolution.[26-28] Here we describe a single-cell, time-resolved, fluorescence microscopy assay based on binding of a red-emitting profluorophore called JF_{646} ligand[29] (mass 702 Da, **Figure 3.2B**) to HaloTag protein[30] (34 kDa) that has been exported to the periplasm. When an antimicrobial agent induces OM permeabilization to the JF_{646} ligand, the ligand gains access to the periplasm, binds covalently to HaloTag protein, and fluoresces red with a periplasmic spatial distribution. The assay is sensitive enough to detect the onset of OM permeabilization to JF_{646} ligand with time resolution of 3 sec or better. The new results for copolymer MM_{63}:CHx_{37} and for LL-37 strongly suggest that a common mechanism may apply to all five peptides in **Table 3.1**. Initial, gradual OM permeabilization to small species is followed by a time lag before abrupt OM permeabilization to globular proteins. Abrupt re-sealing of the OM and permeabilization of the CM to globular proteins follow shortly afterward. This may prove to be a fairly general sequence of events across a variety of cationic peptides, with timing details dependent on the specific peptide and its concentration. We present a mechanistic picture

of membrane permeabilization and re-sealing in terms of time-dependent curvature stress caused by asymmetric binding of the peptide to the two leaflets of the membrane. This mechanism is borrowed from a large body of work on vesicles composed of pure lipids.[17-22]

Future extensions might combine the new HaloTag-based assay with addition of external Sytox Green or Sytox Orange, which bind to chromosomal DNA to signal CM permeabilization to small molecules. Such a combined single-cell assay could reveal the timing of OM and CM permeabilization events to both small species and globular proteins, all in one experiment. These methods may also find application in mechanistic studies of the effects of small-molecule antibiotics.

METHODS

The strains and plasmids used in this study are summarized in **Appendix 3A**. Details of strain construction and induction conditions are provided in **Appendix**. Bulk cultures were grown in EZRDM[31] from glycerol frozen stock to stationary phase overnight at 30°C. Subcultures were grown to exponential phase (OD = 0.2–0.6 at 600 nm) before sampling for the microscopy experiments at 30°C. The antimicrobial agents are described in **Table 3.1**; additional details are found in SI. The aerobic MIC values for the various antimicrobial agents were determined using the broth microdilution method as previously described.[7] Imaging of individual cells was carried out at 30°C in a simple microfluidics chamber as previously described.[11] Fresh, aerated medium flows over the cells continuously. The cells were imaged for ~5 min before switching to fresh medium containing the compounds under study (antimicrobial agent, JF_{646} ligand). Details of the microscopy procedure and setup are in SI. The concentration of each peptide was chosen to be sufficiently high to cause significant antimicrobial action on a 30-min timescale, but low enough to enable the methods to resolve sequential events in time.

RESULTS AND DISCUSSION

The new assay detects the onset of OM permeabilization to small molecules using the HaloTag concept (**Figure 3.2**).[30] This requires two components, an *E. coli* strain that exports the HaloTag protein to the periplasmic space and an impermeant profluorophore called JF_{646} ligand.[29] The strains used in this work are listed in **Appendix 3A**. Strain zy3720 carries a plasmid pMB2 that expresses HaloTag protein with the DsbA signal peptide appended to the N-terminus (ssDsbA–HaloTag). As a result, HaloTag protein is co-translationally exported to the periplasm, as previously shown.[32] In aqueous solution, the JF_{646} ligand preferentially adopts the closed lactone form, which fluoresces only weakly (**Figure 3.2B**). When JF_{646} ligand binds covalently to the HaloTag protein to form the HaloTag-JF_{646} conjugate, the local environment around JF_{646} changes. The result is a large increase in red JF_{646} fluorescence.[29, 33] A hollow, shell-like spatial distribution signals the passage of JF_{646} ligand across the OM into the periplasm. At the same time, the OM presumably becomes permeable to other small molecules, likely including the antimicrobial agent itself. If the next step is CM permeabilization to globular proteins, the HaloTag-JF_{646} conjugate gains access to the cytoplasm, and the hollow spatial distribution fills in. If the next step is OM permeabilization to globular proteins, the conjugate leaves the cell envelope and the red fluorescence disappears. By measuring fluorescence intensity across the short axis of the cell, we can determine for each camera frame whether a fluorophore distributes predominantly in the periplasm or throughout the entire cell.

Minimum inhibitory concentration (MIC) results for the antimicrobial agents are shown in **Table 3.1**. Details of the microscopy experiments are described in SI. Briefly, exponentially growing cells are plated in a microfluidics chamber. At $t = 0$, the flow of aerated medium is switched to aerated medium plus a fixed concentration of antimicrobial agent and 100 nM

JF_{646} ligand. For one-color imaging experiments using strain zy3720, we alternate fluorescence and phase contrast images, usually at 6 sec intervals (12 sec/cycle). The fluorescence image monitors the JF_{646} ligand binding to HaloTag protein and the phase contrast image monitors cell length. Two-color imaging experiments use strain zy3722 that contains a plasmid expressing both ssDsbA–HaloTag and ssTorA–GFP. Both HaloTag protein and GFP are exported to the periplasm. We sequentially acquire two fluorescence channels and the phase contrast channel, again at 12 sec/cycle. The green channel monitors GFP, the red channel monitors JF_{646} fluorescence, and the phase contrast channel monitors cell length. For each case, typically at least 60 cells in total were analyzed from three repeat experiments.

Preliminary tests

First we tested two strains for their ability to export HaloTag protein to the periplasm, zy3719 and zy3720 (**Appendix 3B**). Strain zy3719 carries plasmid pMB1, expressing the HaloTag domain fused to the signal sequence of maltose-binding periplasmic protein (ssMalE-HaloTag). Strain zy3720 carries plasmid pMB2, expressing the HaloTag domain fused to the signal sequence of the periplasmic protein DsbA (ssDsbA–HaloTag). To determine where the HaloTag protein localizes inside *E. coli* cells, we added the permeable, red fluorescent tetramethyl-rhodamine ligand (TMR ligand).[30] On excitation at 561 nm, TMR ligand emits at 580 nm. When supplied exogenously, TMR ligand permeates both membranes of living *E. coli* cells and covalently binds to HaloTag protein specifically. After rinsing with fresh medium, unbound TMR ligands are removed from the cells. The pattern of the residual fluorescence reports on the spatial distribution of the HaloTag protein.

Wild-type (WT) MG1655 cells do not express HaloTag protein and exhibited no significant TMR fluorescence after TMR ligand incubation and rinsing (**Appendix 3B.**). There is

little or no permanent binding of TMR ligand to the cell envelope or to periplasmic or cytoplasmic components. Attempts at exporting HaloTag protein to the periplasm using ssMalE (strain zy3719) failed (**Appendix 3B.A**). TMR fluorescence fills the entire cell, indicating that functional HaloTag protein remains primarily in the cytoplasm. In contrast, for strain zy3720 using the ssDsbA signal, TMR fluorescence exists predominately in the periplasm, indicating that HaloTag protein is exported efficiently to the periplasm (**Appendix 3B.A**). Similarly, two-color imaging demonstrated that strain zy3722 efficiently exports both HaloTag protein and GFP to the periplasm (**Appendix 3B.A**).

Next we tested the membrane permeability and toxicity of JF_{646} ligand towards *E. coli.* At $t = 0$, we flowed 100 nM JF_{646} ligand alone across *E. coli* zy3720 cells expressing periplasmic HaloTag protein. Fluorescence images and phase contrast images were interleaved, to monitor JF_{646} fluorescence and bacterial growth. During 1 hr of continuous flow, no obvious fluorescence was observed inside the cells (**Appendix 3B.B**, Movie S1). Although some background fluorescence outside the cells appeared in the first few minutes, JF_{646} ligand at 100 nM does not permeate the OM of *E. coli*. A detailed description is included in SI. Meanwhile, JF_{646} ligand does not harm the growth of *E. coli*, as cells continue to grow and divide. The doubling time for *E. coli* zy3720 cells in the presence of 100 nM JF_{646} ligand is 52 ± 3 min, determined from cell length vs time. This is comparable to the 50 ± 3 min doubling time of WT *E. coli* cells plated in the microfluidic chamber when only EZ rich defined medium (EZRDM) is supplied.

Finally, we tested for JF_{646} fluorescence in WT cells (lacking HaloTag protein) after permeabilization by copolymer MM_{63}:CHx_{37} at 1.2X MIC (**Appendix 3B.C**). We observe only a weak burst of red intracellular fluorescence that begins after OM permeabilization (see below)

and quickly dies away. This burst is at least 30-fold weaker than the JF_{646} fluorescence induced in zy3720 cells by the copolymer, as shown below.

Membrane permeabilization and re-sealing induced by copolymer MM_{63}:CHx_{37}

First we used the one-color assay to observe membrane permeabilization events induced by the copolymer MM_{63}:CHx_{37} in *E. coli* cells. At t = 0, we flowed 30 μg/mL of MM_{63}:CHx_{37} (1.2X MIC) plus 100 nM JF_{646} ligand across plated *E. coli* zy3720 cells that export HaloTag protein to the periplasm. In these one-color experiments, we monitored JF_{646} fluorescence and phase contrast every 12 s. Consistent with our previous study,[13] nearly all cells began to shrink in length beginning within 24 sec of MM_{63}:CHx_{37} addition. Later some cells partially recovered cell length, as before. For the representative cell in **Figure 3.3A** and Movie S2, the cell length decrease started at t_1 = 0.2 min and continued until 1.4 min, when partial reversal occurred. Beginning at t_2 = 0.4 min, red JF_{646} fluorescence increased abruptly and continued to rise until t = 1.8 min, when it reached a plateau (**Figure 3.3C**). The plateau may indicate that all the HaloTag protein has become bound by JF_{646} ligands. As shown from transverse intensity profiles (**Figure 3.3B**), the JF_{646} fluorescence at first accumulated in the periplasm, but began to fill the cytoplasm at t_3 = 1.6–1.8 min.

Copolymer MM_{63}:CHx_{37} caused OM permeabilization to JF_{646} ligand, allowing it to enter the periplasm and bind to the HaloTag protein. Initially much or all of the HaloTag-JF_{646} conjugate remained in the periplasm. Later the CM was permeabilized to the HaloTag-JF_{646} conjugate, which began to fill the cytoplasm. Meanwhile, the OM remained essentially impermeable to the conjugate. We previously interpreted the shrinkage event as primarily an osmotic effect caused by entry of the highly cationic copolymer and its many counterions into the periplasm.[13] The partial recovery of length may be due to import of K^+ ions into the

cytoplasm. Under the assumption that the OM was permeabilized to the copolymer (mean molar mass ~7 kDa) at the same time as the JF_{646} ligand (702 Da), the earlier explanation is corroborated. Notice that the onset of shrinkage matches the onset of HaloTag-JF_{646} conjugate fluorescence within 1 camera cycle = 0.2 min = 12 sec. The duration of the shrinkage event and the risetime of the fluorescence seem to match as well.

It is important to exclude the possibility that the JF_{646} fluorescence increase is produced by interaction of JF_{646} ligand with some intracellular species other than HaloTag protein. In **Appendix 3B.C** (and Movie S3), we show a control experiment flowing 30 μg/mL MM_{63}:CHx_{37} plus 100 nM JF_{646} ligand across wild type *E. coli* cells containing no HaloTag protein. A weak, transient, intracellular, cytoplasmic signal appears only after the shrinkage event. The peak fluorescence intensity in the control experiments (**Appendix 3B.C**) is at least 30-fold smaller than the plateau value attained when HaloTag protein is present (**Figure 3.3C**). Evidently the bright periplasmic fluorescence observed in zy3720 cells is almost entirely due to the binding of JF_{646} ligand to the HaloTag protein following OM permeabilization.

We measure the mean values across cells of the timing events t_1 (onset of cell shrinkage), $(t_2 - t_1)$ (the additional lag time to the onset of HaloTag-JF_{646} conjugate fluorescence in the periplasm), and $(t_3 - t_2)$ (the lag time between the onset of periplasmic fluorescence and entry of the conjugate into the cytoplasm). The corresponding detailed distributions are shown in **Appendix 3C**. Across 70 cells, $\langle(t_2 - t_1)\rangle = 0.2 \pm 0.0$ min and $\langle(t_3 - t_2)\rangle = 1.0 \pm 0.7$ min (± 1SD). Even at 1.2X MIC, the Gellman copolymer MM_{63}:CHx_{37} permeabilizes the OM and CM in rapid succession. The new assay readily discerns both the onset of OM permeabilization to small molecules and the onset of CM permeabilization to globular proteins using a single fluorophore.

To gain additional information, we also applied the two-color assay to the attack of copolymer MM_{63}:CHx_{37} on *E. coli* cells. At $t = 0$, we flowed 30 μg/mL MM_{63}:CHx_{37} (1.2X MIC) plus 100 nM JF_{646} ligand across *E. coli* zy3722 cells that export both HaloTag protein and GFP to the periplasm. In these experiments, we monitored green GFP fluorescence, red JF_{646} fluorescence, and phase contrast with a cycle time of 12 s. As in the one-color experiment, the JF_{646} signal begins to rise shortly after the onset of cell shrinkage, initially forming a periplasmic image. For the particular cell in **Figure 3.4A** and Movie S4, this occurs at $t_2 = 0.6$ min, and the signal continues to rise gradually up until $t_3 = 5.2$ min. The JF_{646} image remains periplasmic during this interval. Meanwhile, the periplasmic GFP image maintains its intensity (except for minor photobleaching) over the same period. This demonstrates clearly that the OM has initially become permeabilized to small molecules such as JF_{646} ligand, but not to small globular proteins such as periplasmic GFP.

At $t_3 = 5.2$ min, both GFP and JF_{646} images abruptly change from periplasmic to cytoplasmic. Interestingly, at the same moment the GFP intensity decreases by about 10% while the HaloTag–JF_{646} conjugate intensity increases by about 20%. Our interpretation is that the copolymer is inducing transient permeabilization of the OM to GFP, after which the OM re-seals to globular proteins of GFP size or larger. The transient opening lasts only about 3 frames = 36 sec. The same transient OM permeabilization event presumably also releases some of the (slightly larger) periplasmic HaloTag protein. However, during the transient event, the JF_{646} ligand can cross the OM more rapidly than before, resulting in a net abrupt increase in fluorescence from the HaloTag–JF_{646} conjugate. Essentially simultaneously with the OM re-sealing event, the CM becomes permeable to both GFP and HaloTag–JF_{646} conjugate and

both images fill in. Meanwhile, the OM remains permeable to JF_{646} ligand, as evidenced by the slow continuing rise of conjugate fluorescence at $t > 5.2$ min.

Membrane permeabilization and re-sealing induced by LL-37

We also applied the one-color assay to the human AMP LL-37. In previous work imaging periplasmic GFP and Sytox Green in the same fluorescence channel, we had observed loss of roughly 90% of periplasmic GFP to the surround (signaling OM permeabilization to GFP) and the subsequent rise in Sytox Green fluorescence (CM permeabilization to Sytox Green).[7, 14] The very strong Sytox Green signal would have obscured any residual GFP that was trapped inside the cell by a membrane re-sealing event.

The one-color HaloTag assay reveals that an OM re-sealing event in fact occurs during the attack of LL-37. At $t = 0$ we initiated flow of 4 μM LL-37 (1X MIC) plus 100 nM JF_{646} across plated zy3720 cells. The typical behavior is shown in **Figure 3.5** and Movie S5. Within 2 min, an intracellular, periplasmic signal from HaloTag–JF_{646} conjugate begins to rise gradually and cell growth begins to slow down. At $t = 14.5$ min, some 75% of the fluorescence is lost abruptly to the surround. The remaining 25% exhibits the cytoplasmic (filled cell) spatial pattern. Once again, our interpretation is that the OM is transiently permeabilized to the conjugate. At essentially the same time as the OM re-seals to globular proteins, the CM is permeabilized to the conjugate. A brief test of the two-color assay (green periplasmic GFP and red HaloTag–JF_{646} conjugate) on LL-37 confirmed that periplasmic GFP and HaloTag–JF_{646} conjugate move similarly in space and time (**Appendix 3D**). Most of the GFP and the conjugate intensity is lost at the same time, and both images change abruptly from the periplasmic to the cytoplasmic spatial distribution.

Rapid CM permeabilization induced by CM15

Finally, we applied the one-color assay to the short, synthetic antimicrobial peptide CM15, which was previously shown to induce very rapid migration of periplasmic GFP into the cytoplasm.[11] Flow of 10 μM CM15 (2X MIC) plus 100 nM JF_{646} ligand across zy3720 cells began at $t = 0$. In an attempt to estimate the kinetic response time of the new assay, the time resolution was increased to 3 sec/cycle. For the representative cell in **Figure 3.6**, shrinkage of cell length by some 20% began abruptly at $t_1 = 39$ sec and was essentially complete in only 4 frames = 12 sec. The onset of JF_{646} fluorescence was essentially simultaneous with t_1. We infer very rapid passage of CM15 across the OM and into the periplasm. Evidently the assay is sufficiently sensitive to detect the onset of OM permeabilization to small molecules to within 3 sec or better. The shift of JF_{646} fluorescence from a periplasmic distribution to a cytoplasmic distribution occurs within one camera cycle, at $t_2 = 0.70–0.75$ min = 42–45 sec. This event is also detected with time resolution of 3 sec or better. The rising signal reached 2/3 of its plateau value in 10 frames = 30 sec. This is a convolution of the timescale of passage of JF_{646} ligand into the periplasm and the timescale for the bimolecular reaction between JF_{646} ligand and the periplasmic HaloTag protein. Thus we take 30 sec as an upper bound on the kinetic response time of the new assay under the conditions described. The comparable fluorescence risetime for the copolymer experiment in **Figure 3.3C** is much longer, ~60 sec. Accordingly, the cell shrinkage event is slower, itself requiring ~60 sec. We interpret this to mean that the copolymer and JF_{646} ligand gain access to the periplasm less rapidly than do CM15 and JF_{646} ligand.

General mechanistic insights

The new HaloTag–JF_{646} assay reveals that after an initial time delay, both the copolymer MM_{63}:CHx_{37} and the natural AMP LL-37 induce a brief period of OM permeability to globular proteins followed by re-sealing of the OM and abrupt permeabilization of the CM to globular

proteins. A similar sequence of events was recently elucidated for the antimicrobial peptide Melittin using periplasmic GFP as the probe.[15] For MM_{63}:CHx_{37} and for LL-37, the new HaloTag assay also enables direct observation of permeabilization of the OM to the much smaller JF_{646} ligand during the initial lag time leading up to OM permeabilization to globular proteins. It is highly likely that the OM has become permeable to the antimicrobial agent itself during the same initial period. We have not tested the timing of JF_{646} permeability induced by Melittin.

Evidently all three of these cationic peptides attack the *E. coli* cell envelope in a similar sequence of mechanistic steps. During the initial period, the peptide binds to and penetrates the anionic lipopolysaccharide (LPS) layer, eventually permeabilizing the OM to small molecules such as JF_{646} ligand, and presumably to the peptide itself. Our methods do not directly speak to the molecular-level details of the initial permeabilization mechanism, which could involve "detergent-like" disruption of OM structure[34-35] or formation of small toroidal pores.[36-37] It would be interesting to learn whether the initial permeabilization occurs locally or globally; such observations would require faster imaging than we have employed here. As more and more cationic peptide binds to the outer leaflet of the OM, this generates increasing curvature stress. The stress eventually causes abrupt OM permeabilization to globular proteins such as GFP, HaloTag protein, and the HaloTag–JF_{646} conjugate, enabling partial loss to the cell surround. This larger-scale disruption of the OM begins and ends abruptly in comparison with the earlier, gradual, continual leakage of small molecules across the OM. Earlier work showed that the larger disruption is often localized at curved membrane surfaces; see the septating cell attacked by Cecropin A in **Figure 3.1**. These details suggest a slow nucleation event preceding the formation of pores sufficiently large to pass globular proteins. The

larger-scale disruption event then enables much more rapid translocation of the peptide into the periplasm, where it binds to the inner leaflet of the OM. This relieves the curvature stress and enables effective re-sealing of the OM to globular proteins.

During the disruption of the OM to globular proteins, the peptide concentration can build rapidly in the periplasm. The same process of differential curvature stress repeats itself due to peptide binding to the outer leaflet of the CM, which then abruptly becomes permeable to globular proteins. The proteins that did not escape the periplasm during the transient OM permeabilization event thus gain entry to the cytoplasm. The rapid build-up of peptide concentration in the periplasm while the OM is open to passage of globular proteins explains why OM re-sealing and CM permeabilization to such proteins seem coupled in time. In the specific case of Melittin, detailed analysis showed that subsequently the CM also re-sealed to GFP, presumably by the same curvature relief mechanism. Seemingly analogous peptide-induced permeabilization and re-sealing events have been observed in studies of pure lipid vesicles and GUVs. Indeed, we have borrowed the curvature stress mechanism from that body of work.[17-22]

This detailed mechanistic picture of gradual permeabilization of the OM to small molecules followed by abrupt, transient permeabilization of the OM to globular proteins followed by permeabilization of the CM may prove to be fairly general in describing the attack of cationic peptides on *E. coli*, and perhaps on other Gram negative species as well. Previous work shows that the timing of these events depends on the bulk peptide concentration.[7-8] It is easy to imagine that different peptides will carry out these events at different rates. The HaloTag assay described here provides a new way to probe size- and time-dependent membrane permeabilization events in living cells in real time.

ACKNOWLEDGMENTS

We thank B. Mehmet (New England Biolabs) for providing the plasmids pMB1 and pMB2, L. Lavis (Janelia Research Campus) for providing JF_{646} ligand, and H. Choi (Janelia Research Campus) for helpful discussion. The Gellman lab provided the MM_{63}:CHx_{37} copolymer sample.

FUNDING SOURCES

This research was supported by the National Institute of General Medical Sciences of the National Institutes of Health under awards R01GM094510 (to JCW as PI) and R01GM093265 (to JCW and Samuel Gellman as co-PIs). The content is solely the responsibility of the authors and does not necessarily represent the official views of the National Institutes of Health.

SUPPORTING INFORMATION

Details on methods, strains and plasmids used in this work (**Appendix 3A**). Control experiments for the HaloTag-based membrane permeabilization assay (**Appendix 3B**). Histograms of lag times for one-color experiment after MM_{63}:CHx_{37} addition (**Appendix 3C**). An example of two-color experiment after LL-37 addition (**Appendix 3D**). Five movies in various conditions.

Table 3.1 Antimicrobial agents.

Antimicrobial Agent	Sequence	Mass (Da)	Net Charge	MIC (μM) [1]
LL-37	**LLGDFFRKSKEKIGKEFKRI-VQRIKDFLRNLVPRTES**	4493	+6	4
Cecropin A	**KWKLFKKIEKVGQNIRDGII-KAGPAVAVVGQATQIAK-NH_2**	4404	+7	0.9
Melittin	**GIGAVLKVLTTGLPALISWI-KRKRQQ-NH_2**	2846	+6	5
β-peptide copolymer MM_{63}:CHx_{37}	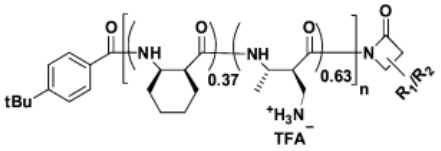	~7000	63% cationic sidechains	25 μg/mL
CM15	**KWKLFKKIGAVLKVL-NH_2**	1770	+6	5

[1] Minimum inhibitory concentration (in μM) against WT MG1655 *E. coli* over 6-hr period in aerated EZRDM medium at 30°C, determined by OD for successive two-fold dilutions in 96 well plates. Copolymer **MM_{63}:CHx_{37}** lacks a defined molar mass, so MIC is in μg/mL. The molecular weight of an "average" copolymer is ~7 kDa. This is 35 subunits long, with 37% CHx (cyclohexyl) and 63% MM (mono-methyl) sidechains; see Ref. 13 for details. Thus an MIC of 25 μg/mL corresponds to a molar concentration of about 4 μM.

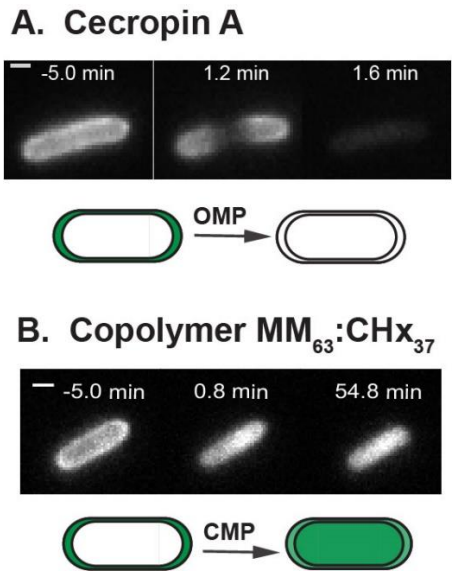

Figure 3.1 Single-cell, time-lapse assay imaging periplasmic GFP to detect membrane permeabilization events induced in live *E. coli* by antimicrobial agents. **(A)** Cecropin A at 0.9 μM (1X MIC) first induces outer membrane permeabilization to GFP, beginning at the septal region. Initial periplasmic halo image gradually disappears. **(B)** Gellman random β-peptide copolymer MM_{63}:CHx_{37} at 30 μg/mL (1.2X MIC) first induces cytoplasmic membrane permeabilization to GFP. Initial periplasmic halo image evolves to a cytoplasmic filled image of which persists for at least 55 min.

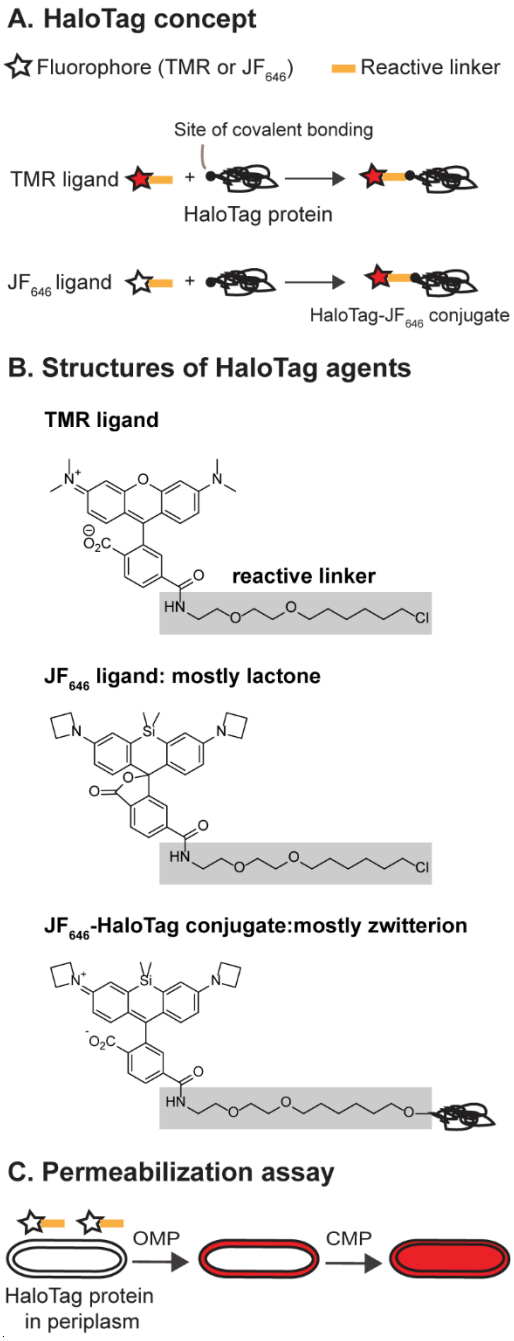

See next page for the figure legend.

Figure 3.2 Schematic of HaloTag technique for detection of outer membrane permeabilization (OMP) to small molecules. **(A)** HaloTag ligand consists of a fluorophore (such as TMR) or a profluorophore (such as JF_{646}) with a reactive chloroalkane linker (yellow line). HaloTag protein covalently binds to HaloTag ligand through the reactive linker. Free TMR ligand is already fluorescent, whereas JF_{646} ligand fluoresces much more strongly after binding to HaloTag protein. **(B)** Structures of free HaloTag TMR ligand, free HaloTag JF_{646} ligand and HaloTag-JF_{646} conjugate. The structure in the grey area is the reactive linker. **(C)** New OM permeabilization assay uses an *E. coli* strain carrying a plasmid that expresses HaloTag protein with a signal sequence causing efficient export to the periplasm. JF_{646} ligand is not permeable to intact *E. coli*. When an antimicrobial agent induces OMP to small molecules, JF_{646} ligand enters the periplasm, binds to HaloTag protein, and fluoresces in a periplasmic pattern. Subsequent CM permeabilization to globular proteins would cause the pattern to change to that of a filled cytoplasm.

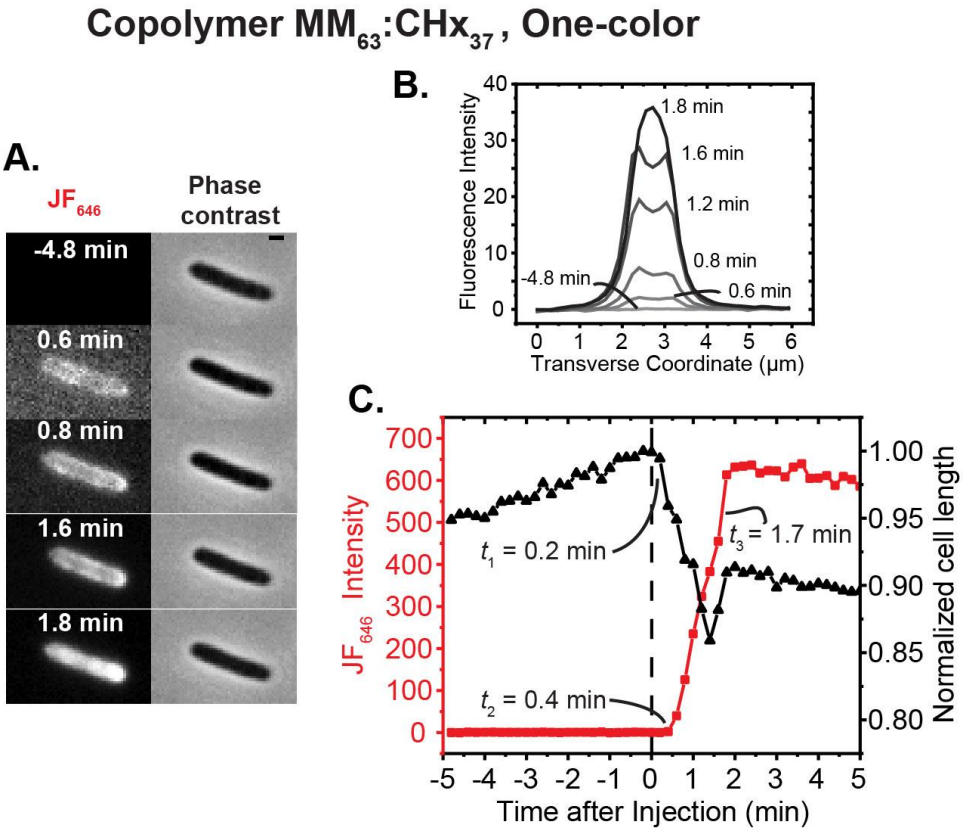

Figure 3.3 Application of one-color assay to membrane permeabilization by copolymer MM_{63}:CHx_{37}. **(A)** Red fluorescence and phase contrast snapshots of single zy3720 *E. coli* cell following addition of 30 μg/mL MM_{63}:CHx_{37} (1.2X MIC) plus 100 nM JF_{646} ligand at t = 0. Time resolution is 12 sec/cycle = 0.2 min/cycle. Scale bar is 1 μm. **(B)** Quantitative transverse intensity profiles vs time. The profile is periplasmic from 0.6 min to 1.6 min and becomes cytoplasmic at 1.8 min. **(C)** Time dependence of cell length (from phase contrast images) and total HaloTag–JF_{646} fluorescence intensity for the same cell.

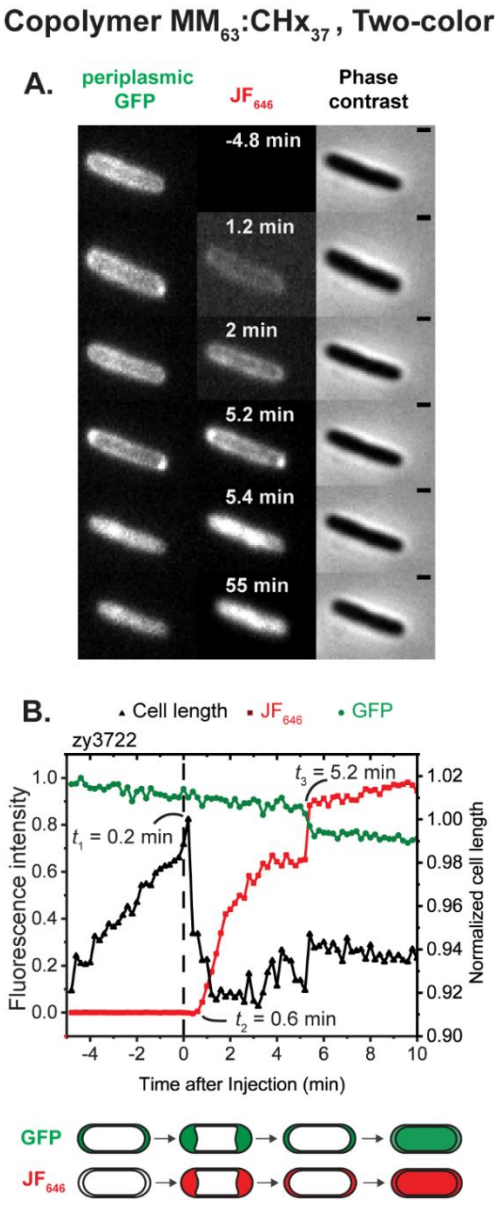

Figure 3.4 Application of two-color assay to membrane permeabilization by copolymer MM_{63}:CHx_{37}. **(A)** Phase contrast and fluorescence snapshots of single *E. coli* cell expressing periplasmic GFP and periplasmic HaloTag protein, following addition of 30 μg/mL MM_{63}:CHx_{37} (1.2X MIC) plus 100 nM JF_{646} ligand at t = 0. **(B)** Time dependence of cell length (from phase contrast images) and of GFP and JF_{646} fluorescence intensity for the same cell. Scale bar is 1μm.

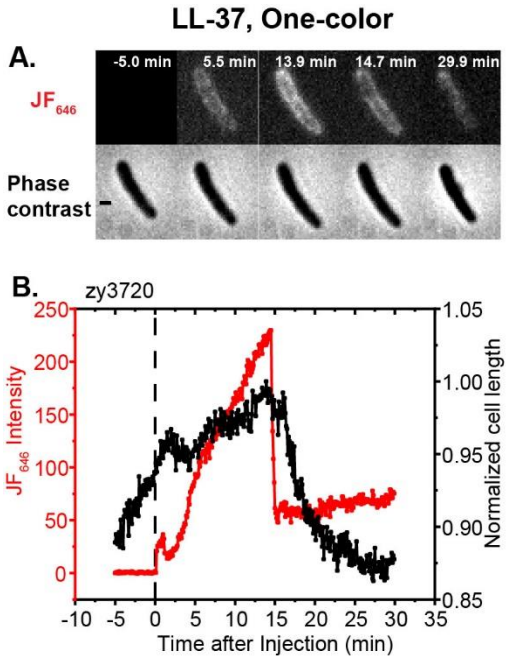

Figure 3.5 Application of one-color assay to membrane permeabilization by the antimicrobial peptide LL-37. *Top:* Red fluorescence and phase contrast snapshots of single zy3720 *E. coli* cell following addition of 4 μM LL-37 (1X MIC) plus 100 nM JF_{646} ligand at $t = 0$. Time resolution is 6 sec/cycle = 0.1 min/cycle. *Bottom:* Time dependence of cell length (from phase contrast images) and HaloTag–JF_{646} conjugate fluorescence intensity for the same cell. The fluorescence builds up in the periplasm for ~10 min, prior to the onset of significant cell shrinkage. Abrupt loss of some 75% of the intensity is attributed to OM permeabilization to globular proteins including GFP, HaloTag protein and HaloTag–JF_{646} conjugate. Simultaneous loss of GFP and HaloTag–JF_{646} conjugate was demonstrated in the two-color experiment of Appendix 3D.. Scale bar is 1 μm.

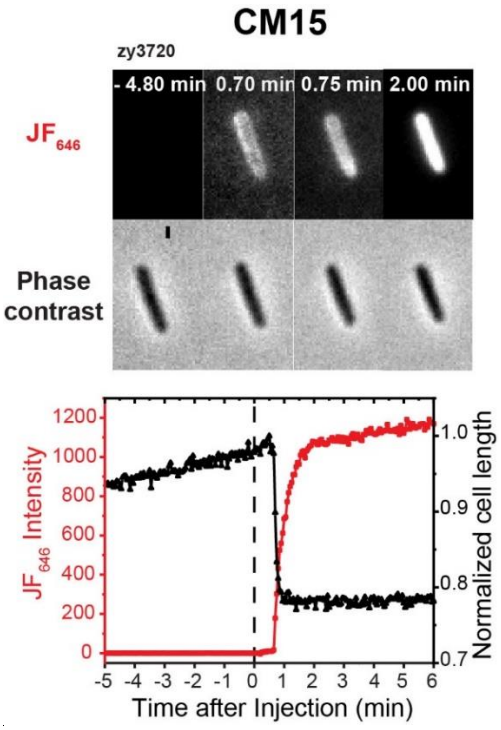

Figure 3.6 Application of one-color assay to membrane permeabilization by the antimicrobial peptide CM15. *Top:* Red fluorescence and phase contrast snapshots of single zy3720 *E. coli* cell following addition of 10 μM CM15 (2X MIC) plus 100 nM JF_{646} ligand at $t = 0$. Time resolution is 3 sec/cycle = 0.05 min/cycle. *Bottom:* Time dependence of cell length (from phase contrast images) and HaloTag–JF_{646} fluorescence intensity for the same cell. There is evidence of a transient periplasmic image at 0.70–0.75 min. The onset of red fluorescence and of cell shrinkage are simultaneous within one camera frame (3 sec).

Appendix

Methods in Detail

E. coli strains and growth conditions

The strains and plasmids used in this study are summarized in **Appendix 3A**. The background strain is MG1655 in all cases. For one-color experiments imaging periplasmic GFP only, TorA-GFP was expressed from plasmid pJW1 as previously described.[16] For one-color experiments imaging HaloTag protein only, ssMalE-Halo was expressed from plasmid pMB1 and ssDsbA-Halo was expressed from plasmid pMB2. Plasmids pMB1 and pMB2 were received from New England Biolabs.[32] For two-color experiments imaging both periplasmic GFP and HaloTag protein, TorA-GFP and ssDsbA-Halo were expressed from the same plasmid pZY2.

The expression of periplasmic HaloTag protein from plasmid pMB2 was controlled by the mutant *lacUV5* promoter: -35-TTTACA; -10-TATAAT. The expression of periplasmic HaloTag protein from plasmid pZY2 was controlled by a different mutant *lacUV5* promoter: -35-TTGACA; -10-TATAAT. Plasmid pZY2 was created by amplifying the *lacUV5* promoter ::ssDsbA::HaloTag gene from the plasmid pMB2 with a two-step polymerase chain reaction (PCR). The primers applied are forward PCR primer 1 (CTGCTGCTTGAGGAGGTACAgacatGAAAAAGATTTGGCTG), forward PCR primer 2 (GAGACTCGAGTTGACATTGTGAGCGGATAACAATATAATCTGctgctt GAGGAGGTACA), and the reverse primer (GAGAAA GCTTaccggAAATCTCCAGAGTAG). The amplified gene was cleaved with restriction enzymes (Xhoi and HindIII), and then ligated into the pJW1 plasmid to form pZY2.

Bulk cultures were grown in EZRDM,[31] which is a Mops-buffered solution supplemented with metal ions (M2130; Teknova), glucose (2 mg/mL), amino acids and vitamins (M2104;

Teknova), nitrogenous bases (M2103; Teknova), 1.32 mM K_2HPO_4, and 76 mM NaCl. Cultures were grown from glycerol frozen stock to stationary phase overnight at 30°C. Subcultures were grown to exponential phase (OD = 0.2–0.6 at 600 nm) before sampling for the microscopy experiments at 30°C.

The expression of ssMalE-Halo in strain zy3719 and ssDsbA-Halo in strain zy3720 was induced with 0.1 mM isopropyl-*β*-D-thiogalactopyranoside (IPTG) for 1 hr, before plating and imaging. In strain zy3722, the expression of TorA-GFP was the same as that in strain JCW10, and the expression of ssDsbA-Halo was induced with 1 mM IPTG for 45 min before plating and imaging. Strain JCW10, zy3719, zy3720 and zy3722 were all grown in 0.1 mg/mL ampicillin.

Minimum Inhibitory Concentration (MIC) assay

The antimicrobial agents are described in **Table 3.1**. The copolymer MM_{63}:CHx_{37} was synthesized by the Gellman lab as described before.[38-39] It is a random mixture of β-peptides with 63% cationic sidechains and 37% hydrophobic sidechains. The mean chain length is 35. The mean molecular weight is ~7 kDa. The antimicrobial peptide CM15 (H-5948) was purchased from Bachem. LL-37 (61302) was purchased from Anaspec. TMR ligand (G825B) was purchased from Promega. Fluorogenic JF_{646} ligand was kindly provided by the Lavis lab.[29]

The aerobic MIC values for the various antimicrobial agents (**Table 3.1**) were determined using the broth microdilution method as previously described.[7] The MIC value was taken as the lowest concentration for which no growth was discernible (<0.05 OD_{600}) after 6 hr.

Microscopy

Imaging of individual cells was carried out at 30°C in a simple microfluidics chamber as previously described.[11] Fresh, aerated medium flows over the cells continuously. The cells were imaged for ~5 min before switching to fresh medium containing the compounds under study

(antimicrobial agent, JF_{646} ligand). To maintain good aeration and steady bulk reagent concentrations, the flow began at 0.3 mL/min for 1 min, and then switched to 0.3 mL/hr for the remainder of the imaging.

Single-cell imaging was performed on a Nikon Eclipse Ti inverted microscope with a 100×, 1.3 N.A. phase contrast objective (Nikon) or with a 100×, 1.45 N.A. phase contrast objective (Nikon). Fluorescence images were obtained with an EMCCD camera Andor iXon 897 or Andor iXon 887. Dichroic mirror ZET 405/488/561/640x (Chroma Technology) was used for the imaging with laser excitation at 488 nm (Coherent Sapphire laser), 561 nm (Coherent Sapphire laser), and 637 nm (Vortran laser). Emission filters were: HQ525/50 (Chroma Technology) for observation of GFP after 488 nm excitation, HQ605/75 (Chroma Technology) for TMR ligand after 561 nm excitation, and 676/37 (Semrock) for JF_{646} fluorescence after 637 nm excitation. The time-lapse movies were obtained with 50-ms exposure time for each frame. One-color imaging was obtained with Andor Solis Software, with fluorescence and phase contrast images interleaved at 6-s intervals (12 s per complete cycle), unless specified otherwise. For two-color imaging, μManager was used to obtain the data and switch emission filters between frames using a LB10-NW filter wheel (Sutter). Each complete cycle of 12 s interleaved images of the green channel (488 nm excitation), the red channel (637 nm excitation), and phase contrast.

HaloTag TMR ligand and JF_{646} ligand

To visualize the spatial distribution of HaloTag protein inside *E. coli* cells, the fluorophore TMR ligand was used (**Figure 3.2B**). This ligand permeates both OM and CM and is fluorescent whether or not it is covalently bound to the HaloTag protein. When the culture OD reached ~0.4, cells were incubated with 5 μM TMR ligand for 15 min, followed by

centrifugation and washing three times with fresh EZRDM medium to remove the free intracellular TMR ligand. Finally, the cells were resuspended in 1 ml of EZRDM, followed by plating in the microfluidic chamber for imaging.

For the microfluidics experiments using the JF_{646} ligand (**Figure 3.2B**), 100 nM was incorporated into the medium. JF_{646} ligand fluoresces only weakly until covalently bound to HaloTag protein. However, at the onset of fast flow of the EZRDM medium containing JF_{646} ligand at 0.3 mL/min, the entire background lights up dramatically. This background fluorescence dims immediately beginning at t = 1 min, when the flow rate slows to 0.3 mL/hr. The underlying cause of the background is not clear. It may be characteristic of Si-rhodamine JF HaloTag ligands, because the analogue JF_{635} ligand[33] showed the same behavior. In the absence of antimicrobial agent, no obvious JF_{646} fluorescence was observed inside the cells for at least 1 hr, indicating that JF_{646} ligand by itself does not permeate the OM of *E. coli*.

Appendix 3A. Strains, doubling times, and plasmids.

	Description	**Doubling Time (min)** [1]
Strains		
MG1655	Wild type, MG1655 (K12)	50
JCW10	MG1655 + pJW1	51
zy3719	MG1655 + pMB1	-
zy3720	MG1655 + pMB2	48
zy3722	MG1655 + pZY2	49
Plasmids		
pASK-IBA3 plus	Amp^r	
pJW1	pASK-torA-GFP, signal sequence of torA fused to GFP in pASK, Amp^r	
pMB1	pDW204-ssMalE-Halo, signal sequence of MalE fused to the HaloTag in pDW204, Amp^r	
pMB2	pDW204-ssDsbA-Halo, signal sequence of DsbA fused to the HaloTag in pDW204, Amp^r	
pZY2	pASK-torA-GFP-ssDsbA-Halo, mutant *lacUV5* promoter-ssDsbA-Halo sequence inserted into pJW1, Amp^r	

[1]Doubling times for bacterial strains in EZRDM at 30°C were determined in bulk cultures by OD measurements.

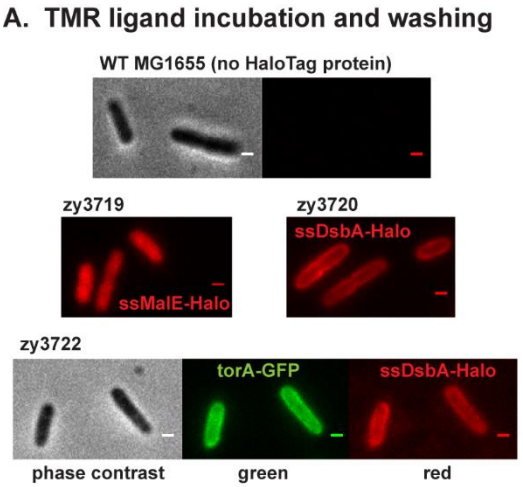

See next page for the figure legend.

Appendix 3B. Control experiments testing for export of HaloTag protein to the periplasm and permeability, non-specific binding, and toxicity of the JF_{646} ligand. Scale bars 1 μm. **(A)** *Top and middle panels*: Fluorescence images of different *E. coli* strains after incubation with red TMR ligand (**Figure 3.2B**) and washing away of excess ligand with fresh medium. TMR ligand permeates both *E. coli* membranes and specifically binds to HaloTag protein. *Top:* No obvious TMR fluorescence is observed in WT MG1655 lacking HaloTag protein. *Middle:* For strain zy3719 (expressing ssMalE–HaloTag protein), the HaloTag protein remains in the cytoplasm. For strain zy3720 (expressing ssDsbA–HaloTag), the HaloTag protein is exported to the periplasm. *Bottom:* Co-imaging of GFP and TMR in strain zy3722 (expressing both ssDsbA–HaloTag and ssTorA–GFP). Both HaloTag protein (red) and GFP (green) exhibit a periplasmic image. **(B)** Test of JF_{646} ligand (**Figure 3.2B**) permeability and toxicity in unperturbed zy3720 cells (no antimicrobial agent). *Top:* Fluorescence and phase contrast snapshots of single cell following addition of 100 nM JF_{646} ligand at $t = 0$. No fluorescence inside the cells was observed during 1 hr of flow. *Bottom:* Time dependence of cell length (from phase contrast images) and JF_{646} fluorescence intensity for the cell shown in top panel. The doubling time calculated from cell length is 52 ± 3 min. The early burst of fluorescence is background outside the cell. **(C)** Test of JF_{646} ligand fluorescence within WT *E. coli* (no HaloTag protein) after permeabilization by Gellman copolymer. *Top:* Fluorescence and phase contrast snapshots following addition of 30 μg/mL MM_{63}:CHx_{37} copolymer and 100 nM JF_{646} ligand at $t = 0$. *Bottom:* Time dependence of cell length and red fluorescence intensity for the same cell. Weak burst of fluorescence after permeabilization quickly washes away.

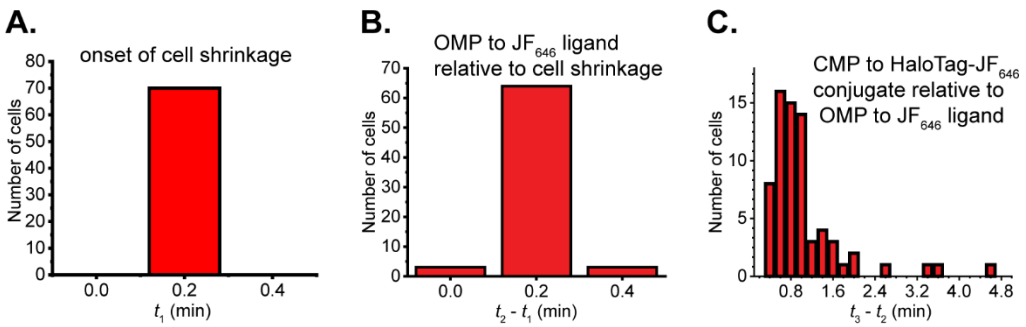

Appendix 3C. Histograms of lag times of the three membrane events after adding 30 μg/mL MM_{63}:CHx_{37} (1.2X MIC) plus 100 nM JF_{646} ligand to *E. coli* zy3720 cells expressing periplasmic HaloTag protein at $t = 0$. Notation: t_1 for onset of cell shrinkage, t_2 for onset of OM permeabilization to JF_{646} ligand, and t_3 for onset of CM permeabilization to HaloTag-JF_{646} conjugate.

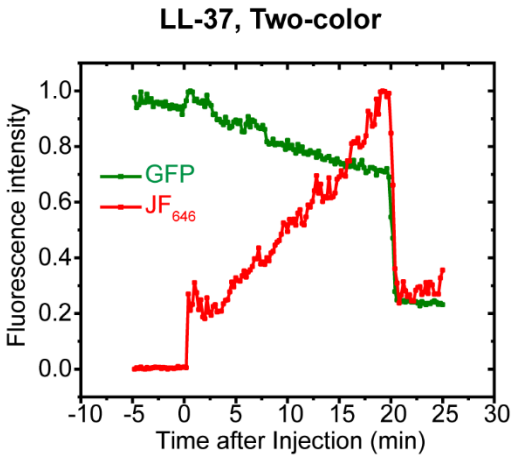

Appendix 3D. Application of two-color assay to membrane permeabilization by the antimicrobial peptide LL-37. Time dependence of GFP and JF_{646} fluorescence intensity after adding 4 μM LL-37 (1X MIC) plus 100 nM JF_{646} ligand to *E. coli* cell expressing periplasmic GFP and periplasmic HaloTag protein at $t = 0$. Time resolution is 12 sec/cycle = 0.2 min/cycle. 4 min after LL-37 addition, HaloTag–JF_{646} started to accumulate in the periplasm, until OM permeabilization to globular proteins including periplasmic GFP, HaloTag–JF_{646} conjugate and HaloTag protein occurs.

References

1. Zasloff, M., Antimicrobial peptides of multicellular organisms. *Nature* **2002,** *415*, 389-395.

2. Wimley, W. C.; Hristova, K., Antimicrobial peptides: successes, challenges and unanswered questions. *J Membr Biol* **2011,** *239* (1-2), 27-34.

3. Brogden, K. A., Antimicrobial peptides: pore formers or metabolic inhibitors in bacteria? *Nat Rev Microbiol* **2005,** *3* (3), 238-50.

4. Hancock, R. E.; Sahl, H. G., New strategies and compounds for anti-infective treatment. *Current opinion in microbiology* **2013,** *16* (5), 519-21.

5. Munoz, A.; Read, N. D., Live-cell imaging and analysis shed light on the complexity and dynamics of antimicrobial Peptide action. *Front Immunol* **2012,** *3*, 248.

6. Choi, H.; Rangarajan, N.; Weisshaar, J. C., Lights, Camera, Action! Antimicrobial Peptide Mechanisms Imaged in Space and Time. *Trends Microbiol* **2016,** *24* (2), 111-22.

7. Sochacki, K. A.; Barns, K. J.; Bucki, R.; Weisshaar, J. C., Real-time attack on single *Escherichia coli* cells by the human antimicrobial peptide LL-37. *Proc Natl Acad Sci U S A* **2011,** *108* (16), E77-81.

8. Rangarajan, N.; Bakshi, S.; Weisshaar, J. C., Localized permeabilization of *E. coli* membranes by the antimicrobial peptide Cecropin A. *Biochemistry* **2013,** *52* (38), 6584-94.

9. Barns, K. J.; Weisshaar, J. C., Real-time attack of LL-37 on single *Bacillus subtilis* cells. *Biochim Biophys Acta* **2013,** *1828* (6), 1511-20.

10. Bakshi, S.; Choi, H.; Rangarajan, N.; Barns, K. J.; Bratton, B. P.; Weisshaar, J. C., Nonperturbative imaging of nucleoid morphology in live bacterial cells during an antimicrobial peptide attack. *Appl Environ Microbiol* **2014,** *80* (16), 4977-86.

11. Choi, H.; Yang, Z.; Weisshaar, J. C., Single-cell, real-time detection of oxidative stress induced in *Escherichia coli* by the antimicrobial peptide CM15. *Proc Natl Acad Sci U S A* **2015,** *112* (3), E303-10.

12. Barns, K. J.; Weisshaar, J. C., Single-cell, time-resolved study of the effects of the antimicrobial peptide alamethicin on *Bacillus subtilis*. *Biochim Biophys Acta* **2016,** *1858* (4), 725-32.

13. Choi, H.; Chakraborty, S.; Liu, R.; Gellman, S. H.; Weisshaar, J. C., Single-Cell, Time-Resolved Antimicrobial Effects of a Highly Cationic, Random Nylon-3 Copolymer on Live *Escherichia coli*. *ACS Chem Biol* **2016,** *11* (1), 113-20.

14. Choi, H.; Yang, Z.; Weisshaar, J. C., Oxidative stress induced in *E. coli* by the human antimicrobial peptide LL-37. *PLoS Pathog* **2017,** *13* (6), e1006481.

15. Yang, Z.; Choi, H.; Weisshaar, J. C., Melittin-Induced Permeabilization, Re-sealing, and Re-permeabilization of *E. coli* Membranes. *Biophys J* **2018,** *114* (2), 368-379.

16. Sochacki, K. A.; Shkel, I. A.; Record, M. T.; Weisshaar, J. C., Protein diffusion in the periplasm of *E. coli* under osmotic stress. *Biophys J* **2011,** *100* (1), 22-31.

17. Rex, S.; Schwarz, G., Quantitative studies on the melittin-induced leakage mechanism of lipid vesicles. *Biochemistry* **1998,** *37* (8), 2336-45.

18. Gregory, S. M.; Pokorny, A.; Almeida, P. F., Magainin 2 revisited: a test of the quantitative model for the all-or-none permeabilization of phospholipid vesicles. *Biophys J* **2009,** *96* (1), 116-31.

19. Krauson, A. J.; He, J.; Wimley, W. C., Determining the mechanism of membrane permeabilizing peptides: identification of potent, equilibrium pore-formers. *Biochim Biophys Acta* **2012,** *1818* (7), 1625-32.

20. Wiedman, G.; Herman, K.; Searson, P.; Wimley, W. C.; Hristova, K., The electrical response of bilayers to the bee venom toxin melittin: evidence for transient bilayer permeabilization. *Biochim Biophys Acta* **2013,** *1828* (5), 1357-64.

21. Cruz, J.; Mihailescu, M.; Wiedman, G.; Herman, K.; Searson, P. C.; Wimley, W. C.; Hristova, K., A membrane-translocating peptide penetrates into bilayers without significant bilayer perturbations. *Biophys J* **2013,** *104* (11), 2419-28.

22. Savini, F.; Bobone, S.; Roversi, D.; Mangoni, M. L.; Stella, L., From liposomes to cells: Filling the gap between physicochemical and microbiological studies of the activity and selectivity of host-defense peptides. *Peptide Science* **2018**, e24041.

23. Wimley, W. C., How Does Melittin Permeabilize Membranes? *Biophys J* **2018,** *114* (2), 251-253.

24. Wheaten, S. A.; Ablan, F. D.; Spaller, B. L.; Trieu, J. M.; Almeida, P. F., Translocation of cationic amphipathic peptides across the membranes of pure phospholipid giant vesicles. *J Am Chem Soc* **2013,** *135* (44), 16517-25.

25. Zakharov, S. D.; Sharma, O.; Zhalnina, M.; Yamashita, E.; Cramer, W. A., Pathways of colicin import: utilization of BtuB, OmpF porin and the TolC drug-export protein. *Biochemical Society transactions* **2012,** *40* (6), 1463-8.

26. Loh, B.; Grant, C.; Hancock, R. E., Use of the fluorescent probe 1-N-phenylnaphthylamine to study the interactions of aminoglycoside antibiotics with the outer membrane of Pseudomonas aeruginosa. *Antimicrobial Agents and Chemotherapy* **1984,** *26* (4), 546-551.

27. Lehrer, R. I.; Barton, A.; Ganz, T., Concurrent assessment of inner and outer membrane permeabilization and bacteriolysis in E. coli by multiple-wavelength spectrophotometry. *Journal of Immunological Methods* **1988,** *108* (1), 153-158.

28. Junkes, C.; Wessolowski, A.; Farnaud, S.; Evans, R. W.; Good, L.; Bienert, M.; Dathe, M., The interaction of arginine- and tryptophan-rich cyclic hexapeptides with *Escherichia coli* membranes. *J Pept Sci* **2008,** *14* (4), 535-43.

29. Grimm, J. B.; English, B. P.; Chen, J.; Slaughter, J. P.; Zhang, Z.; Revyakin, A.; Patel, R.; Macklin, J. J.; Normanno, D.; Singer, R. H.; Lionnet, T.; Lavis, L. D., A general method to improve fluorophores for live-cell and single-molecule microscopy. *Nat Methods* **2015,** *12* (3), 244-50, 3 p following 250.

30. Los, G. V.; Encell, L. P.; McDougall, M. G.; Hartzell, D. D.; Karassina, N.; Zimprich, C.; Wood, M. G.; Learish, R.; Ohana, R. F.; Urh, M.; Simpson, D.; Mendez, J.; Zimmerman, K.; Otto, P.; Vidugiris, G.; Zhu, J.; Darzins, A.; Klaubert, D. H.; Bulleit, R. F.; Wood, K. V., HaloTag: A Novel Protein Labeling Technology for Cell Imaging and Protein Analysis. *ACS Chemical Biology* **2008,** *3* (6), 373-382.

31. Neidhardt, F. C.; Bloch, P. L.; Smith, D. F., Culture medium for enterobacteria. *J Bacteriol* **1974,** *119* (3), 736-47.

32. Ke, N.; Landgraf, D.; Paulsson, J.; Berkmen, M., Visualization of Periplasmic and Cytoplasmic Proteins with a Self-Labeling Protein Tag. *J Bacteriol* **2016,** *198* (7), 1035-43.

33. Grimm, J. B.; Muthusamy, A. K.; Liang, Y.; Brown, T. A.; Lemon, W. C.; Patel, R.; Lu, R.; Macklin, J. J.; Keller, P. J.; Ji, N.; Lavis, L. D., A general method to fine-tune fluorophores for live-cell and in vivo imaging. *Nat Methods* **2017,** *14* (10), 987-994.

34. Ladokhin, A. S.; White, S. H., 'Detergent-like' permeabilization of anionic lipid vesicles by melittin. *Biochimica et Biophysica Acta (BBA) - Biomembranes* **2001,** *1514* (2), 253-260.

35. Shai, Y., Mechanism of the binding, insertion and destabilization of phospholipid bilayer membranes by alpha-helical antimicrobial and cell non-selective membrane-lytic peptides. *Biochim Biophys Acta* **1999,** *1462* (1-2), 55-70.

36. Lee, M. T.; Chen, F. Y.; Huang, H. W., Energetics of pore formation induced by membrane active peptides. *Biochemistry* **2004,** *43* (12), 3590-9.

37. Yamaguchi, S.; Hong, T.; Waring, A.; Lehrer, R. I.; Hong, M., Solid-State NMR Investigations of Peptide−Lipid Interaction and Orientation of a β-Sheet Antimicrobial Peptide, Protegrin. *Biochemistry* **2002,** *41* (31), 9852-9862.

38. Mowery, B. P.; Lee, S. E.; Kissounko, D. A.; Epand, R. F.; Epand, R. M.; Weisblum, B.; Stahl, S. S.; Gellman, S. H., Mimicry of antimicrobial host-defense peptides by random copolymers. *J Am Chem Soc* **2007,** *129* (50), 15474-15475.

39. Mowery, B. M.; Lindner, A. M.; Weisblum, B.; Stahl, S. S.; Gellman, S. H., Structure-Activity Relationships Among Random Nylon-3 Copolymers that Mimic Antibacterial Host-Defense Peptides. *J Am Chem Soc* **2009,** *131*, 9735.

Chapter 4

Oxidative stress induced in *E. coli* by the human antimicrobial peptide LL-37

Adapted from publication listed below:

Choi, H., Yang, Z., and Weisshaar, J. C. (**2017**) Oxidative stress induced in *E. coli* by the human antimicrobial peptide LL-37, *PLoS Pathogens 13*, e1006481.

* ZY, HC, and JCW all contributed to design of the project. Choi, H. and Yang, Z. contributed equally to this work. Both HC and ZY performed experiments. HC, ZY and JCW analyzed the data and wrote the manuscript. The supplemental movies are available online.

Abstract

Antimicrobial peptides (AMPs) are thought to kill bacterial cells by permeabilizing their membranes. However, some antimicrobial peptides inhibit *E. coli* growth more efficiently in aerobic than in anaerobic conditions. In the attack of the human cathelicidin LL-37 on *E. coli*, real-time, single-cell fluorescence imaging reveals the timing of membrane permeabilization and the onset of oxidative stress. For cells growing aerobically, a CellROX Green assay indicates that LL-37 induces rapid formation of oxidative species after entry into the periplasm, but before permeabilization of the cytoplasmic membrane (CM). A cytoplasmic Amplex Red assay signals a subsequent burst of oxidative species, most likely hydrogen peroxide, shortly after permeabilization of the CM. These signals are much stronger in the presence of oxygen, a functional electron transport chain, and a large proton motive force (PMF). They are much weaker in cells growing anaerobically, by either fermentation or anaerobic respiration. In aerobic growth, the oxidative signals are attenuated in a cytochrome oxidase–*bd* deletion mutant, but not in a –bo_3 deletion mutant, suggesting a specific effect of LL-37 on the electron transport chain. The AMPs melittin and LL-37 induce strong oxidative signals and exhibit O_2-sensitive MICs, while the AMPs indolicidin and cecropin A do not. These results suggest that AMP activity in different tissues may be tuned according to the local oxygen level. This may be significant for control of opportunistic pathogens while enabling growth of commensal bacteria.

Introduction

Antimicrobial peptides (AMPs, also called host-defense peptides) play a number of important roles in the innate immune response of plants and animals [1]. Important human AMPs include the cathelidicin LL-37 and the defensins [2]. In humans, AMPs are constitutively expressed in phagocytes, including macrophages, neutrophils, and dendritic cells [3, 4]. When a pathogen attacks the host, phagocytes initially envelope the invading microbes in internal phagosomes [5]. The phagosome fuses with lysosomes to form the phagolysosome. Presence of the pathogen stimulates a "respiratory burst" in the phagocyte, leading to synthesis of harmful reactive oxygen species (ROS) within the phagolysosome [6, 7]. In parallel, AMPs stored in granules are released into the phagolysosome, where their high concentration likely contributes to direct killing of the invading pathogen. AMPs are also released from the phagocyte into surrounding tissue and the bloodstream. In addition to directly attacking pathogens, these external AMPs serve a variety of immunoregulatory functions [8, 9].

Most AMPs are cationic and amphipathic. They are attracted to the anionic outer surfaces of bacterial cells and, at sufficient concentration, permeabilize bacterial membranes. In early studies, the halting of growth of bacterial pathogens by AMPs was typically attributed to permeabilization of the cytoplasmic membrane (CM), with concomitant loss of the proton motive force (pmf), loss of critical small molecules, and halting of ATP production. However, over the past 15 years, many studies have shown that AMPs cause a variety of deleterious biophysical and biochemical effects in bacterial cells, including interference with cell wall biosynthesis, DNA replication, transcription, and translation [10-13]. Induction of reactive oxygen species (ROS) has received little attention as a potentially important aspect of AMP action against bacterial cells [14].

We recently used time-resolved, single-cell fluorescence microscopy [15-19] to show that the hybrid synthetic peptide CM15 (15 aa long, net +6 charge) induces oxidative stress within seconds of contact with *E. coli* growing in aerobic conditions [20]. The minimum inhibitory concentration (MIC) was 20-fold higher in anaerobic (fermentation) conditions than in aerobic growth, suggesting that induction of oxidative stress may be a significant growth-halting mechanism. Additional evidence from the oxidation sensitive dye CellROX Green and an intracellular Amplex Red assay suggested that CM15 may interfere with the electron transport chain, possibly leading to formation of superoxide ($\bullet O_2^-$) and hydroxyl radical (•OH) as well as hydrogen peroxide (H_2O_2) [21]. We observed analogous effects of oxygen for **MM_{63}:CHx_{37}**, a potent example of a highly cationic, random β-peptide copolymer (mean chain length 35 units, 63% cationic sidechains) [22]. The MIC of this copolymer against *E. coli* is at least 8-fold lower in aerobic than in anaerobic conditions.

Both CM15 and **MM_{63}:CHx_{37}** are synthetic peptides. To get a better sense of the generality of these phenomena, here we extend our studies of oxidative effects to four natural AMPs (**Table 4.1**): LL-37 (human cathelicidin, α-helical, 37 aa long, net +6), cecropin A (moth, α-helical, 37 aa long, net +7)), melittin (bee, α-helical, 26 aa long, net +6), and indolicidin (bovine, extended structure, 13 aa long, net +4). LL-37 and melittin exhibit significantly lower MICs against *E. coli* in aerobic vs anaerobic (fermentation) conditions, and they both induce strong fluorescence signals indicative of oxidative stress. In contrast, for cecropin A and indolicidin the MIC is the same in aerobic and anaerobic conditions. Correspondingly, they induce much weaker fluorescence signals.

In addition, we provide a detailed, single-cell comparison of LL-37 attacking *E. coli* growing under conditions of aerobic respiration, anaerobic fermentation, and anaerobic respiration. In

aerobic growth, a burst of oxidative species is induced already on access of LL-37 to the periplasm, *i.e.*, well before the cytoplasmic membrane is permeabilized to the dye Sytox Orange. The mechanism may involve interference with proteins of the electron transport chain (ETC), leading to improper release of superoxide ($\bullet O_2^-$) into the periplasmic space. Mutation studies suggest that LL-37 targets the cytochrome oxidase-*bd* complex, but not the cytochrome oxidase-bo_3 complex. A subsequent burst of oxidative species, detected by an intracellular Amplex Red assay sensitive to H_2O_2, rose sharply at the moment of CM permeabilization. For cells growing by anaerobic fermentation or by anaerobic respiration using NO_3^- as terminal electron acceptor, no such signals of abrupt oxidative events were observed. However, the CellROX Green and Amplex Red assays are insensitive to oxidative nitrogen-containing radicals, so that oxidative damage might still be occurring.

These new results suggest the possibility that the host may use the degree of tissue aeration for selective control of the potency of AMPs. The present work indicates that LL-37 is most potent against *E. coli* in oxygen-rich conditions. Earlier work found the same effect for the human beta defensin hBD-3, but the opposite effects for hBD-1 [23]. Reduction of the Cys-Cys linkages in hBD-1, which converts the globular oxidized structure to a linear structure, greatly enhanced its antimicrobial activity against anaerobic Gram positive species. Tuning of cationic AMP activity according to local redox conditions may prove to be important in controlling opportunistic pathogens while enabling growth of commensal bacteria.

Methods

Bacterial strains, materials, and growth conditions. The strains are listed in Table **4.2**. The background ("WT") strain is MG1655 (K12) in all cases. Experiments on periplasmic GFP used strain JCW10, in which TorA-GFP is expressed from plasmid pJW1 as previously described

[26]. TorA-GFP is transported to the periplasm by the twin-arginine transport system and the TorA signal peptide is cleaved, leaving free GFP in the periplasm. ZY01 is the strain that expresses the peroxidase APEX2 from a plasmid introduced into the background strain, as described previously [20]. To construct the deletion mutant strain called Δ*cyoABCDE*, lacking the gene for cytochrome-bo_3 oxidase, we performed λ-Red reconstruction, replacing the *cyoABCDE* gene with a kanamycin resistance gene. The deletion of the *cyoABCDE* gene and the replacement by a kanamycin resistance gene were confirmed by PCR and DNA sequencing. The deletion mutant strain Δ*cydAB* was constructed and confirmed analogously. To visualize resorufin generation in the Δ*cyoABCDE* deletion mutant, we transformed a pASK-IBA3plus vector containing the APEX2 gene into Δ*cyoABCDE*, yielding strain ZY02.

Unlabeled LL-37 lacking a C-terminal amide was purchased from Anaspec (61302). Rhodamine B-LL-37 (no C-terminal amide) was purchased from Bachem (4049885). The oxidation sensitive dye CellROX Green (C10444) and Amplex Red (A22188) were purchased from Invitrogen. The DNA stains Sytox Green (S7020) and Sytox Orange (S11368) were purchased from Thermo-Fisher Scientific.

Bulk cultures were grown in EZ rich, defined medium (EZRDM) [40], which is a MOPS-buffered solution at pH = 7.4 supplemented with metal ions (M2130; Teknova), glucose (2 mg/mL), amino acids and vitamins (M2104; Teknova), nitrogenous bases (M2103; Teknova), 1.32 mM K_2HPO_4, and 76 mM NaCl. Cultures were grown from glycerol frozen stock to stationary phase overnight at 30°C. Subcultures were grown to exponential phase (OD = 0.2–0.6 at 600 nm) at 30°C before sampling for the microscopy experiments.

Minimum Inhibitory Concentration (MIC) Assay. The aerobic MIC values for the various AMPs (**Table 4.1**) were determined using the broth microdilution method as previously

described [19]. Two-fold serial dilutions of LL-37 in 1× EZRDM were performed in separate rows of a polystyrene 96-well plate, with each plate containing an inoculum of *E. coli* MG1655. The inoculum was a 1:20 dilution from a bulk culture at midlog phase (OD600 = 0.5) grown at 30°C. The plate was incubated at 30°C and shaken at 200 rpm in a Lab-Line Orbital Environ Shaker (model 3527) for 6 hr. The MIC value was taken as the lowest concentration for which no growth was discernible (<0.05 OD) after 6 hr.

Anaerobic MIC values (**Table 4.1**) were measured on a 96-well plate that was sealed with plastic wrap. Cells were incubated in EZRDM containing protocatechuic acid (PCA) at 10 mM and protocatechuate 3,4-dioxygenase (PCD) at 100 nM to scavenge oxygen [41]. The plate was incubated at 30°C for 6 hr, followed by OD measurements. In the earlier study of CM15 [20], we tested that PCA by itself does not interfere with CellROX* fluorescence.

Time-lapse recovery assay. The time-lapse recovery assays utilized an MG1655 culture in bulk. Overnight culture of wild-type MG1655 was inoculated at 1:100 dilution in 2 mL EZRDM at 30°C. When the culture is at midlog phase (OD600 = 0.5), the culture was diluted with warmed EZRDM to 1:10 and incubated with different concentrations (0, 4, 8, and 16 μM) of LL-37. 100 uL of each culture was sampled at different time point (30 min, 1-hr. and 2-hr incubation). Then, each culture was 10-fold serial diluted with warmed EZRDM into a 96-well plate. Each dilution was plated into fresh LB agar plates and the plates were incubated at 30°C for 24 hr. The plates were then visually inspected for growth of colonies. The control procedure was the same except that the LL-37 was omitted. See **Appendix 4A** for results.

Microfluidics chamber for aerobic and anaerobic microscopy. As previously described [20], imaging of individual cells was carried out at 30°C in a microfluidics chamber consisting of a single rectilinear channel of uniform height of 50 μm and width of 6 mm, with a channel length

of 11 mm. The total chamber volume is ~10 μL. After bonding of the PDMS chamber to the glass coverslip, 0.01% poly-L-lysine (molecular weight >150,000 Da) was injected through the chamber for 30 min and rinsed thoroughly with Millipore water. *E. coli* cells are immobilized on the coverslip but grow normally. During imaging experiments, the chamber was maintained at 30°C with an automatic temperature controller.

For aerobic imaging experiments, the medium is exposed to air over three hr while held at 30°C in a shaker bath; this ensures full oxygenation of the medium. In addition, the PDMS ceiling of the microfluidics device is permeable to the ambient gases N_2 and O_2. For anaerobic imaging experiments, O_2 must be prevented from entering the chamber through its ceiling. A small anaerobic chamber surrounding the microfluidics device was constructed of aluminum with a nitrogen gas inlet and outlet. Details are provided elsewhere [20]. Before injection of cells, nitrogen gas flowed through the chamber continuously for 1.5 hr. *E. coli* were grown in aerobic conditions until injected into the chamber. Fresh deoxygenated EZRDM was made by treating EZRDM with 50 nM protocatechuate 3,4-dioxygenase (PCD) and 2.5 mM protocatechuic acid (PCA). This was used to wash the cells at 30°C before plating. Deoxygenated EZRDM (with or without addition of 10 mM KNO_3) then flowed across the plated cells for 30 min before injection of antimicrobial peptides and CellROX. The subsequent microscopy imaging experiment was carried out as before.

Microscopy. Single-cell imaging was performed on two different microscopes: a Nikon TE300 inverted microscope with a 100×, 1.3 N.A. phase contrast objective and a Nikon Eclipse Ti inverted microscope with a 100×, 1.45 N.A. phase contrast objective. For the TE300, images were further magnified 1.45× in a home-built magnification box. GFP, Sytox Green, and CellROX* were imaged using 488 nm excitation (Coherent Sapphire laser), expanded to

illuminate the field of view uniformly. The emission filter was HQ525/50 (Chroma Technology). Resorufin and Sytox Orange were imaged using 561 nm excitation (Coherent Sapphire laser). The emission filter was HQ617/73 (Chroma Technology). Laser intensities at the sample were typically ~5 W/cm^2 at 488 nm and ~2.5 W/cm^2 at 561 nm. Fluorescence images were obtained with an EMCCD camera, either Andor iXon 897 or Andor iXon 887. In both cases, the pixel size corresponds to 110 ± 10 nm at the sample.

For single color experiments, time-lapse movies of 60-min total duration were obtained as 600 frames of 50-ms exposure time each, with fluorescence and phase contrast images interleaved at 6-s intervals (12 s per complete cycle). For dual color experiments, µManager was used to obtain the data and switch filters between frames using a LB10-NW filter wheel (Sutter). The time-lapse movies of 35-min total duration were obtained as 1050 frames of 50-ms exposure time each, with green fluorescence (488 nm excitation), red fluorescence (561 nm excitation), and phase contrast images interleaved (6 s per complete cycle). To minimize spectral bleed-through in the two-color experiments, we utilized the narrower filters HQ510/20 for the green channel and HQ600/50M for the red channel.

CellROX Green Oxidation Assay. CellROX Green (Life Technologies) is a proprietary oxidation-sensitive dye whose fluorescence quantum yield at 500-550 nm after excitation at 488 nm increases dramatically on oxidation in the presence of ds-DNA. It readily permeates both *E. coli* membranes. The manufacturer tested its sensitivity to different reactive oxygen species in the presence of ds-DNA *in vitro* including hydroxyl radical (•OH), superoxide (O_2^-), hydrogen peroxide (H_2O_2), peroxynitrite ($ONOO^-$), nitric oxide (NO), and hypochlorite (ClO^-). The only two oxidizing agents that significantly enhanced CellROX* fluorescence were hydroxyl radical and superoxide. Importantly, hydrogen peroxide has no effect.

In the CellROX* imaging experiments, MG1655 cells were injected into the microfluidics chamber. After allowing 5 min for plating of cells, the bulk solution was washed away with fresh, pre-warmed, aerated EZRDM. After the wash, cells were grown for 5 min prior to the injection of 4 μM LL-37 plus 2.5 μM CellROX Green. To maintain good aeration and steady bulk concentrations, the medium with LL-37 and CellROX Green flowed continuously at 0.3 mL/hr.

Amplex Red Oxidation Assay. As previously described [20], the assay for single-cell, time-resolved measurement of H_2O_2 production following LL-37 treatment is based on the well-established Amplex Red method [30]. Some peroxidases (but not the catalases naturally occurring in *E. coli*) catalyze reaction of the dye Amplex Red with H_2O_2 to form the red fluorescent species resorufin (λ_{em} = 585 nm). Recently Collins and coworkers [29] adapted the method to carry out the Amplex Red + H_2O_2 reaction inside the cytoplasm by inserting a plasmid that expresses the peroxidase APEX2 (mutated ascorbate peroxidase). Their method detects H_2O_2 produced inside the cell using plate-based bulk fluorescence measurements with time resolution of ~60 min. Here we use intracellular APEX2 combined with single-cell, time-resolved detection by fluorescence microscopy. This enables sensitive detection of intracellular H_2O_2 production with 12-s time resolution and correlation of LL-37-induced H_2O_2 production with other events in real time.

Results

Minimum inhibitory concentration of some AMPs depend on growth conditions. We have measured MICs in aerobic and anaerobic fermentation conditions using a series of two-fold dilutions for the four natural AMPs in the same rich, chemically defined EZRDM medium at 30°C (**Table 4.1**). The MIC in anaerobic fermentation conditions is 4-fold higher for LL-37 and

8-fold higher for melittin. Multiple experimental runs produce the same MIC value within the resolution of the two-fold dilution steps, indicating that 4-fold and 8-fold differences are significant. For cecropin A and for indolicidin, the MIC is the same in aerobic and fermentation conditions. Evidently the activity against *E. coli* of some, but not all, natural AMPs is enhanced by the presence of oxygen. For LL-37, the primary focus of this study, we also measured the MIC in conditions enabling anaerobic respiration (no oxygen, but supplemented with 10 mM KNO_3; **Table 4.2**). The MIC is 12 μM, three times higher than in aerobic respiration.

The doubling times for MG1655 growing in EZRDM at 30°C under aerobic respiration, anaerobic respiration with KNO_3, and fermentation conditions are similar, all in the range 45–53 min (**Table 4.2**). Earlier work in M9 medium supplemented with hydrolyzed casein [24] found that *E. coli* maintained a substantial proton motive force (pmf) in all three growth conditions (–160 mV for aerobic respiration, –144 mV for anaerobic respiration using NO_3^-, and –117 mV for fermentation). These pmf values may not be transferable to our strain and growth conditions.

Bactericidal effects of LL-37 at the minimum inhibitory concentration in aerobic growth conditions. We chose the human cathelicidin LL-37 for a detailed time-dependent, single-cell study of antimicrobial action. First we investigated the extent to which LL-37 in aerobic conditions at the 6-hour MIC of 4 μM causes cell death (irreversible halting of growth) on the timescale of our microscopy measurements, typically 30-60 min. We monitored cell killing activity using a conventional cell survival assay. A mid-log phase culture of MG1655 *E. coli* was incubated with LL-37 at 4 μM, sampled after 30 min, 1 hr, and 2 hr of incubation, and serially diluted over the range 5×10^6 to 5 cells/mL. One μL of the diluted sample was spot-plated onto a 3% LB-agar plate for overnight growth at 30°C. In control experiments, no LL-37 was added

prior to plating and incubation. At 4 μM LL-37, we observe a significant decrease in colony formation after 30 min of incubation when compared to the control (**Appendix 4A**). After 1-hr incubation at 4 μM, essentially no colonies formed, even for the least diluted sample. These results were reproducible over three trials. According to classic clinical microbiological definitions, this indicates that the MIC and the minimum bactericidal concentration (MBC) for LL-37 are essentially the same. At 4 μM of LL-37, both growth inhibition and cell death occur within a 1-hr period. This indicates that the single-cell signs of LL-37 attack as observed under the microscope on the 30-60 minute timescale are likely relevant to cell killing activity.

Sequence of membrane permeabilization events in aerobic growth conditions. For individual *E. coli* cells, time-lapse microscopy can determine the timing of the slowing or halting of cell growth, of outer membrane permeabilization, and of cytoplasmic membrane permeabilization following the onset of flow of LL-37 (Methods). Warm (30°C), aeriated EZRDM growth medium flows continuously across the plated cells. Over an observation period of 30-60 min, we alternate phase contrast images with fluorescence images (either one or two colors) and make time-dependent, quantitative measurements of cell length and total fluorescence intensity. In the first set of measurements, the *E. coli* cells express GFP that is exported to the periplasm by the twin-arginine transport (Tat) system [25]. This produces a characteristic halo image [26]. The medium contains 5 nM of the DNA stain Sytox Green, which becomes fluorescent on crossing both membranes and binding to the chromosomal DNA within the cytoplasm. We directly observe cell length vs time (from phase contrast), the onset of permeabilization of the OM to periplasmic GFP (observed as loss of the green halo surrounding the cytoplasm), and the onset of permeabilization of the CM to Sytox Green (from green staining of the nucleoids).

At $t = 0$, we initiate flow of 4 μM LL-37 (the 6-hr MIC) in aerated medium through the microfluidics observation chamber. For the example cell in **Figure 4.1**, the growth rate (slope of the plot of cell length vs time) begins to decrease immediately after injection of LL-37. For at least 90% of the cells in a typical field of 50 cells, we observe gradual slowing or abrupt halting of growth within 10 min of injection. Over the first 30 min after injection of LL-37, 60% of the cells lose the "halo" of periplasmic GFP, indicating OM permeabilization to GFP (**Figure 4.1C**). During the same 30 min, the other 40% of the cells exhibit an attenuated growth rate, yet continue to elongate without loss of periplasmic GFP. Loss of GFP begins over a wide range of times (2–50 min). Once it begins, complete loss of GFP occurs fairly quickly, over the subsequent 2-3 min. The onset of GFP intensity loss almost always coincides with moderate shrinkage of cell length. As observed before [19], obviously septating cells tend to undergo OM permeabilization earlier than apparently non-septating cells.

For the 60% of cells that undergo OM permeabilization before $t = 30$ min, growth halts. A new signal from Sytox Green begins to rise within 5 min of the OM permeabilization event (example in **Figure 4.1** and S1 Movie). Green fluorescence evolves in the cytoplasm in a spatial pattern reminiscent of the distribution of the *E. coli* nucleoids, indicating CM permeabilization to Sytox Green. Permeabilization of the CM correlates in time with additional shrinkage of cell length, presumably due to loss of osmolytes from the cytoplasm. The 40% of cells that continued to elongate slowly for the first 30 min did not display a Sytox Green signal during that period, indicating that both the CM and the OM remained intact. However, eventually almost all cells exhibit both OM and CM permeabilization within a 1-hr period after LL-37 addition, as shown by the cumulative distribution function of the lag times to CM permeabilization (**Figure 4.1C**).

The timescale of the halting of growth observed in these single-cell permeabilization experiments at the MIC is consistent with the results of the bulk, time-lapse bactericidal assay.

Overview of real-time oxidative stress signals. The MIC data suggest that the halting of growth at 4 μM of LL-37 is mediated by oxygen. Our working hypothesis is that LL-37 induces formation of harmful reactive oxygen species (ROS). In an earlier study of CM15 [20], we developed two single-cell, real-time fluorescence measurements that monitor oxidative stress using the dyes CellROX Green and Amplex Red. CellROX Green (Life Technologies) is a proprietary, permeable, non-fluorescent, oxidation-sensitive dye. Oxidation produces a species we call CellROX*, which fluoresces in the green, but only when bound to ds-DNA. *In vitro*, CellROX Green is sensitive to superoxide ($\bullet O_2^-$) and to hydroxyl radical (•OH), but not to hydrogen peroxide (H_2O_2) or to a variety of other oxidants including peroxynitrite ($ONOO^-$), NO, and hypochlorite (OCl^-). In the cellular environment, other species such as high-valence Fe centers could also oxidize CellROX Green [27, 28]. Amplex Red is a permeable dye whose reaction with H_2O_2 is catalyzed by the non-native peroxidase APEX2, expressed in the cytoplasm from a plasmid [29, 30]. The product is resorufin, which fluoresces in the red. The specificity of the enzymatic reaction strengthens the assumption that resorufin fluorescence signals H_2O_2 formation.

We monitor oxidative stress by measuring single-cell fluorescence of CellROX* or resorufin (in cells expressing APEX2) as a function of time after LL-37 addition. The duration of each complete imaging cycle is 12 s for one-color imaging and 6 s for two-color imaging.

Onset of CellROX* fluorescence occurs on entry of LL-37 into the periplasm. First we carried out the CellROX* assay in aerobic conditions using 4 μM of LL-37 (the aerobic MIC).

At $t = 0$ the flow was switched to medium including LL-37 and 2.5 μM CellROX Green. Laser intensities and imaging conditions were held constant, enabling quantitative intensity comparisons across different experiments. More than 90% of 171 cells from three repeats of the experiment exhibit attenuation of growth rate or abrupt shrinkage within 10 min of injection of LL-37 (example in **Figure 4.2A, B** and S2 Movie), as was observed in the periplasmic GFP experiments. For the particular cell in **Figure 4.2**, halting of growth and mild shrinkage occurs shortly after $t = 0$. At $t = 2$ min, CellROX* fluorescence intensity begins to increase gradually; the intensity continues to rise for about ten minutes, when it turns sharply downward and decays to a non-zero plateau. At the same moment, cell length begins a second period of gradual shrinkage. For all cells whose length begins to decrease at $t < 30$ min, we eventually observe a sudden decrease in CellROX* signal to a non-zero plateau. We show below that this decrease typically correlates in time with the moment of CM permeabilization to the DNA stain Sytox Orange. Those cells that continue to grow slowly over the first 30 min (no CM permeabilization), exhibit a much weaker CellROX* signal that increases slowly throughout the observation period.

Control experiments indicate that the peak CellROX* signal induced by LL-37 from 58 analyzed cells is on average ten times larger than the magnitude of the slowly rising green fluorescence signal observed at $t = 30$ min in the absence of LL-37 (**Figure 4.3A**). These data suggest that the strong CellROX* fluorescence begins to rise when LL-37 penetrated the OM and gains access to the periplasm. Experiments using two-color imaging of CellROX* and Rhodamine B-LL-37 will corroborate this inference.

To directly confirm that CellROX* begins to rise before CM permeabilization, we carried out two-color fluorescence experiments in aerobic conditions, injecting both 2.5 μM CellROX

Green and 5 nM of the DNA stain Sytox Orange into the growth medium at $t = 0$. Observations were then carried out for 30 min. A typical example of the two fluorescence traces from a single cell that undergoes CM permeabilization during the observation period is shown in **Figure 4.4A**. See also S3 Movie. A strong CellROX* fluorescence begins to rise some 10 min before the abrupt onset of Sytox Orange fluorescence, which in turn marks the moment when the CM is permeabilized. The CellROX* signal then typically decreases abruptly by about 60% and stabilizes at a lower value. As before, the abrupt decrease in CellROX* fluorescence occurred in all cells exhibiting CM permeabilization over 30 min. Most often the CellROX* signal decrease begins within 1 min of CM permeabilization, but in about 1/3 of 39 cells the decrease begins 2–15 min after CM permeabilization. A histogram in shown in **Appendix 4F**.

Additional evidence that the onset of strong CellROX* fluorescence coincides with entry of LL-37 into the periplasm comes from two-color imaging experiments using CellROX Green and a red fluorescent variant of the peptide, Rh-LL-37. Earlier we showed that Rh-LL-37 and unlabeled LL-37 have the same MIC vs MG1655 *E. coli*, although membrane permeabilization events occurred somewhat more slowly for Rh-LL-37 [19]. Under aerobic growth conditions, at $t = 0$ we flowed 25 μM CellROX Green plus 8 μM Rh-LL-37 across plated *E. coli* cells. A representative result is shown in **Figure 4.4B**. As before [19], weak red fluorescence from Rh-LL-37 initially coats all cells uniformly (plateau of red fluorescence at $t = 2–17$ min). We attribute this to binding of Rh-LL-37 oligomers to the lipopolysaccharide (LPS) layer. The weak plateau of green fluorescence is a background signal that also coats all cells uniformly. This background is not CellROX* fluorescence, because it occurs on addition of Rh-LL-37 in the absence of CellROX Green.

Like LL-37, Rh-LL-37 preferentially attacks septating cells. As observed earlier [19], septating cells gradually exhibit a brighter band of red fluorescence that begins at the septal region and slowly spreads to the entire periplasm over 5-10 min (**Figure 4.4B**). In salty solution Rh-LL-37 fluorescence is self-quenched due to bundling of multiple helices. We believe that this self-quenching persists during binding to the LPS layer of *E. coli*, rendering the initial wave of red fluorescence weak. Entry into the periplasm at the septal region unbundles the helices, causing dequenching of fluorescence and gradual development of the brighter red band. Evidently Rh-LL-37 enters at the septal region and binds strongly to some immobile element of the periplasm, possibly the anionic cross-links within the peptidoglycan layer. As local binding sites become occupied, unbundled Rh-LL-37 slowly migrates towards the tips of the periplasm, observed as a gradual outward spreading of the brighter red band. In earlier work, we showed that Rh-LL-37 binds to purified peptidoglycan [19].

As shown in the example of **Figure 4.4B**, the green fluorescence from CellROX* and the brighter band of red fluorescence from Rh-LL-37 in the periplasm rise on the same time scale. This occurred within 30 min for 59 cells from three repeat experiments. We infer that oxidative species are formed gradually, as more and more monomeric Rh-LL-37 copies gain access to the periplasm.

In an important control experiment, in earlier work [20] we found that permeabilization of both the OM and the CM using Triton-X (without addition of AMP) did not enhance CellROX* fluorescence. This shows that CM permeabilization alone is not sufficient to trigger the signals of oxidative stress observed after LL-37 treatment.

No effect of the enantiomer *D*-LL-37 on CellROX* signal level. To test for the importance of LL-37 stereochemistry on the magnitude of oxidative effects, we repeated the CellROX* assay

in aerobic conditions using 4 μM of the all-*D* stereoisomer of LL-37. The average peak CellROX* signal level was the same within experimental error (**Figure 4.3B**). In addition, our earlier work found the same MIC for *D*- and *L*-LL-37 [19].

Attenuation of CellROX* response by pre-treatment with cyanide. Our working hypothesis is that in aerobic conditions, LL-37 causes formation of ROS (most likely $\bullet O_2^-$) in the periplasm by disrupting the electron transport chain. The disruption begins when LL-37 gains access to the periplasm, which also affords access to the outer leaflet of the CM. The electron transport chain employs a series of membrane proteins embedded in the CM [31]. For exponential growth in aerobic conditions, the primary pathway runs through the two NADH dehydrogenases NDH-I and NDH-II (with complex II dominant), passes through ubiquinone (UB), and terminates at the cytochrome oxidase-bo_3 complex [32]. Depending on the level of oxygenation, some fraction of the electron flux terminates at the alternative cytochrome oxidase-*bd* complex. The –*bd* complex has much higher affinity for O_2 than does –bo_3; its expression level increases with decreasing O_2 concentration in the growth medium. The terminal oxidase converts O_2 to H_2O, transferring protons to the periplasm and helping to maintain the proton motive force. At sufficient concentration, CN^- binds to the key heme iron in both the -bo_3 and the –*bd* complex, blocking O_2 binding, halting oxidative respiration and cell growth, and greatly diminishing the proton-motive force [21].

To test whether aerobic respiration is a prerequisite for LL-37-induced generation of the oxidative stress signals, we pre-incubated WT MG1655 *E. coli* cells with 1 mM KCN for 5 min prior to injection of 4 μM LL-37 in aerated growth medium. According to previous studies of reconstituted respiration *in vitro*, at this concentration the –bo_3 complex is strongly inhibited, but

the –*bd* complex is more weakly inhibited [33]. The inhibiting concentration *in vivo* is not known.

After pre-treatment for 5 min with cyanide, cells do not grow over a 50-min observation time, suggesting that respiration has been blocked. In two-color imaging experiments, we initiated flow of 4 μM LL-37 with 2.5 μM CellROX Green and 5 nM Sytox Orange at $t = 0$. The flow also contained 1 mM KCN to block respiration continuously. For the typical cell shown in **Appendix 4B**, no significant rise of CellROX* or Sytox Orange fluorescence was observed on a 50-min timescale. Evidently LL-37 induced neither ROS formation nor CM permeabilization. We measured the maximum CellROX* intensity from 62 cells in three separate experiments with and without pre-incubation with KCN (**Figure 4.3A**). The KCN pre-treatment attenuates the mean CellROX* fluorescence per cell by at least a factor of 5.

The KCN treatment also greatly reduces the fraction of cells that exhibit significant Sytox Orange fluorescence over 60 min of LL-37 treatment, from ~100% for normally growing cells to ~30% for KCN-treated cells (**Appendix 4B**). This suggests the possibility that formation of oxidative species, possibly ROS, within the periplasm may enhance the ability of LL-37 to permeabilize the CM. Alternatively, reduction of the transmembrane potential may inhibit the ability of LL-37 to permeabilize the CM, as discussed below.

The same pre-treatment of cells with KCN also reduces the cell-killing effects of LL-37. We repeated the LL-37 bactericidal assay after KCN treatment. As shown in **Appendix 4A**, more pre-treated cells survive after 4 μM LL-37 incubation for 30 min, and also for 1 hr. Evidently KCN pre-treatment provides some protection against the deleterious effects of LL-37. However,

when 8 μM LL-37 was applied to cells pre-treated with KCN, no growth was observed even after 1 hr.

In a similar vein, pre-treatment of the cells with the protonophore CCCP at 200 μM for 10 min completely halted growth. Subsequent injection of 4 μM of LL-37 and CellROX Green caused only a small, slowly rising CellROX* signal, again five times smaller than the peak signal from cells growing aerobically (**Figure 4.3A**).

Onset of resorufin fluorescence in aerobic conditions follows CM permeabilization. We tested for H_2O_2 induction in aerobic conditions by repeating the flow experiment using the MG1655 strain expressing the non-native peroxidase APEX2 from a plasmid [30]. At $t = 0$, we flowed 4 μM of LL-37 plus 10 μM Amplex Red and alternated phase contrast and red fluorescence images. Inside some 20% of 121 cells from three repeat experiments, a substantial burst of intracellular resorufin fluorescence is observed (example in **Figure 4.5A** and S4 Movie). However, for most cells we observe only a weak intracellular resorufin signal that is difficult to measure above a steadily increasing background of red fluorescence outside the cells (**Appendix 4C**). This strongly suggests that for most cells, resorufin formed in the cytoplasm efficiently escapes the cell envelope. As a result, the intracellular resorufin signal is usually very small.

To determine the exact timing of the onset of the strong, intracellular resorufin signals relative to CM permeabilization, we carried out two-color imaging experiments using Amplex Red and the green fluorescent DNA stain Sytox Green. In the minority of cells that exhibit appreciable intracellular resorufin fluorescence, the abrupt onset of red and green fluorescence is essentially simultaneous (**Figure 4.5B** and S5 Movie). Evidently the burst of resorufin is produced promptly after the CM is permeabilized. However, once again the majority of cells

show little or no intracellular resorufin signal. And once again a background of red fluorescence in the surround rises gradually over time, suggesting that while most or perhaps all cells are producing H_2O_2 in the cytoplasm, the resulting resorufin usually escapes the cell envelope efficiently (**Appendix 4C**). This makes sense; the OM is typically permeabilized to GFP and smaller species long before the CM is permeabilized to Sytox and other small molecules.

To summarize, the typical behavior in time of the CellROX* and resorufin fluorescence signal in aerobic conditions is very different. In most cells, CellROX* fluorescence rises gradually as LL-37 slowly gains entry to the periplasm (before CM permeabilization), and then decreases abruptly by a factor of two or more at the moment of CM permeabilization (**Figure 4.2**). In contrast, intracellular resorufin fluorescence rises abruptly at the moment of CM permeabilization (**Figure 4.5**). This is observed only in a minority of cells, but red background fluorescence rises gradually over the 30-min experiment.

Smaller signals of oxidative stress on cytochrome oxidase–*bd* deletion mutant strain. To test the possibility that LL-37 is causing release of oxidants by perturbing proper function of cytochrome oxidase-bo_3 or of cytochrome oxidase-*bd*, we carried out a limited number of microscopy experiments on the deletion mutant strains Δ*cyoABCDE* (–bo_3 deletion mutant) and Δ*cydAB* (–*bd* deletion mutant). The strains exhibit aerobic doubling times of 53 min and 45 min, respectively, similar to WT cells (**Table 4.2**). The 6-hr MICs are both 4 μM (**Table 4.2**), the same as the WT strain. The expression levels of the –bo_3 and –*bd* oxidases vary with the availability of O_2 in the medium. The –bo_3 oxidase, which binds O_2 more weakly, is more abundant when the level of dissolved O_2 is high [31]. The –*bd* oxidase, which binds O_2 more strongly, is more abundant for low O_2 concentrations.

As shown for the typical cell in **Appendix 4D**, in aerobic growth the Δ*cyoABCDE* mutant exhibited strong signals in the CellROX* after injection of LL-37 at 4 μM. The mean CellROX* signal level is slightly larger than for the WT strain (**Figure 4.3B**). The same mutant also showed strong resorufin signals in the Amplex Red assay, comparable to the signal shown in **Figure 4.5A** (**Appendix 4G**). However, the CellROX* signal level for the Δ*cydAB* mutant strain is only 27% that of the WT strain (**Figure 4.3B**). This result implicates cytochrome oxidase-*bd* in the mechanism by which LL-37 induces oxidative stress on accessing the periplasmic space.

Smaller signals of oxidative stress in growth under anaerobic fermentation conditions. No known terminal electron acceptors are present in the standard EZRDM medium. Cells growing in EZRDM with glucose as carbon source but without oxygen (Methods) and without added nitrate carry out fermentation, synthesizing ATP by glycolysis. The doubling time is essentially the same as in aerobic conditions (**Table 4.2**), and the pmf is likely reduced by about 25% [32]. At $t = 0$, we initiated flow of 2.5 μM CellROX Green and 4 μM unlabeled LL-37 (the aerobic MIC) over wild-type *E. coli* growing in fermentation conditions. The rate of cell growth, as judged by cell length in phase contrast images, decreased early on, much as it did in aerobic conditions. However, on the 30-min timescale, under anaerobic conditions 80% of 134 cells from three separate experiments continued to grow, albeit more slowly (example in **Figure 4.2C, D**). In comparison, on the same 30-min timescale under aerobic conditions only 40% of the cells continued to grow.

In these fermentation experiments with LL-37, a small green fluorescence signal, possibly due to CellROX*, was typically observed to rise slowly over 30 min as most cells continued to grow (**Figure 4.2C, D**). Averaged over 20 cells, the maximum green fluorescence intensity achieved during the 30-min observation period was three times smaller in fermentation than in

aerobic growth conditions (**Figure 4.3A**). There was no abrupt increase in green fluorescence. In contrast, the green signal in aerobic conditions rises more rapidly (over 5–10 min vs 30 min, **Figure 4.2B vs 2D**).

We repeated the one-color imaging experiments in fermentation conditions using 4 μM LL-37 along with either Sytox Green or CellROX Green. Over the first 30 min 20% of the 92 cells from three separate experiments exhibited cytoplasmic membrane permeabilization to Sytox Green (**Figure 4.1C**) and a halting of growth. Importantly, in the CellROX Green experiments no abrupt rise of CellROX* fluorescence was observed for any of the cells. We also repeated the Amplex Red/APEX2 experiments in fermentation conditions using 4 μM LL-37. For all 117 cells studied, we observed no significant resorufin fluorescence signal, either within the cells or in the extracellular background (example in **Figure 4.5A**).

We also carried out experiments at 16 μM LL-37 in fermentation conditions, a concentration equal to the 6-hr MIC. Under those conditions, all cells shrink within 30 min. A weak signal from CellROX* again rose gradually over 30 min, but there was no abrupt increase and the average maximum signal after 30 min was comparable to that at 4 μM LL-37 in fermentation conditions (**Figure 4.3A**).

To summarize, in fermentation conditions, the CM (and presumably the OM) of a subset of cells is permeabilized at 4 μM LL-37 and the CM of all cells is permeabilized at 16 μM LL-37. There is no evidence of the same type of rapidly rising CellROX* and resorufin signals of oxidative stress that were observed in aerobic growth.

Smaller signals of oxidative stress in growth under anaerobic respiration. Cells growing in EZRDM in the absence of oxygen but in the presence of glucose and added NO_3^- carry out

anaerobic respiration using the terminal reductase NarGHI, which reduces NO_3^- to NO_2^- [31]. To test whether a functional electron transport chain is sufficient to enable LL-37 to induce the CellROX* and resorufin signals, we carried out analogous fluorescence microscopy experiments on cells growing anaerobically in EZRDM supplemented with 10 mM KNO_3. In anaerobic respiration conditions, 4 μM LL-37 induced CM permeabilization to Sytox Green in a significantly smaller fractions of cells than in aerobic growth conditions, on both the 30-min and 60-min timescales (**Figure 4.1C**). This is congruent with the increase in MIC (**Table 4.2**). On average, the maximum CellROX* signal generated over 30 min was fivefold smaller than in the peak signal in aerobic growth (**Figure 4.3A**). No resorufin signal, either intracellular or extracellular, was observed from the Amplex Red assay in any of 49 cells studied. At 16 μM LL-37 (higher than the MIC of 12 μM under anaerobic respiration conditions), all cells exhibited cytoplasmic membrane permeabilization within 15 min. We carried out the Amplex Red assay at this higher LL-37 concentration and again observed no signal whatsoever in any of the 45 cells studied.

Magnitude of CellROX* signals for Melittin, Cecropin A, and Indolicidin

For *E. coli* in aerobic conditions, on addition of 10 μM melittin (twice the aerobic MIC) we observed a strong, rapidly rising CellROX* fluorescence signal (**Appendix 4E**). Much weaker, more slowly rising CellROX* fluorescence was observed (**Appendix 4E**) on addition of 0.9 μM cecropin A (1X the aerobic MIC) and of 32 μM indolicidin (1X the aerobic MIC). The average maximum intensity results are shown in the bar graph of **Figure 4.3B**. These data are congruent with a strong increase in MIC from aerobic to anaerobic (fermentation) conditions for melittin, but not for cecropin A nor for indolicidin.

Discussion

This work extends our earlier study of the attack of LL-37 on *E. coli* [19] to include direct observation of the timing of fluorescence signals that monitor oxidative stress. As shown before, the initial step in the attack is binding of the cationic LL-37 to the anionic lipopolysaccharide (LPS) layer, followed by permeabilization of the outer membrane (OM). For LL-37, we observed significant increases in MIC for cells growing under fermentation and anaerobic respiration conditions compared with aerobic respiration (**Tables 4.1 and 4.2**). In and of themselves, differences in MIC under different growth conditions should be interpreted cautiously. In addition to modulating oxidative stress effects, different growth conditions may also modulate the bacterial membrane composition. Such changes could alter the binding propensity of an AMP for the outer membrane and also the surface concentration of AMP required for membrane permeabilization.

The present work shows that for cells growing aerobically, an early green CellROX* signal gradually rises as the LL-37 concentration builds up in the periplasm, but before LL-37 has permeabilized the cytoplasmic membrane (CM) to the small dye Sytox Orange (**Figure 4.4**). Compared with the WT strain, the maximum CellROX* signal decreases almost 4-fold in the Δ*cydAB* deletion mutant but increases slightly (nominal 1.3-fold) in the Δ*cyoABCDE* deletion mutant. The signal is attenuated almost 6-fold after pre-treatment with KCN, which is known to inhibit aerobic respiration. The signal level was unchanged using the *D* stereoisomer form of LL-37. Entry of LL-37 into the periplasm gives the AMP access to the outer leaflet of the CM and to external surfaces of cytoplasmic membrane proteins.

These observations are consistent with a proposed mechanism in which LL-37 interferes with the terminal cytochrome oxidase-*bd*, causing inappropriate release of superoxide ($\bullet O_2^-$) into

the periplasmic space, where it oxidizes CellROX to CellROX* (**Figure 4.6**). Similarly, *in vitro* studies showed that the cyclic, cationic antimicrobial agent gramicidin S interfered with the activity of cytochrome oxidase-*bd*, but not with cytochrome oxidase-bo_3 [34]. The interference might arise from direct interaction of LL-37 with the oxidase. Observation of the same CellROX* signal level using the *L*- or *D*- enantiomer of LL-37 argues against existence of a specific binding pocket within the cytochrome oxidase-*bd* structure; it does not rule out a non-specific interaction due to electrostatic binding, for example. Alternatively, LL-37 may disrupt -*bd* function indirectly by perturbation of the membrane environment, perhaps by strong interaction of the polycationic peptide with anionic lipids such as cardiolipin (CL) or phosphatidylglycerol (PG) [35].

Importantly, we know from inadvertent experiments that use of old CellROX samples induces cytoplasmic fluorescence in *E. coli* even without addition of LL-37. Presumably CellROX had already been oxidized to the fluorescent form CellROX*. This makes it plausible that CellROX* created by LL-37 action in the periplasm is able to permeate the intact cytoplasmic membrane, bind to DNA, and fluoresce, prior to permeabilization of the CM to Sytox Orange or presumably to LL-37 itself.

The subsequent CM permeabilization event enables Sytox Orange and presumably LL-37 itself to enter the cytoplasm. CM permeabilization correlates in time with abrupt, partial quenching of the CellROX* fluorescence (by an unknown mechanism, **Figure 4.4A**) and the abrupt onset of resorufin fluorescence (**Figure 4.5B**), presumed to be formed by reaction of Amplex Red with APEX2 and H_2O_2. The resorufin signal is detected primarily outside the cells, but some 20% of cells retain substantial resorufin inside the cytoplasm. The detailed mechanism of H_2O_2 production is unclear. The most plausible source is dismutation of $\bullet O_2^-$ by the

superoxide dismutases (SODs) that reside in the cytoplasm. Once LL-37 has permeabilized the CM to Sytox Orange and to LL-37 itself, the $\bullet O_2^-$ formed in the periplasm may be able to cross the CM and reach the cytoplasm, where it finds SODs. Alternatively, if the CM becomes permeable to globular proteins, both the SODs and also APEX2 may pass from the cytoplasm to the periplasm, where they find $\bullet O_2^-$ and produce H_2O_2 (which itself is permeable). In addition, once LL-37 enters the cytoplasm it may induce formation of additional $\bullet O_2^-$ by some alternative mechanism.

Based on the properties of the dyes *in vitro*, we tentatively attribute the CellROX* signal that rises before CM permeabilization to production of superoxide ($\bullet O_2^-$) and the resorufin signal that rises after CM permeabilization to production of hydrogen peroxide (H_2O_2). However, enhancement of intracellular oxidants other than $\bullet O_2^-$ (or •OH) might cause conversion of CellROX Green to CellROX* [27]. The specificity of the APEX2 enzymatic reaction with H_2O_2 and Amplex Red to form resorufin lends support to the assumption that resorufin fluorescence is signaling an increase in hydrogen peroxide flux.

We found considerable evidence that aerobic respiration or a robust transmembrane potential or both are prerequisites for LL-37 to induce the early, gradually rising CellROX* signal and the delayed, abruptly rising resorufin signals (**Figures 4.2–4.5**). In **Figure 4.3** we compare the maximum CellROX* intensity observed over 30 min for various conditions. Both oxidative stress signals are greatly attenuated by pre-treatment of cells with cyanide (which blocks O_2 binding to the cytochrome oxidases, halts growth, and diminishes the pmf); by pre-treatment of cells with the protonophore CCCP (which abrogates the pmf); and by exclusion of oxygen from the medium, both in fermentation conditions (no operative electron transport chain)

and in anaerobic respiration using NO_3^- in the medium (enabling a different active electron transport chain).

It could be that the oxidants induced on entry of LL-37 to the periplasm enhance the ability of LL-37 to permeabilize the CM. Alternatively, the transmembrane electric field associated with the strong aerobic pmf points in the direction that would enhance the ability of a cationic peptide such as LL-37 to penetrate the low dielectric core of the bilayer and its substantial, repulsive dipole potential [36]. Such an effect was observed previously for cationic antibiotics such as gentamicin [37]. In anaerobic fermentation (**Figures. 4.1C, 4.2C, 4.2D and 4.5A**) and anaerobic respiration conditions (**Figure 4.1C**), the pmf is likely lower than in aerobic growth [24]. In those lower-pmf conditions, 4 μM LL-37 permeabilizes the CM and halts growth in a smaller fraction of cells. Even those permeabilized cells do not exhibit the type of CellROX* or resorufin signals characteristic of the rapid oxidative stress induced in aerobic conditions.

It is difficult to pinpoint exactly what aspects of the attack of LL-37 on *E. coli* cause the halting of growth and the eventual killing of cells. The smaller MIC in aerobic vs anaerobic growth conditions (**Table 4.1**) suggests that the observed oxidative stress events contribute, perhaps indirectly. Permeabilization of the CM to small species and concomitant loss of the pmf is undoubtedly an important factor as well. In a recent study of *E. coli* attacked by an analogue of the AMP PMAP-23, at killing concentrations the copy number of AMP per cell was estimated to be 10^6–10^7, and the assay was most sensitive to membrane-bound copies [38]. For the synthetic cationic peptide "ARVA", the analogous copy number was estimated to be $>10^8$ per cell [39]. Even at 10^6 per cell, the AMP concentration would be 1 mM. If LL-37 also binds to *E. coli* at such high concentrations, it is easy to imagine multiple harmful processes occurring in parallel.

The generality of oxidative stress induction by AMP action on bacteria deserves further exploration. As judged by the MIC in aerobic growth vs fermentation conditions (**Table 4.1**), the efficacy against *E. coli* of LL-37 and melittin depends on oxygen levels, while that of cecropin A and indolicidin does not. In previous work, we observed oxygen-sensitive MICs and time-dependent intra-cellular fluorescence signals indicative of oxidative stress during the attack on MG1655 *E. coli* by the synthetic AMP CM15 [20] and by the synthetic, highly cationic random β-peptide copolymer **MM_{63}:CHx_{37}** [22]. In the present work, the oxidative signals induced by LL-37 decreased significantly on deletion of cytochrome oxidase-*bd*, but not on deletion of the –bo_3 oxidase. This suggests a remarkably specific target of LL-37 activity. It seems likely that different AMPs will prove to induce oxidative stress by different mechanisms.

Finally, the enhancement of growth-halting effects of LL-37 in aerobic vs anaerobic conditions suggests the possibility that the degree of oxygenation in specific tissues may help to regulate AMP activity. For example, in the human gut the fraction of strict anaerobes increases from proximal to distal; in the colon, the oxygen partial pressure is only 25% of that in the atmosphere [23]. An earlier study of human β–defensin-1 found the AMP to be much more potent in its reduced, unfolded form against the pathogenic fungus *Candida albicans* and against anaerobic, Gram positive commensals of the *Bifidobacterium* and *Lactobacillus* species [23]. The effect was specific to certain microbial species. In contrast, human β-defensin-3, which is extremely potent in its oxidized, folded form, was less potent under reducing conditions. Like LL-37, hBD-3 is more potent in aerobic conditions. More work is needed, but it is already evident that the degree of oxygenation affects different human AMPs in different ways. Future work will test the generality of the induction of oxidative stress by other natural AMPs.

Acknowledgments

We thank Ms. Meghan Turner for the MIC measurement on indolicidin. The James Imlay lab generously provided an *E. coli* strain carrying the Δ*cydAB* deletion mutation, which we transferred to our background strain by P1 transduction.

Table 4.1 Antimicrobial peptides and their MICs for *E. coli* MG1655 in aerobic growth vs anaerobic fermentation in EZRDM at 30°C.

Antimicrobial Peptide	**Sequence**	**Net Charge**	**MIC (μM)** [1]	
			Aerobic	**Fermentation**
LL-37	**LLGDFFRKSKEKIGKEFK RIVQRIKDFLRNLVPRTES**	+6	4	16
Cecropin A	**KWKLFKKIEKVG QNIRDGIIKAGPAV AVVGQATQIAK-NH_2**	+7	0.9	0.9
Melittin	**GIGAVLKVLTTGL-PALISWIKRKRQQ-*NH_2***	+6	5	40
CM15	**KWKLFKKIGAVLKVL-NH_2**	+6	5	100
Indolicidin	**ILPWKWPWWPWRR-*NH_2***	+4	32	32

[1] MIC values were reproducible to the same factor of two in the dilution series for multiple repeats of the assay.

Table 4.2 Bacterial strains, with doubling times and MIC values for LL-37.[1]

Strain[2]	**Description**	**Growth Condition**	**Doubling Time (min)** [1]	**MIC (μM)** [1]
WT	MG1655	Aerobic	50 ± 3 [3,4]	4
JCW10	exports GFP to periplasm	Aerobic	51 ± 3 [3]	–
ZY01	expresses APEX2 from plasmid in MG1655	Aerobic	53 ± 3 [3]	–
Δ*cyoABCDE*	cytochrome oxidase-bo_3 deletion mutant of MG1655	Aerobic	53 ± 3 [3]	4
Δ*cydAB*	cytochrome oxidase-*bd-I* deletion mutant of MG1655	Aerobic	45 ± 3 [3]	4
ZY02	expresses APEX2 in Δ*cyoABCDE* strain	Aerobic	–	–
WT	MG1655	Anaerobic	53 ± 3 [4]	16
WT	MG1655	Anaerobic + 10 mM KNO_3	45 ± 3 [4]	12

[1] Doubling times and six-hour MIC values for LL-37 in EZRDM at 30°C. MIC values were reproducible to the same factor of two in the dilution series for multiple repeats of the assay. Doubling time precision is ±3 min, as judged from repeat experiments.

[2] See Methods for description of how strains were made.

[3] Determined in bulk cultures by OD measurements; see Methods.

[4] Determined by measuring cell length vs time using phase-contrast microscopy; see [18].

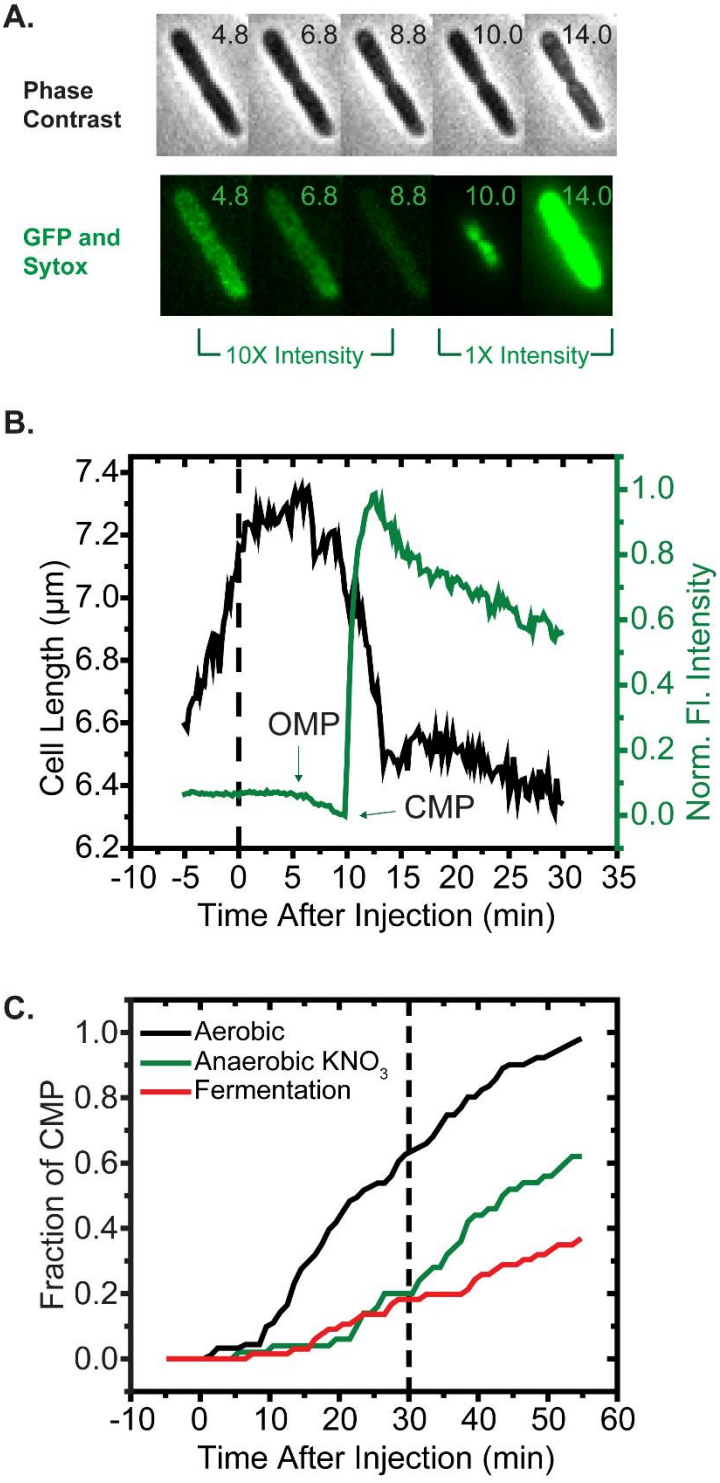

See next page for the figure legend

Figure 4.1 (A) Phase contrast and green fluorescence snapshots of single *E. coli* cell expressing periplasmic GFP in aerobic growth conditions, following addition of 4 μM LL-37 (the 6-hr aerobic MIC) with 5 nM Sytox Green. Times in minutes after injection of LL-37 at $t = 0$. (B) Time dependence of cell length (from phase contrast images) and total GFP and Sytox green fluorescence intensity for the cell shown in (A). Time of outer membrane permeabilization (OMP) and cytoplasmic membrane permeabilization (CMP) as shown. The initial decrease of fluorescence is due to loss of GFP from the periplasm to the surroundings. The subsequent burst of fluorescence is due to access of Sytox green to the cytoplasm upon CM permeabilization. (C) Cumulative distribution function (CDF) of the fraction of cells that have undergone CM permeabilization (onset of Sytox green fluorescence) vs time after the injection of 4 μM LL-37. Comparison for growth in aerobic respiration, anaerobic respiration using NO_3^-, and fermentation.

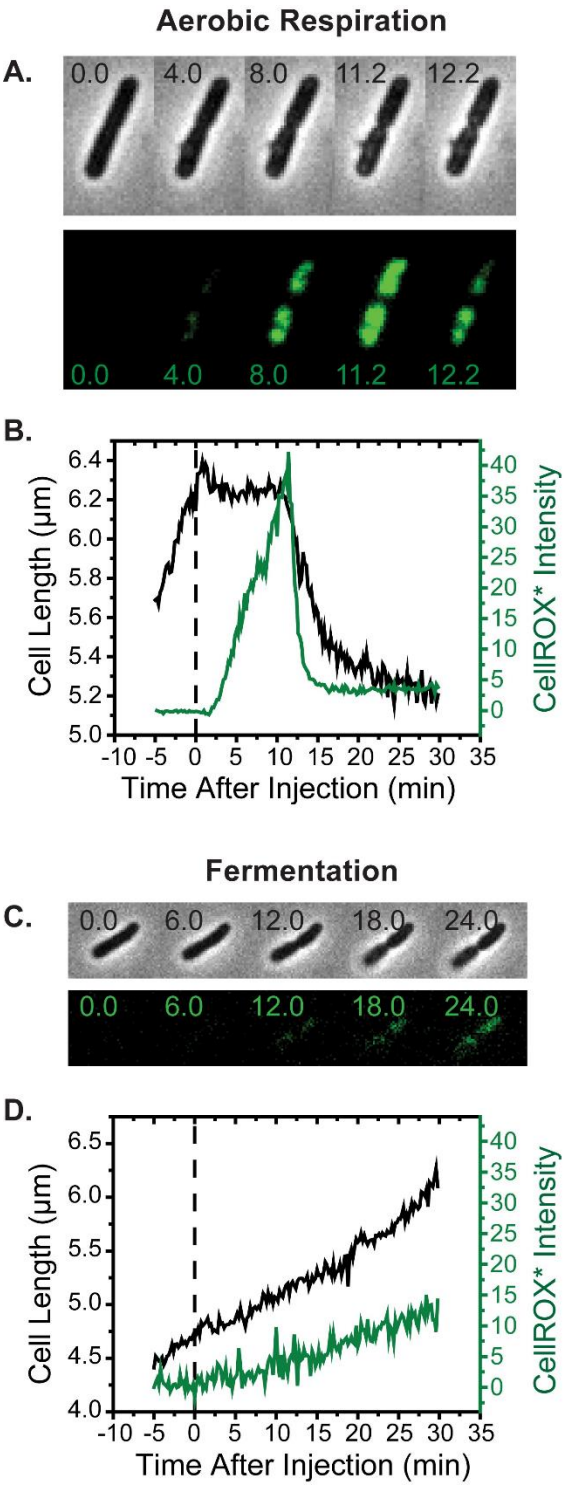

See next page for the figure legend

Figure 4.2 (A) Phase contrast and green fluorescence snapshots vs time after initiating flow at $t = 0$ of 4 μM LL-37 and 2.5 μM CellROX Green over MG1655 *E. coli* growing in aerobic conditions. Periplasmic GFP is not present. (B) Cell length and total CellROX* fluorescence intensity vs time for the cell shown in (A). (C and D) Same as panels (A and B), but cells are growing in anaerobic conditions under fermentation.

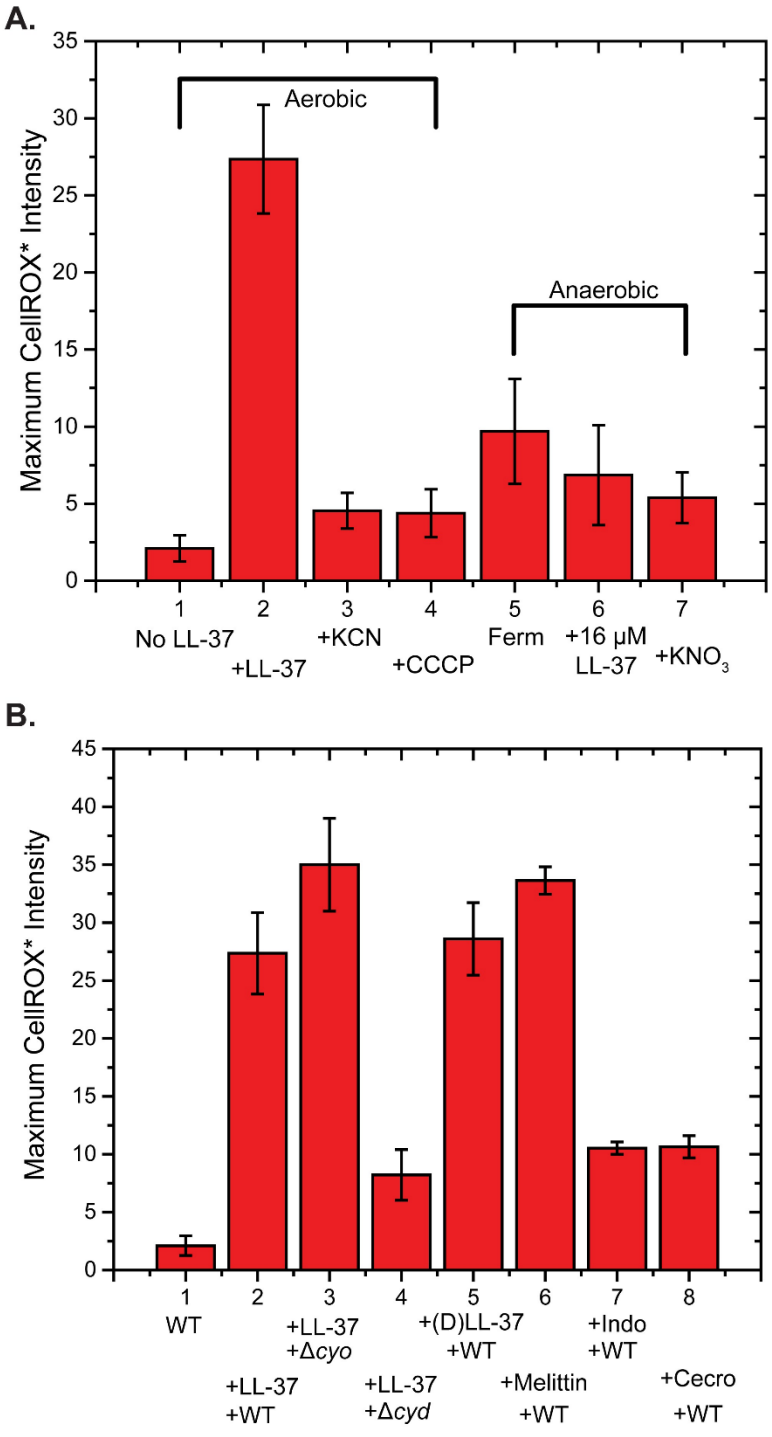

See next page for the figure legend

Figure 4.3 Comparison of average maximum CellROX* intensity over 30 min under different conditions. **(A)** (1) Normal aerobic growth (23 cells); no LL-37. (2) Addition of 4 μM LL-37 in aerobic conditions (58 cells). (3) Pre-treatment with KCN, followed by 4 μM LL-37 in aerobic conditions (62 cells). (4) Pre-treatment with CCCP, followed by 4 μM LL-37 in aerobic conditions (90 cells). (5) Addition of 4 μM LL-37 to cells growing in anaerobic, fermentation conditions (25 cells). (6) Addition of 16 μM LL-37 to cells growing in anaerobic, fermentation conditions (34 cells). (7) Addition of 4 μM LL-37 to cells growing in anaerobic conditions with respiration using NO_3^- (23 cells). In cases (2) and (6), the maximum intensity is that at the peak of the gradually rising and sharply falling signal, as in Figure 4.2B. In all other cases, the maximum is that of a slowly rising signal at t = 30 min, as in Figure 4.2D. **(B)** Comparison of average maximum CellROX* intensity over 30 min following addition of AMP as indicated. (1) Normal aerobic growth of WT MG1655 cells; no LL-37 (23 cells). (2) Addition of 4 μM LL-37 to WT MG1655 cells in aerobic growth (58 cells). (3) Addition of 4 μM LL-37 to Δ*cyoABCDE* MG1655 cells (cytochrome oxidase-bo_3 deletion strain) in aerobic growth (50 cells). (4) Addition of 4 μM LL-37 to Δ*cydAB* MG1655 cells (cytochrome oxidase-*bd* deletion strain) in aerobic growth (29 cells). (5) Addition of 4 μM of the enantiomer (*D*)LL-37 to WT MG1655 cells in aerobic growth. (30 cells) (6) Addition of 10 μM melittin to WT cells in aerobic growth (42 cells). (7) Addition of 32 μM indolicidin to WT cells in aerobic growth (42 cells). (8) Addition of 0.9 μM cecropin A to WT cells in aerobic growth (49 cells).

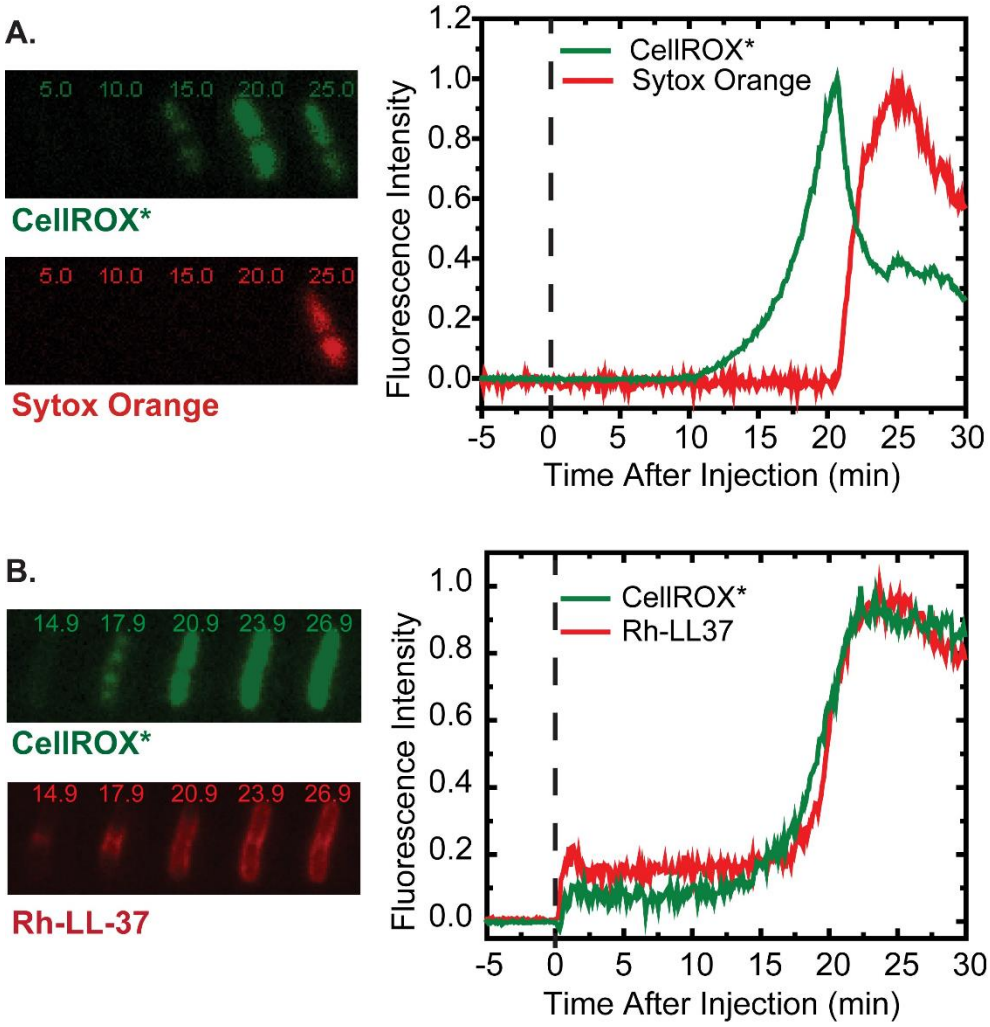

Figure 4.4 (A) Relative timing of CellROX* and Sytox Orange signals from two-color imaging. Aerobic growth conditions. *Left:* Snapshots of green and red fluorescence images of a single MG1655 cell after treatment with 4 μM LL37, 2.5 μM CellROX Green, and 5 nM Sytox Orange. Times in minutes after injection. Aerobic growth conditions. *Right:* CellROX* and Sytox Orange total fluorescence intensity vs time for cell shown at left. (B) Relative timing of CellROX* and Rh-LL-37 signals from two-color imaging. *Left:* Snapshots of green and red fluorescence images of a single MG1655 cell after treatment with 8 μM Rh-LL-37 plus 25 μM CellROX Green at $t = 0$. Times in minutes after injection. Aerobic conditions. *Right:* CellROX* and Rh-LL-37 total fluorescence intensity vs time for the cell shown at left.

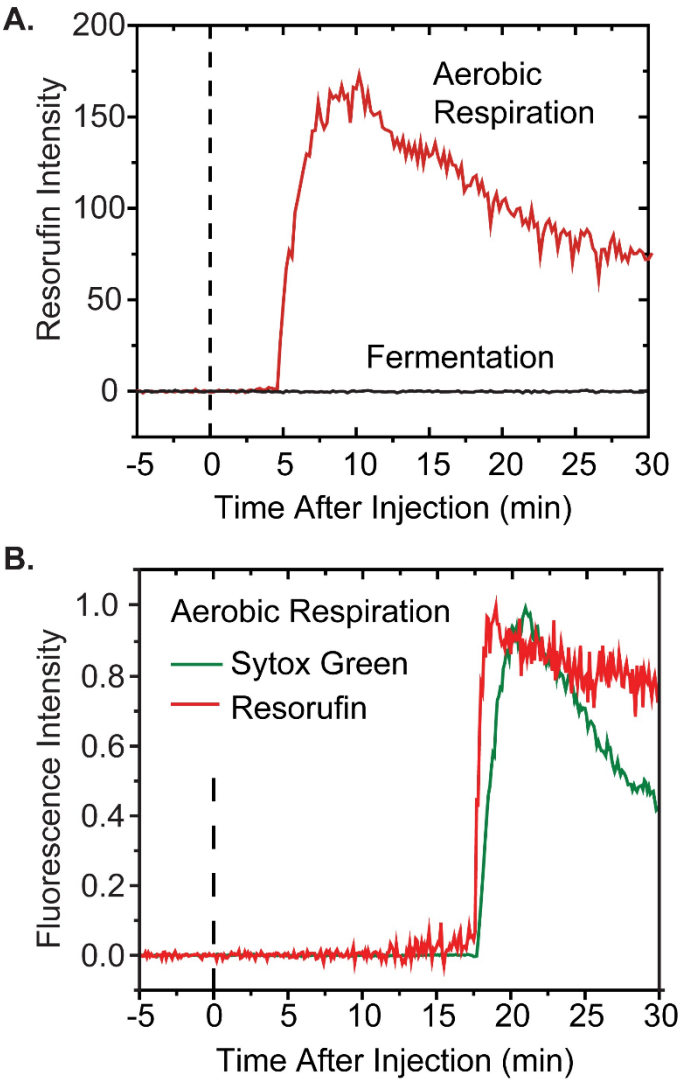

Figure 4.5 (A) Resorufin total fluorescence intensity vs time in aerobic growth and fermentation conditions. Flow of 4 μM LL-37 and 10 μM Amplex Red over MG1655 *E. coli* expressing the peroxidase APEX2 begins at $t = 0$. (B) Aerobic growth conditions. Relative timing of resorufin and Sytox Green signals from two-color imaging. Flow of 4 μM LL-37, 10 μM Amplex Red, and 5 nM Sytox Green over MG1655 *E. coli* expressing the peroxidase APEX2 begins at $t = 0$.

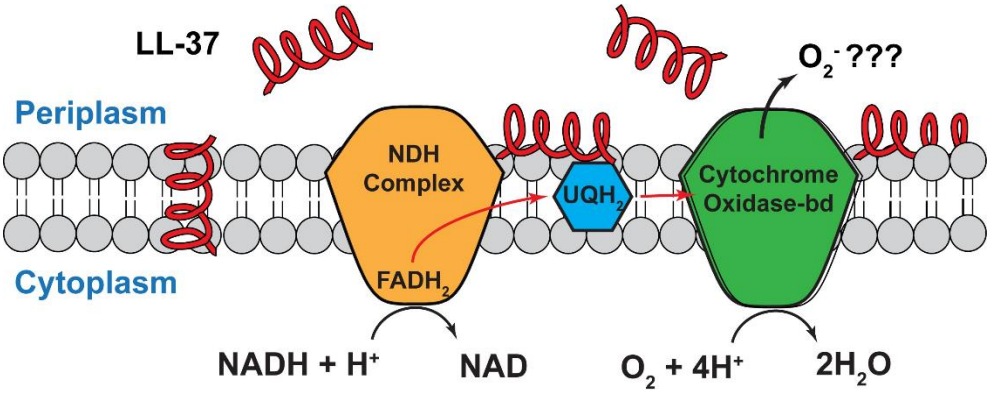

Figure 4.6 Schematic of the branch of the aerobic electron transport chain of *E. coli* terminating at cytochrome oxidase-*bd*. We suggest that LL-37 enters the periplasm, binds to the outer leaflet of the cytoplasmic membrane, and disrupts the proper activity of the terminal cytochrome oxidase-*bd* complex, releasing the intermediate superoxide (O_2^-) into the periplasm.

Appendix

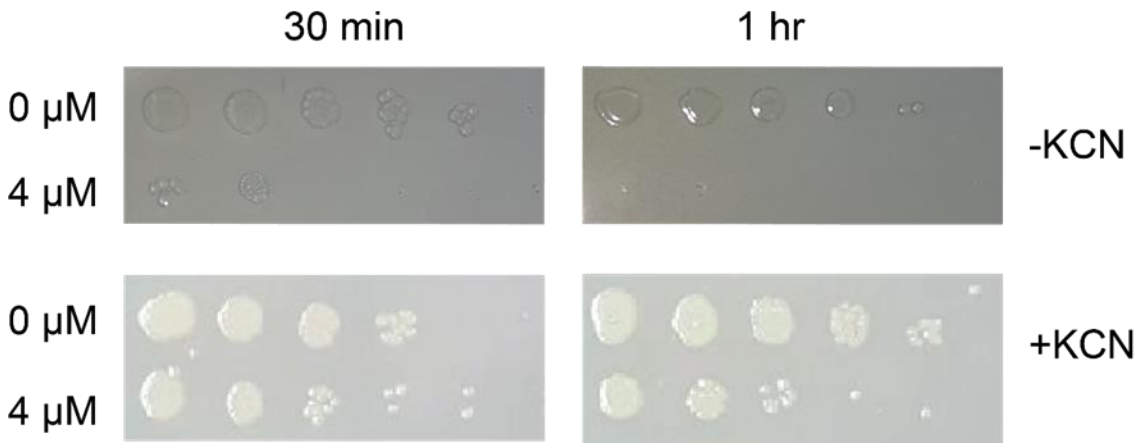

Appendix 4A. Bactericidal assay. Cultures growing aerobically in EZRDM at 30°C were pre-treated with 1 mM KCN for 5 min (+KCN) or not (–KCN) and incubated with LL-37 at 0 or 4 μM (1X the aerobic MIC) for 30 min (left) or 1 hr (right). The cultures were then sampled and diluted before spotting onto LB plates for overnight incubation at 30°C. From left to right in each panel, serial dilutions led to addition of 5×10^6, 5×10^5, 5×10^4, 5×10^3, 5×10^2, and 5 cells/mL onto the LB plate. Colonies were photographed the next morning. There is a higher cell survival rate for 30-min LL-37 treatment than for 60-min and after KCN pre-treatment than without KCN pre-treatment.

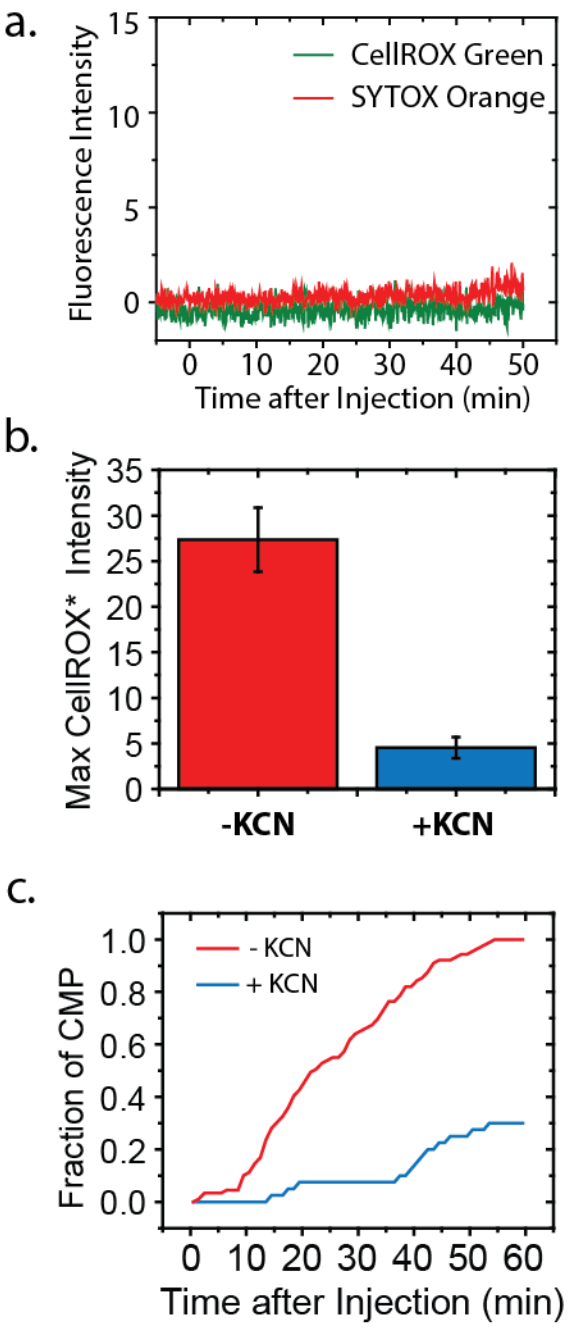

See next page for the figure legend.

Appendix 4B. Effects of 4 μM LL-37 (the 6-hr aerobic MIC) on MG1655 *E. coli* pretreated with 1 mM KCN for 5 min. a) Example of CellROX* and Sytox Orange fluorescence intensity vs time after the injection of LL-37. b) Comparison of mean, single-cell CellROX* peak fluorescence intensity without and with KCN pre-treatment. Error bars are ±1 SD of the mean. c**)** Cumulative distribution function for cells that undergo cytoplasmic membrane permeabilization (CMP) after the injection of 4 μM LL-37 without (90 cells) and with (60 cells) KCN pre-treatment, as judged by Sytox Orange fluorescence.

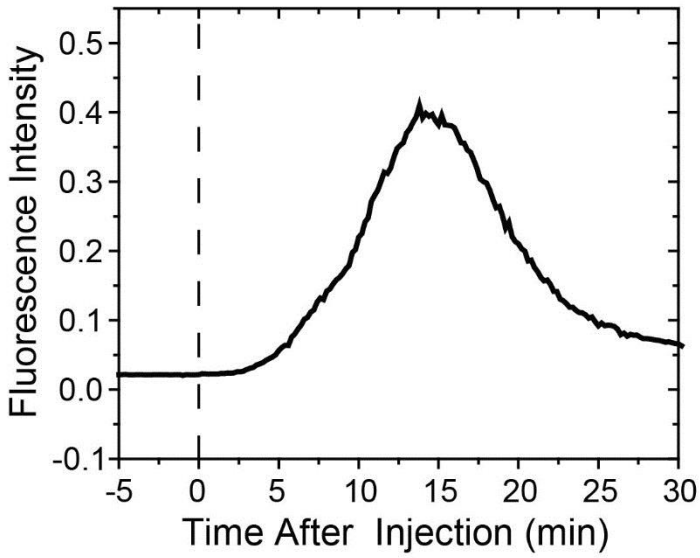

Appendix 4C. Time dependence of background fluorescence (outside of any cells) from resorufin after injection at $t = 0$ of 4 μM LL-37 plus 10 μM Amplex Red across cells expressing APEX2 and growing aerobically.

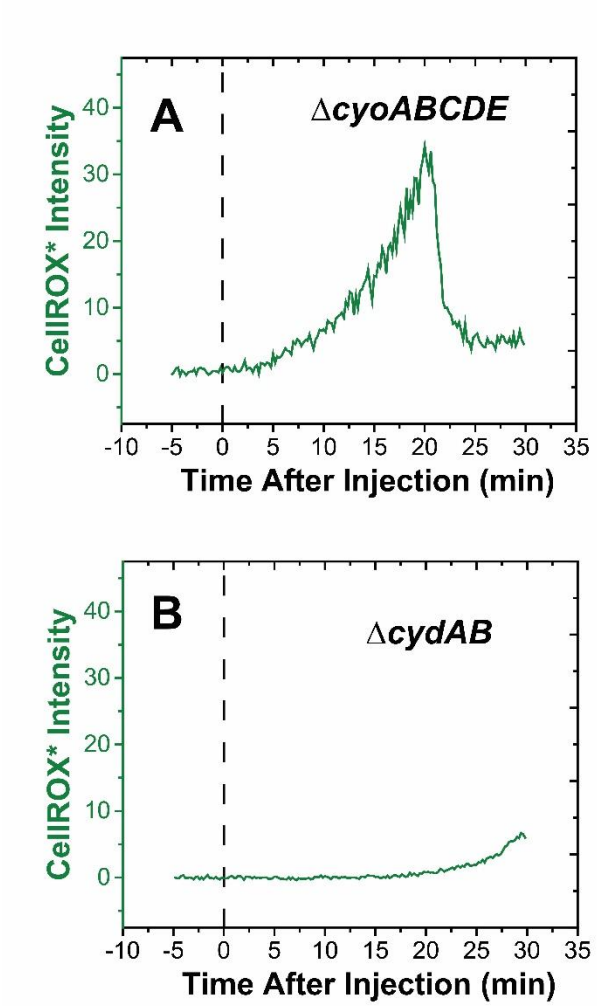

Appendix 4D. (A) CellROX* total fluorescence intensity vs time within a single, representative Δ*cyo-ABCDE* cell. Flow of 4 μM LL-37 and 2.5 μM CellROX Green begins at $t = 0$. (B) CellROX* total fluorescence intensity vs time within a single, representative Δ*cyd-AB* cell. Flow of 4 μM LL-37 and 2.5 μM CellROX Green begins at $t = 0$. Both signals are taken under identical laser and imaging conditions, so that quantitative comparison of signal amplitudes is appropriate. See Figure 4.3B for comparison of the mean of the peak CellROX* signal for WT, Δ*cyo-ABCDE*, and Δ*cyd-AB* strains.

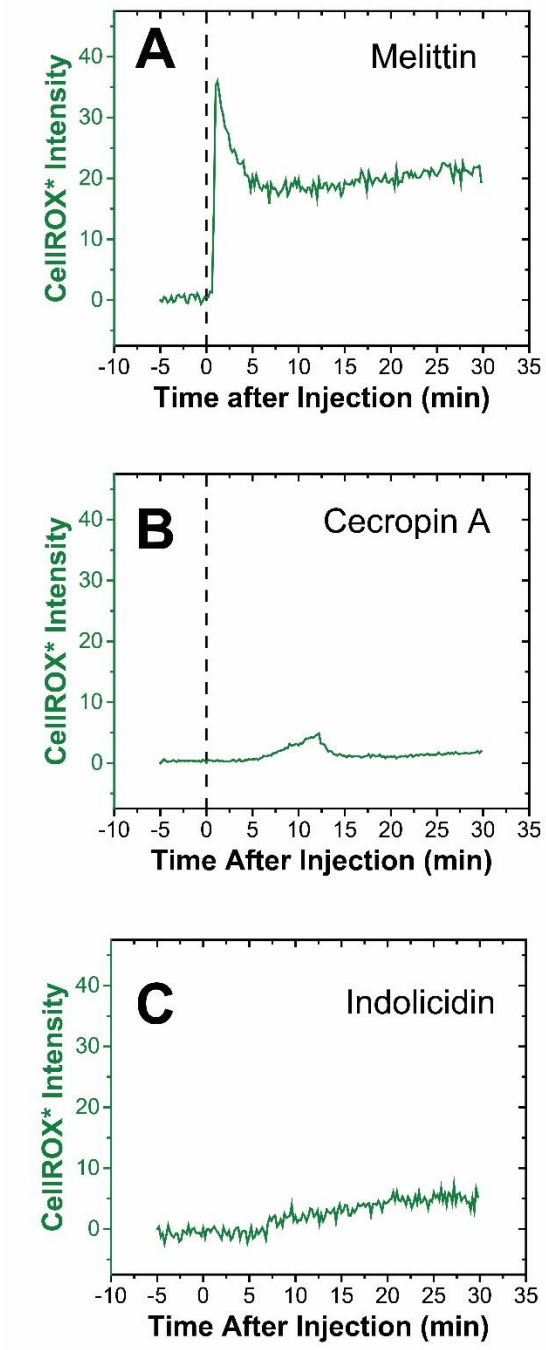

See next page for the figure legend.

Appendix 4E. CellROX* total fluorescence intensity vs time within single, representative WT cells for three additional AMPs. Flow of each AMP and 2.5 μM CellROX Green begins at $t = 0$. All three signals are taken under identical laser and imaging conditions, so that quantitative comparisons of signal amplitudes are appropriate. (A) 10 μM melittin (twice the aerobic MIC). (B) 0.9 μM cecropin A (1X the aerobic MIC). (C) 32 μM indolicidin (1X the aerobic MIC). See Figure 4.3B for comparison of the mean of the peak CellROX* signals for LL-37, melittin, cecropin A, and indolicidin.

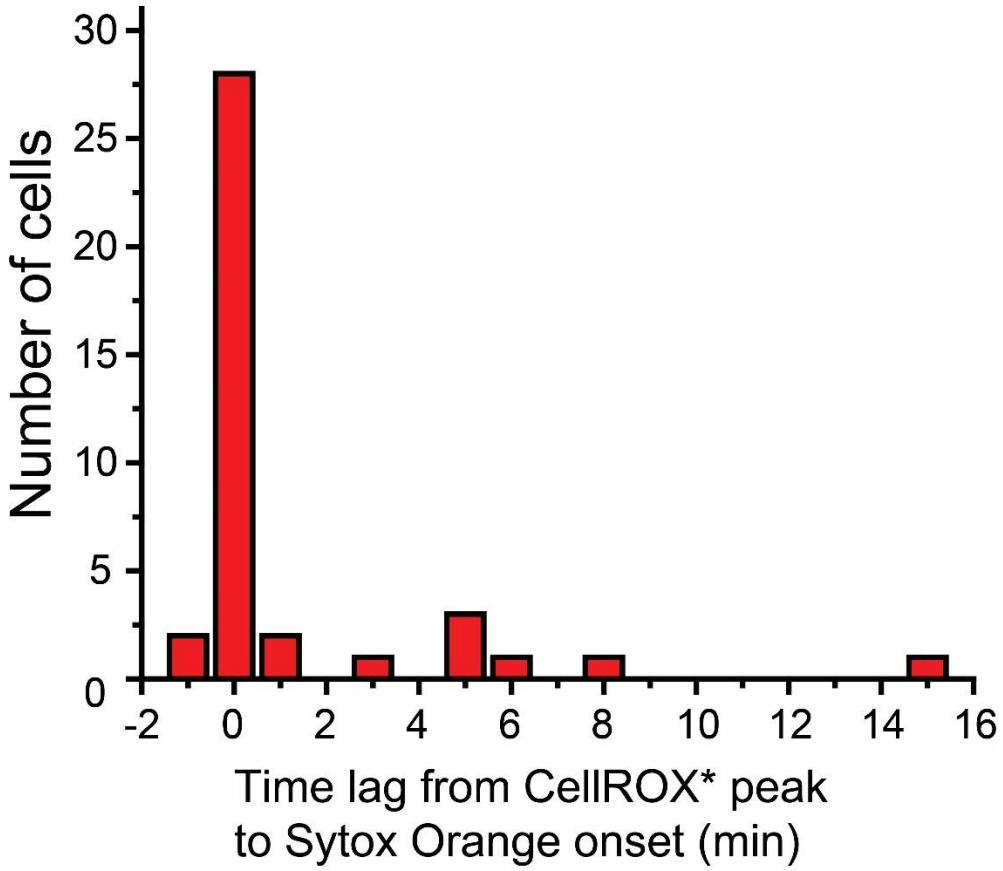

Appendix 4F. Histogram of time lags between the peak of the CellROX* signal and the abrupt onset of the Sytox Orange signal. Addition of 4 μM LL-37, 2.5 μM CellROX Green, and 5 nM Sytox Orange were injected across plated cells growing aerobically. The time between the peak CellROX* signal and the onset of Sytox Orange fluorescence was measured, as shown in Figure 4.4A. Most often, the two events coincided in time within 1 min.

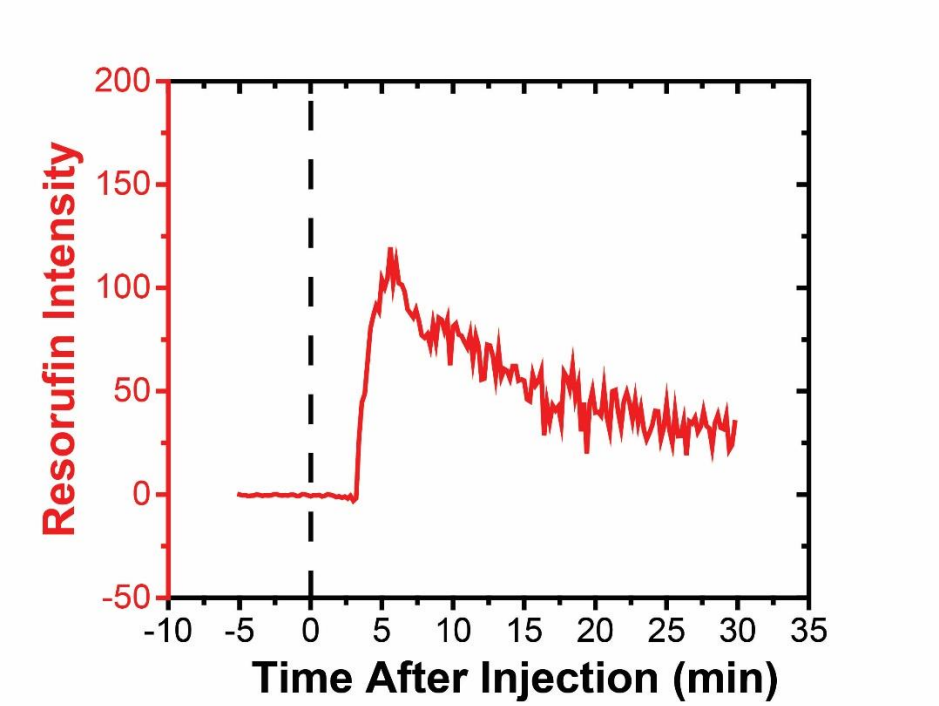

Appendix 4G. Example of single-cell resorufin fluorescence vs time from the Amplex Red assay carried out in aerobic growth using the Δ*cyoABCDE* mutant strain. Injection of 4 μM LL-37 begins at $t = 0$.

References

1. Hilchie AL, Wuerth K, Hancock RE. Immune modulation by multifaceted cationic host defense (antimicrobial) peptides. Nat Chem Biol. 2013;9(12):761-8.

2. Wang G, Mishra B, Lau K, Lushnikova T, Golla R, Wang X. Antimicrobial peptides in 2014. Pharmaceuticals (Basel). 2015;8(1):123-50.

3. Flannagan RS, Cosio G, Grinstein S. Antimicrobial mechanisms of phagocytes and bacterial evasion strategies. Nat Rev Microbiol. 2009;7(5):355-66.

4. Ganz T. The role of antimicrobial peptides in innate immunity. Integr Comp Biol. 2003;43(2):300-4.

5. Moller J, Luhmann T, Chabria M, Hall H, Vogel V. Macrophages lift off surface-bound bacteria using a filopodium-lamellipodium hook-and-shovel mechanism. Sci Rep. 2013;3:2884.

6. Hampton MB, Kettle AJ, Winterbourn CC. Inside the neutrophil phagosome: oxidants, myeloperoxidase, and bacterial killing. Blood. 1998;92(9):3007-17.

7. Slauch JM. How does the oxidative burst of macrophages kill bacteria? Still an open question. Mol Microbiol. 2011;80(3):580-3.

8. Soehnlein O, Kai-Larsen Y, Frithiof R, Sorensen OE, Kenne E, Scharffetter-Kochanek K, et al. Neutrophil primary granule proteins HBP and HNP1-3 boost bacterial phagocytosis by human and murine macrophages. J Clin Invest. 2008;118(10):3491-502.

9. Chen X, Takai T, Xie Y, Niyonsaba F, Okumura K, Ogawa H. Human antimicrobial peptide LL-37 modulates proinflammatory responses induced by cytokine milieus and double-stranded RNA in human keratinocytes. Biochem Biophys Res Commun. 2013;433(4):532-7.

10. Pag U, Sahl HG. Multiple activities in lantibiotics--models for the design of novel antibiotics? Curr Pharm Des. 2002;8(9):815-33.

11. Hechard Y, Sahl HG. Mode of action of modified and unmodified bacteriocins from Gram-positive bacteria. Biochimie. 2002;84(5-6):545-57.

12. Wilmes M, Cammue BP, Sahl HG, Thevissen K. Antibiotic activities of host defense peptides: more to it than lipid bilayer perturbation. Nat Prod Rep. 2011;28(8):1350-8.

13. Brogden KA. Antimicrobial peptides: pore formers or metabolic inhibitors in bacteria? Nat Rev Microbiol. 2005;3(3):238-50.

14. Afacan NJ, Yeung AT, Pena OM, Hancock RE. Therapeutic potential of host defense peptides in antibiotic-resistant infections. Curr Pharm Des. 2012;18(6):807-19.

15. Barns KJ, Weisshaar JC. Single-cell, time-resolved study of the effects of the antimicrobial peptide alamethicin on *Bacillus subtilis*. Biochim Biophys Acta. 2016;1858(4):725-32.

16. Choi H, Rangarajan N, Weisshaar JC. Lights, Camera, Action! Antimicrobial Peptide Mechanisms Imaged in Space and Time. Trends Microbiol. 2016;24(2):111-22.

17. Rangarajan N, Bakshi S, Weisshaar JC. Localized permeabilization of *E. coli* membranes by the antimicrobial peptide Cecropin A. Biochemistry. 2013;52(38):6584-94.

18. Barns KJ, Weisshaar JC. Real-time attack of LL-37 on single *Bacillus subtilis* cells. Biochim Biophys Acta. 2013;1828(6):1511-20.

19. Sochacki KA, Barns KJ, Bucki R, Weisshaar JC. Real-time attack on single *Escherichia coli* cells by the human antimicrobial peptide LL-37. Proc Natl Acad Sci U S A. 2011;108(16):E77-81.

20. Choi H, Yang Z, Weisshaar JC. Single-cell, real-time detection of oxidative stress induced in *Escherichia coli* by the antimicrobial peptide CM15. Proc Natl Acad Sci U S A. 2015;112(3):E303-10.

21. Imlay JA. The molecular mechanisms and physiological consequences of oxidative stress: lessons from a model bacterium. Nat Rev Microbiol. 2013;11(7):443-54.

22. Choi H, Chakraborty S, Liu R, Gellman SH, Weisshaar JC. Single-Cell, Time-Resolved Antimicrobial Effects of a Highly Cationic, Random Nylon-3 Copolymer on Live *Escherichia coli*. ACS Chem Biol. 2016;11(1):113-20.

23. Schroeder BO, Wu Z, Nuding S, Groscurth S, Marcinowski M, Beisner J, et al. Reduction of disulphide bonds unmasks potent antimicrobial activity of human beta-defensin 1. Nature. 2011;469(7330):419-23.

24. Tran QH, Unden G. Changes in the proton potential and the cellular energetics of *Escherichia coli* during growth by aerobic and anaerobic respiration or by fermentation. Eur J Biochem. 1998;251(1-2):538-43.

25. Sargent F. The twin-arginine transport system: moving folded proteins across membranes. Biochem Soc Trans. 2007;35(Pt 5):835-47.

26. Sochacki KA, Shkel IA, Record MT, Weisshaar JC. Protein diffusion in the periplasm of *E. coli* under osmotic stress. Biophys J. 2011;100(1):22-31.

27. Imlay JA. Diagnosing oxidative stress in bacteria: not as easy as you might think. Curr Opin Microbiol. 2015;24:124-31.

28. Kalyanaraman B, Darley-Usmar V, Davies KJ, Dennery PA, Forman HJ, Grisham MB, et al. Measuring reactive oxygen and nitrogen species with fluorescent probes: challenges and limitations. Free Radic Biol Med. 2012;52(1):1-6.

29. Dwyer DJ, Belenky PA, Yang JH, MacDonald IC, Martell JD, Takahashi N, et al. Antibiotics induce redox-related physiological alterations as part of their lethality. Proc Natl Acad Sci U S A. 2014;111(20):E2100-9.

30. Martell JD, Deerinck TJ, Sancak Y, Poulos TL, Mootha VK, Sosinsky GE, et al. Engineered ascorbate peroxidase as a genetically encoded reporter for electron microscopy. Nat Biotechnol. 2012;30(11):1143-8.

31. Unden G, Steinmetz PA, Degreif-Dunnwald P. The Aerobic and Anaerobic Respiratory Chain of *Escherichia coli* and *Salmonella* enterica: Enzymes and Energetics. EcoSal Plus. 2014;6(1).

32. Unden G, Bongaerts J. Alternative respiratory pathways of *Escherichia coli*: Energetics and transcriptional regulation in response to electron acceptors. Biochim Biophys Acta-Bioenergetics. 1997;1320(3):217-34.

33. Kita K, Konishi K, Anraku Y. Terminal oxidases of *Escherichia coli* aerobic respiratory chain. II. Purification and properties of cytochrome b558-d complex from cells grown with limited oxygen and evidence of branched electron-carrying systems. J Biol Chem. 1984;259(5):3375-81.

34. Mogi T, Ui H, Shiomi K, Omura S, Kita K. Gramicidin S identified as a potent inhibitor for cytochrome bd-type quinol oxidase. FEBS Lett. 2008;582(15):2299-302.

35. Oliver PM, Crooks JA, Leidl M, Yoon EJ, Saghatelian A, Weibel DB. Localization of anionic phospholipids in *Escherichia coli* cells. J Bacteriol. 2014;196(19):3386-98.

36. Wang L. Measurements and implications of the membrane dipole potential. Annu Rev Biochem. 2012;81:615-35.

37. Eisenberg ES, Mandel LJ, Kaback HR, Miller MH. Quantitative association between electrical potential across the cytoplasmic membrane and early gentamicin uptake and killing in *Staphylococcus aureus*. J Bacteriol. 1984;157(3):863-7.

38. Roversi D, Luca V, Aureli S, Park Y, Mangoni ML, Stella L. How many antimicrobial peptide molecules kill a bacterium? The case of PMAP-23. ACS Chem Biol. 2014;9(9):2003-7.

39. Starr CG, He J, Wimley WC. Host Cell Interactions Are a Significant Barrier to the Clinical Utility of Peptide Antibiotics. ACS Chem Biol. 2016;11(12):3391-9.

40. Choi H, Chakraborty S, Liu R, Gellman SH, Weisshaar JC. Medium effects on minimum inhibitory concentrations of nylon-3 polymers against *E. coli*. PLoS One. 2014;9(8):e104500.

41. Aitken CE, Marshall RA, Puglisi JD. An oxygen scavenging system for improvement of dye stability in single-molecule fluorescence experiments. Biophysical Journal. 2008;94(5):1826-35.

Chapter 5

Future Directions

My thesis work explores the actions of antimicrobial peptides (AMPs) on single, live *E. coli* cells primarily from the standpoint of membrane permeabilization and reactive oxygen species (ROS) formation. Now we have a clearer picture of AMP mechanisms. For example, membrane permeabilization and membrane re-sealing seem to be a common mechanism for a variety of AMPs. Outer membrane is permeabilized at least to small molecules before short AMPs or nylon-3-copolymers permeabilize the cytoplasmic membrane of *E. coli*. Activities of some AMPs are regulated by O_2, possibly linked to ROS formation. Still, some additional interesting questions can also be addressed by implementing our assays.

Combination effects of AMPs and AMP & antibiotics

Our current single-cell, time-lapse fluorescence microscope studies have been focusing on studying one AMP at a time on *E. coli* cells. However, a combination of different AMPs or of AMP plus antibiotics seems to display better potential in the clinical application, mainly due to the high cost of AMPs. Therefore, understanding the mechanisms behind the combination effects is important to guide the development of efficient and economical AMP-based therapies of antibiotic-resistant infections.

When drugs are combined, the effects can be either stronger (synergism), the same (additivity), or weaker (antagonism). Various methods have been developed to predict and evaluate the efficacy of drug combinations. Synergism seems to be a common phenomenon in AMPs interaction and three-AMP combinations exhibit stronger synergism than two-AMP interaction[1]. For example, PGLa and Magainin-2 which are co-expressed AMPs on frog's skin, are synergistic when applied to both *E. coli* and tumor cells[2]. This finding is very exciting. If

human innate AMPs are synergistic with AMP-based drugs or conventional antibiotics, it will further reduce the drug dosage and side effects.

In contrast, the combination effects of AMP & antibiotics seem to be random, though researchers initially thought that potent membrane disruption activity by AMPs would enhance the uptake of antibiotics and increase their antibacterial effects[3-5]. For example, magainin II was demonstrated to be synergistic with ceftriaxone, amoxicillin clavulanate and β-lactam antibiotics. However, buforin II, cecropin P1 and indolicidin only demonstrated additivity with the antibiotics[6]. Thankfully, antagonistic effect is rare.

Even though combination of AMPs and AMP plus antibiotics has been studied somewhat, the experimental studies are largely restricted to comparing minimum inhibitory concentrations and bacterial killing curves. The mechanisms behind the combination effects remain obscure. Therefore, I propose to bring the study to the single-cell, time-lapse level by applying the membrane permeabilization assays and ROS assays described in my thesis work. Combination of AMPs might stabilize the membrane pores and allow faster translocation of AMP partners inhibiting intracellular targets. Some antibiotics might inhibit the intracellular activities, which are targets of some AMPs. It was revealed that arrested cellular respiration by the bacteriostatic antibiotic blocks the bactericidal killing, possibly by decreasing ROS resources of the bactericidal antibiotic[7]. A similar hypothesis may apply to the combination effect of AMP and antibiotics, as we already know from Chapter 4 that ROS also contribute to the antimicrobial activity of some AMPs.

Membrane permeabilization effects of AMPs under anaerobic condition

In our 2015 work, we noticed that CM15 attacks membranes of *E. coli* differently between aerobic condition and anaerobic condition[8]. At anaerobic condition, about 25% of the cells showed behavior similar to that in aerobic conditions. Periplasmic GFP first migrated to the cytoplasm, followed by complete loss of GFP from the outer membrane much later. Others exhibit symptoms such as membrane blebbing, complete loss of GFP signal as the initial event, and GFP bubble formation. In 2017 work, we observed a significant decrease of cytoplasmic membrane permeabilization when LL-37 attacks *E. coli* switching from aerobic condition to anaerobic condition[9]. However, the activities of outer membrane permeabilization by AMPs is unknown in the anaerobic condition, especially to small molecules. Therefore, I propose to apply the HaloTag-based membrane permeabilization assay developed in Chapter 3 to probe events induced by AMPs on membranes of *E. coli* under anaerobic condition. It is worth noting that the HaloTag fluorescence does not depend on O_2, contrasting to fluorescent proteins.

Finally, I would like to propose to exploit advanced microfluidics systems with more channels, cameras with bigger chips and fluorescence microscope equipped with automated stage, to enlarge the observation field and enhance information about AMPs actions on bacteria cells.

References

1. Yu, G.; Baeder, D. Y.; Regoes, R. R.; Rolff, J., Combination Effects of Antimicrobial Peptides. *Antimicrob Agents Chemother* **2016,** *60* (3), 1717-24.

2. Westerhoff Hans, V.; Zasloff, M.; Rosner, J. L.; Hendler Richard, W.; Waal, A.; Gomes Ana, V.; Jongsma Ans, P. M.; Riethorst, A.; Juretić, D., Functional Synergism of the Magainins PGLa and Magainin‐2 in *Escherichia coli*, Tumor Cells and Liposomes. *European Journal of Biochemistry* **1995,** *228* (2), 257-264.

3. He, J.; Starr, C. G.; Wimley, W. C., A lack of synergy between membrane-permeabilizing cationic antimicrobial peptides and conventional antibiotics. *Biochim Biophys Acta* **2015,** *1848* (1 Pt A), 8-15.

4. Feng, Q.; Huang, Y.; Chen, M.; Li, G.; Chen, Y., Functional synergy of α-helical antimicrobial peptides and traditional antibiotics against Gram-negative and Gram-positive bacteria in vitro and in vivo. *European Journal of Clinical Microbiology & Infectious Diseases* **2015,** *34* (1), 197-204.

5. Al-Ani, I.; Zimmermann, S.; Reichling, J.; Wink, M., Pharmacological synergism of bee venom and melittin with antibiotics and plant secondary metabolites against multi-drug resistant microbial pathogens. *Phytomedicine* **2015,** *22* (2), 245-55.

6. Zhou, Y.; Peng, Y., Synergistic effect of clinically used antibiotics and peptide antibiotics against Gram-positive and Gram-negative bacteria. *Exp Ther Med* **2013,** *6* (4), 1000-1004.

7. Lobritz, M. A.; Belenky, P.; Porter, C. B.; Gutierrez, A.; Yang, J. H.; Schwarz, E. G.; Dwyer, D. J.; Khalil, A. S.; Collins, J. J., Antibiotic efficacy is linked to bacterial cellular respiration. *Proc Natl Acad Sci U S A* **2015,** *112* (27), 8173-80.

8. Choi, H.; Yang, Z.; Weisshaar, J. C., Single-cell, real-time detection of oxidative stress induced in *Escherichia coli* by the antimicrobial peptide CM15. *Proc Natl Acad Sci U S A* **2015,** *112* (3), E303-10.

9. Choi, H.; Yang, Z.; Weisshaar, J. C., Oxidative stress induced in *E. coli* by the human antimicrobial peptide LL-37. *PLoS Pathog* **2017,** *13* (6), e1006481.

Chapter 6

Track antimicrobial peptides actions on single *E. coli* cells under the microscope

Prepared for the WISL Award for Communicating Graduate Chemistry Research to the Public. Thanks to Professor Bassam Z. Shakhashiri for the event initiation and organization. Many credits to Professor Bassam Z. Shakhashiri, editor and Cayce J. Osborne for the comments.

Q1: Can you briefly describe your research?

I use a fluorescence microscope (a microscope that uses fluorescence to generate an image) to track responses of individual *E. coli* (a common bacterium, refer to Q4 for more information) cells upon exposure to antimicrobial peptides (a special type of antibiotics, defined in Q2). In the example below, the green color represents a kind of protein which fluoresces green after exposure to a laser. Darker green contains more green fluorescent protein. At the beginning, the four cells all contain some green fluorescent protein. However, their experiences upon attack by antimicrobial peptides are completely different. For example, some cells become longer initially but shorter later, partially losing green fluorescent protein. Some cells die immediately and become shorter and lose green fluorescent protein completely.

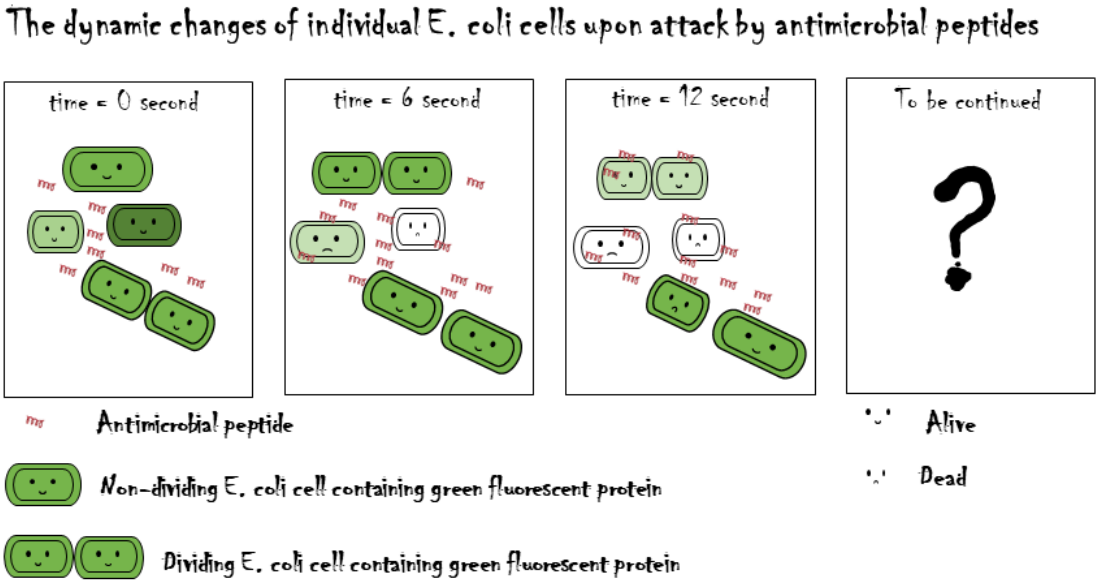

Q2: What are antimicrobial peptides and where do they come from?

Antimicrobial peptides are relatively small peptides (peptides are compounds consisting of two or more amino acids linked in a chain) that protect a host from bacterial infection, by either modulating host immunity or killing bacterial cells. Antimicrobial peptides act on bacterial cells in many ways. For example, they can disrupt bacterial membranes, resulting in leakage from the cell, or they can mess up bacterial intracellular metabolism activities. All these actions can lead bacterial cells to stop growing or even die.

Antimicrobial peptides can be found nearly everywhere in nature. For example, the antimicrobial peptides studied in my thesis work include LL-37 that is found under our skin, Melittin originating from bee venom, and Indolicidin coming from cows. These antimicrobial peptides all have different structures and conformations. So far, almost 3000 natural antimicrobial peptides have been discovered.

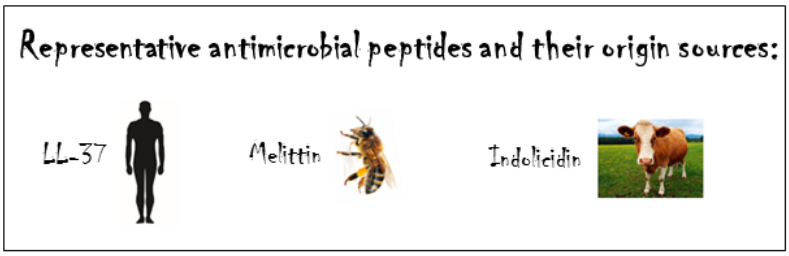

Q3: What is the significance of studying antimicrobial peptides?

A healthy body keeps good bacteria but not harmful bacteria. If we have either a low level of good bacteria or a high level of harmful bacteria, we are likely to suffer from many chronic inflammatory diseases, such as asthma, cancer, and stroke. Studies have shown that antimicrobial peptides contribute to the proper maintenance of microorganisms in our bodies.

Exploring the actions of antimicrobial peptides on bacterial cells can help us understand why we are able to but sometimes fail to maintain the appropriate level of good bacteria and harmful bacteria.

Additionally, antimicrobial peptides are considered promising platforms for novel antibiotics. As you might know, we are currently facing a severe antibiotic crisis. For some bacteria-caused diseases, the current commercially available antibiotics are no longer effective.

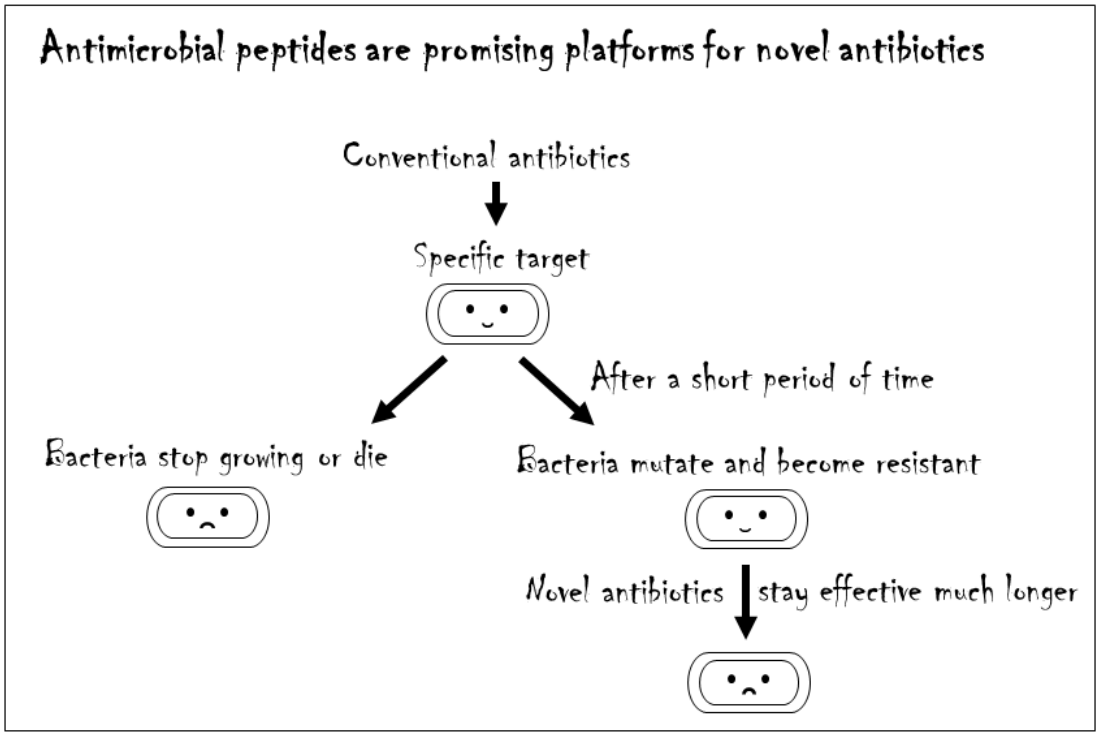

The major reason why this is happening is that conventional antibiotics only have specific targets within the bacteria. Once bacteria mutate those specific targets, the conventional antibiotics become ineffective. In contrast, antimicrobial peptides target bacteria in many different ways as mentioned in Q2. Therefore, it takes much longer for bacteria to mutate and escape from all the actions of the antimicrobial peptides.

Q4: What bacterial system are you studying?

We chose *E. coli* (*Escherichia coli*) as our model system, as it is a very common and well-studied bacterium. *E. coli* normally live in the intestines of people and animals. Most *E. coli* are harmless and actually are an important part of a healthy human intestinal tract. However, some *E. coli* are pathogenic, meaning they can cause illness such as diarrhea. The pathogenic *E. coli* in general come from contaminated food or water. *E. coli* consists of many species, and our lab started with a non-pathogenic one called MG1655. The common characteristics of *E. coli* are listed in the graphic below.

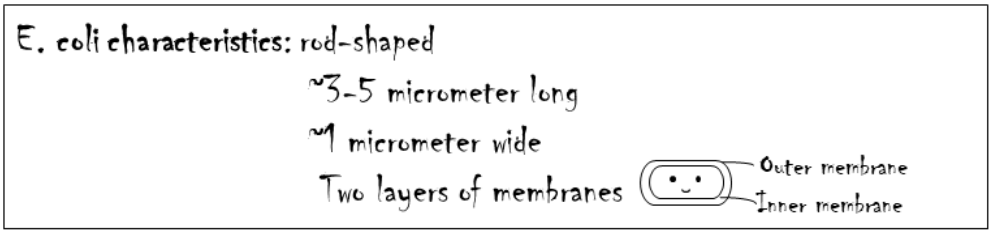

Q5: How do you perform the experiments?

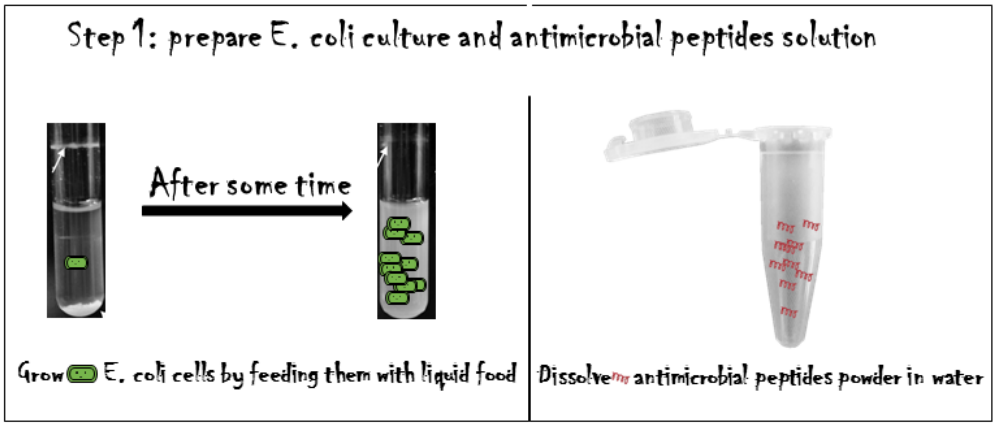

Step 2: Set up lasers and microscope

A table equipped with different-wavelength lasers and various optics that direct laser beams to the microscope

A microscope attached to camera and computer

Step 3: Add antimicrobial peptides solution to E. coli cells in a small chamber

A small chamber placed on microscope, providing ~10 microliter space

(a) Flow E. coli cells to a small chamber

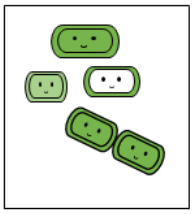

(b) Flow antimicrobial peptides solution

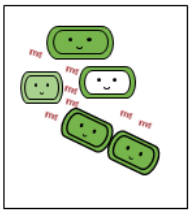

E. coli cells are immobilized but stay alive in the small chamber

Step 4: Take movies via software installed in computer

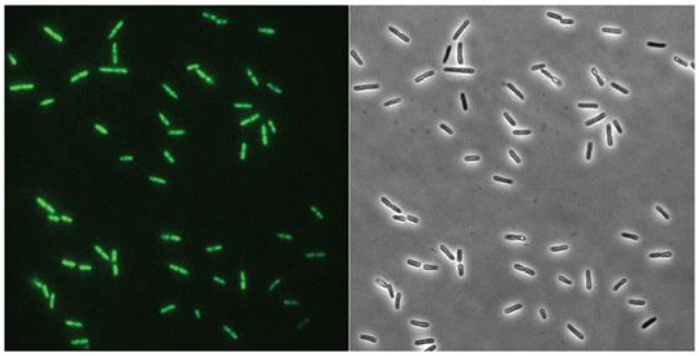

Channel 1 (observe fluorescence within individual E. coli cells)

Channel 2 (observe the shape and location of individual E. coli cells)

Q6: What is the advantage of your technique?

No two leaves are alike, and similarly no two *E. coli* cells are alike even though they have identical DNA. Historically, scientists studied the actions of antimicrobial peptides in an entire population of bacterial cells and assumed that all the cells respond the same. However, the truth might be different. For example, our lab noticed that dividing *E. coli* cells are more susceptible to antimicrobial peptide LL-37. As shown in the graphic below, dividing *E. coli* cells tend to lose green fluorescent protein much earlier than non-dividing cells, indicating that LL-37 broke their membranes much earlier. In addition, the red fluorescence, an indicator for the disruption of the inner membrane, appears at the end of the non-dividing *E. coli* cell first, but first appears in the middle of the dividing *E. coli* cell. This suggests that LL-37 attacks the inner membrane differently on these two types of *E. coli* cells. However, for both types of *E. coli* cells, red fluorescence always appears as green fluorescent protein diminishes. Overall, our technique

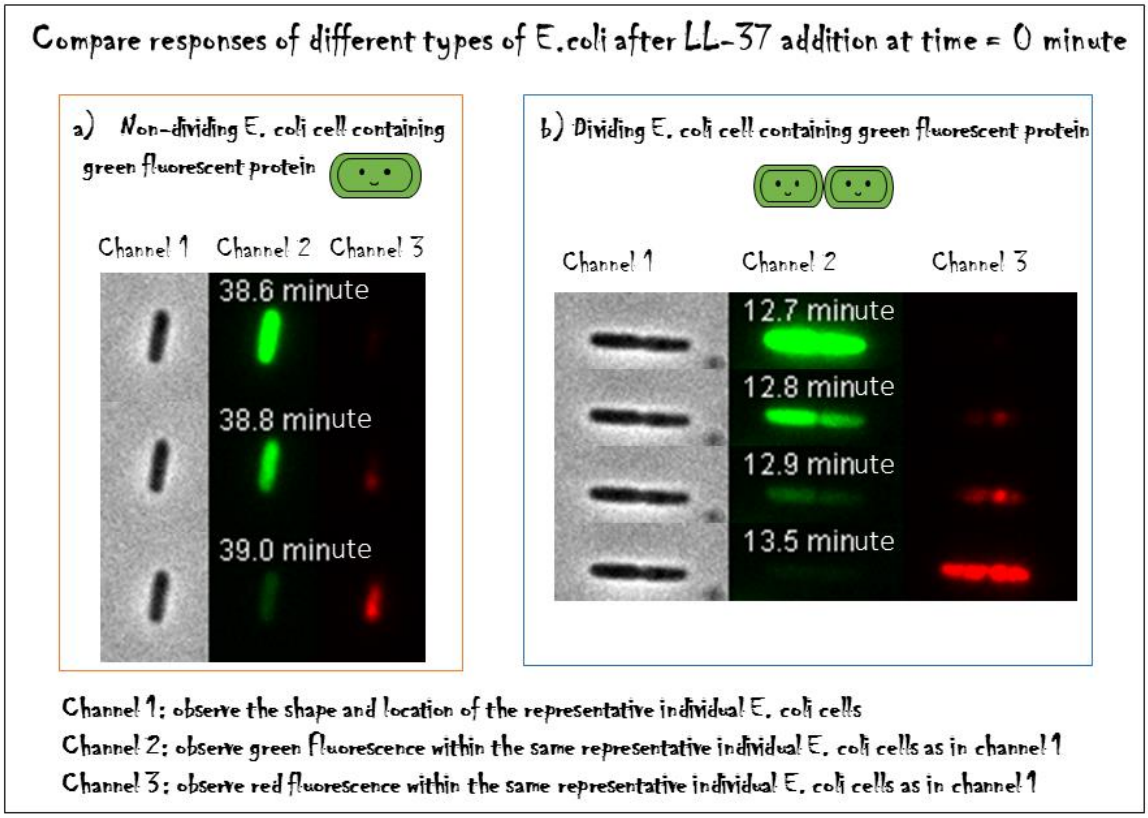

provides multiple measurements on the same individual cells and comparisons across different types of cells. It is a powerful technique that reveals a complete picture of antimicrobial peptides' actions on live bacterial cells, giving us feedback for novel antibiotic design and bacterial control.

Q7: What is the major finding in your thesis work?

For the first time, I demonstrated a series of actions of Melittin on both membranes of live *E. coli* cells. In particular, as shown in the graphic below, I figured out both timing and order for outer/inner membrane disruption events, outer/inner membrane re-sealing events and outer/inner membrane re-disruption events. We hypothesize that many antimicrobial peptides disrupt membranes of bacteria, but bacteria then reseal until antimicrobial peptides disrupt again.

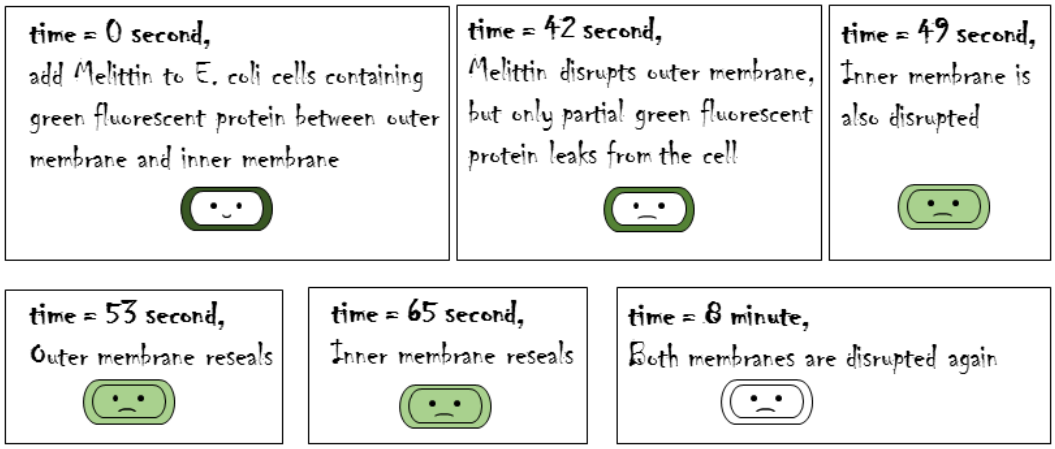

In addition, we found that several antimicrobial peptides not only disrupt membranes of *E. coli*, but also induce the formation of harmful compounds inside *E. coli* cells. We also figured out the possible relationship between these two distinct actions of antimicrobial peptides. Overall, my thesis work is enhancing our understanding of antimicrobial peptides' actions in live *E. coli* cells, providing insights into bacteria-related disease treatment and novel antibiotics

development. Many labs in the antimicrobial peptides field showed great interest in our powerful assays. We hope that our single-cell, fluorescent microscope technique can contribute more to the antimicrobial peptide field.

Q8: What is the current stage of developing novel antibiotics from antimicrobial peptides?

As of January 2018, more than ten antimicrobial peptides are in clinical use, such as daptomycin, vancomycin and bacitracin. More are in clinical trials. We hope that more novel therapeutic agents will come into market, saving us from resistant bacteria.